

May 2014

Effect of Processing Parameters and Matrix Shrinkage on Porosity Formation During Synthesis of Metal Matrix Composites with Dual-scale Fiber Reinforcements Using Pressure Infiltration Process

Reihaneh Etemadi

University of Wisconsin-Milwaukee

Follow this and additional works at: <https://dc.uwm.edu/etd>



Part of the [Mechanical Engineering Commons](#)

Recommended Citation

Etemadi, Reihaneh, "Effect of Processing Parameters and Matrix Shrinkage on Porosity Formation During Synthesis of Metal Matrix Composites with Dual-scale Fiber Reinforcements Using Pressure Infiltration Process" (2014). *Theses and Dissertations*. 686.
<https://dc.uwm.edu/etd/686>

This Thesis is brought to you for free and open access by UWM Digital Commons. It has been accepted for inclusion in Theses and Dissertations by an authorized administrator of UWM Digital Commons. For more information, please contact open-access@uwm.edu.

EFFECT OF PROCESSING PARAMETERS AND MATRIX SHRINKAGE ON
POROSITY FORMATION DURING SYNTHESIS OF METAL MATRIX
COMPOSITES WITH DUAL-SCALE FIBER REINFORCEMENTS USING
PRESSURE INFILTRATION PROCESS

by

Reihaneh Etemadi

A Thesis Submitted in
Partial Fulfillment of the
Requirements for the Degree of

Master of Science
in Engineering
at

The University of Wisconsin-Milwaukee

May 2014

ABSTRACT

EFFECT OF PROCESSING PARAMETERS AND MATRIX SHRINKAGE ON POROSITY FORMATION DURING SYNTHESIS OF METAL MATRIX COMPOSITES WITH DUAL-SCALE FIBER REINFORCEMENTS USING PRESSURE INFILTRATION PROCESS

by

Reihaneh Etemadi

University of Wisconsin-Milwaukee, 2014
Under the Supervision of Professor K. M. Pillai

This is first such study on porosity formation phenomena observed in dual-scale fiber preforms during the synthesis of metal matrix composites (MMCs) using the gas-based pressure infiltration process (gas PIP). In this thesis, different mechanisms of porosity formation during pressure infiltration of Al-Si alloys into Nextel's 3D woven ceramic-fabric reinforcements (a dual-porosity or dual-scale porous medium) are studied. The effect of processing conditions in terms of the infiltration temperature and pressure on porosity content of the ceramic fabric infiltrated by the alloys through the gas PIP is investigated. Relative density (RD), defined as the ratio of the actual MMC density and the density obtained at ideal 100% saturation of the preform, was used to quantify overall porosity. Increasing the infiltration temperature led to an increase in RD (and reduction in porosity) due to reduced viscosity and enhanced wettability leading to improved feedability of the liquid metal. Similarly, increasing the infiltration pressure led to enhanced penetration of fiber tows and led to higher RD and reduced porosity. For the first time, the modified Capillary number (Ca^*), which is found to predict formation of porosity in polymer matrix

composites quite well, is employed to study porosity in MMCs made using PIP. It is observed that in the high Ca^* regime used in the present study (and common in PIP), the overall porosity shows a strong downward trend with increasing Ca^* due to a decrease in the size of trapped air pockets inside fiber tows due to increased infiltration pressures. This contradicts the well-known result of increasing porosity with Ca^* observed by Patel et al. in [1]. In addition, the effect of matrix shrinkage on porosity content of the samples is studied through using a zero-shrinkage Al-Si alloy as the matrix: usage of this alloy as the matrix led to a reduction in porosity content.

Keywords: porosity, metal matrix composite, MMC, pressure infiltration process, RTM, voids, Capillary Number, porous media, dual scale, dual porosity

TABLE OF CONTENTS

ABSTRACT.....	ii
TABLE OF CONTENTS.....	iv
LIST OF FIGURES	v
LIST OF TABLES.....	ix
ACKNOWLEDGEMENTS.....	x
CHAPTER 1: INTRODUCTION.....	1
1.1 INTRODUCTION TO METAL MATRIX COMPOSITES.....	1
1.2 MODELING OF RESIN FLOW THROUGH DUAL-SCALE FIBER MATS AND POROSITY FORMATION DURING LCM PROCESSING OF POLYMER MATRIX COMPOSITES	33
1.3 POROSITY FORMATION IN CAST METAL MATRIX COMPOSITES DURING PRESSURE INFILTRATION PROCESS	42
1.4 AIM OF THE PRESENT STUDY AND JUSTIFICATION.....	54
CHAPTER 2: INSTRUMENTATION AND EXPERIMENTAL PROCEDURE.....	58
CHAPTER 3: RESULTS AND DISCUSSION.....	73
3.1 EFFECT OF PROCESSING CONDITIONS ON THE QUALITY OF INFILTRATION AND POROSITY CONTENT	79
3.2 EFFECT OF MODIFIED CAPILLARY NUMBER ON POROSITY FORMATION IN MMC SAMPLES	82
3.3 EFFECT OF MATRIX SHRINKAGE ON POROSITY IN MMC SAMPLES	84
CHAPTER 4: SUMMARY AND CONCLUSIONS AND FUTURE WORK	87
REFERENCES	89
APPENDICES	112
APPENDIX A: RAW DATA FOR THE EXPERIMENTS	112
APPENDIX B: CALCULATING DARCY VELOCITY FOR MODIFIED CAPILLARY NUMBER	123
APPENDIX C: ESTIMATION OF PERMEABILITY FOR FIBER PREFORM.....	126
APPENDIX D: WETTING PHENOMENA IN COMPOSITE SYNTHESIS	129
APPENDIX E: THE PHYSICS OF SHRINKAGE POROSITY	134

LIST OF FIGURES

Figure 1. Classification of the composites within the group of materials [2] (This figure is replicated here with permission from "John Wiley and Sons").	3
Figure 2. Development curve of the market for modern materials [2] (This figure is replicated here with permission from "John Wiley and Sons").	12
Figure 3. Liquid state processes for fabrication of MMCs [2] (This figure is replicated here with permission from "John Wiley and Sons").	16
Figure 4. Micrographs of a) SiC particles [86], b) Al ₂ O ₃ particles [87], c) aluminum borate whiskers [88] and d) Alumina platelet [89] preforms used in different pressure infiltration processes. (These figures are replicated here with permission from "Elsevier").	18
Figure 5. Micrographs of aluminum alloy matrix composites fabricated by pressure infiltration process. Preforms are made form a) nickel coated carbon fibers [90], b) Altex (γ -Al ₂ O ₃) fibers [91], c) fly ash cenospheres [68] and d) SiC particles [91](These figures are replicated here with permission from “Springer” and “Elsevier”.)	19
Figure 6. Schematic of a bottom filling gas pressure infiltration apparatus [68]	22
Figure 7. Schematic of a top filling gas infiltration process [102]	23
Figure 8. A schematic of the liquid metal gas infiltration process, showing the four basic stages [102]	23
Figure 9. Direct squeeze casting infiltration	26
Figure 10. Indirect squeeze casting infiltration	27
Figure 11. Schematic of the pressure die infiltration: a) before infiltration and b) after infiltration.	31
Figure 12. A schematic depicting the saturated, partially saturated (L_s), and unsaturated flow regions within dual-scale preforms, and highlights the delayed impregnation of the fiber tows [130].	36
Figure 13. Percent area macro- and microvoids as a function of modified capillary number in RTM (This approximate graph is based on the information provided in reference [148].)	40
Figure 14. Five different interfacial configurations studied by Ilegbusi and Yang for porosity nucleation.	53

Figure 15. Scanning Electron Micrographs showing (a) porosity between Nextel fibers and also (b) porosity within the matrix	57
Figure 16. Gas pressure infiltration equipment and its schematic.....	59
Figure 17. (a) Non-crimp orthogonally woven alumina fabric with 3D weave pattern [215],(b) Longitudinal cross section of the 3D woven Nextel fabric with 10X magnification.	63
Figure 18. Different patterns of 3D woven Nextel fibers. Tighter pattern has more inherent structural integrity and may produce stronger and stiffer composites	63
Figure 19. (a) Samples being heated in the furnace under vacuum followed by pressurizing with Ar.(b), (c) Pressure infiltration setup available at the Composite Center, University of Wisconsin-Milwaukee	65
Figure 20. Experimental set-up for investigating the temperature map of the furnace	66
Figure 21. Labview Signal Express software was used to find the temperature map of the furnace.....	67
Figure 22. Resultant Temperature map of the furnace	67
Figure 23. Square tube that was used as mold in the experiments.	69
Figure 24 .The reinforcement is placed at the bottom of the mold.....	70
Figure 25. After placing the filter on top of the reinforcement, the metal is placed on top of the filter inside the mold.....	71
Figure 26. Mettler Toledo standard level analytical balance with density determination kit.	74
Figure 27. A typical MMC sample created after the PIP experiment.....	75
Figure 28. Relative density of the MMC samples made using gas PIP increases with the infiltration temperature and pressure.	77
Figure 29 . Optical micrographs of the infiltrated fabric: (a) The 100 psi infiltration pressure case showing large gaps between fiber tows infiltrated with metal while almost no metal can be seen in the pores inside the fiber bundles due to low infiltration pressure. (Magnification 50x) (b) By increasing the infiltration pressure to 200 psi, some metal is observed to have infiltrated inside the fiber tows. (Magnification 100x)(c) More metal infiltration occurred inside the tows as the pressure increases to 300 psi.(Magnification 200x) (Note that the bright areas in these figures correspond to the matrix while the dark areas represent either the fibers or empty voids between them.).....	81

Figure 30. Experimentally observed increase in the relative density with an increase in the modified capillary number, Ca^*	84
Figure 31. A plot of Relative Densities as a function of infiltration temperature for pressure infiltration of 3D-Nextel fabric with A356 and Mercusil alloy at 200 psi.	86
Figure 32. Micrograph of a S11 sample (Magnification 50X)	113
Figure 33. Micrograph of a fiber tow of a S23 sample (Magnification 200X).....	113
Figure 34. Micrograph of a S32 sample. (Magnification 200X)	114
Figure 35. Micrograph of a S33 sample. (Magnification 50X)	114
Figure 36. Micrograph of a fiber tow of S34 sample. (Magnification 200X)	115
Figure 37. Micrograph of S34 sample with higher magnification. Porosity can be seen at the contact areas of the fibers.(Magnification 500X)	115
Figure 38. Micrograph of Mercusil Alloy (Magnification 50X)	118
Figure 39. Micrograph of MMC with Mercusil Alloy as matrix made at 750C and 200 psi (Magnification 50X)	118
Figure 40. Micrograph of MMC with Mercusil Alloy as matrix made at 750C and 200 psi showing Z yarns (Magnification 50X).....	119
Figure 41. Micrograph of a partially infiltrated Z yarn (Magnification 100X)	119
Figure 42. Micrograph of MMC sample made by Mercusil alloy as the matrix at 750 C and 200 psi (Magnification 100X).....	120
Figure 43. Micrograph of MMC sample made by Mercusil alloy as the matrix at 800 C and 200 psi (Magnification 200X).....	120
Figure 44. Micrograph of MMC sample made by Mercusil alloy as the matrix at 800 C and 200 psi showing the partial infiltration of a fiber tow (Magnification 200X)	121
Figure 45. Micrograph of MMC sample made by Mercusil alloy as the matrix at 800 C and 200 psi showing the partial infiltration of a fiber tow and porosity (Magnification 500X)	121
Figure 46. Z yarn fibers inside a tow infiltrated with mercusil alloy (Magnification 500X)	122
Figure 47. Micrograph of MMC sample made by Mercusil alloy as the matrix at 800 C and 200 psi (Magnification 1000X).....	122

Figure 48. Variation of contact angle of Al-Mg with Al₂O₃ versus Temperature [226] .
..... 133

LIST OF TABLES

Table 1. Some examples of application of metal matrix composites [2].....	4
Table 2. Typical Reinforcements of metal matrix composites [24-32]	7
Table 3. Selected properties of some metals and reinforcement particles [33-35].....	8
Table 4. Four different types of pores, their development and characterization in the solidifying casting of Al-7Si-Mg [158].	43
Table 5. Summary of various works on mathematical modeling of pressure infiltration for making of MMCs.....	45
Table 6. Chemical composition of Aluminum alloys A356 and Mercusil	61
Table 7. Important properties of 3M™ Nextel™ 720 ceramic fibers	62
Table 8. Some details of the experiments conducted to study the effect of infiltration pressure and temperature on the quality of infiltration and porosity content in the MMC samples created using the gas PIP. The sample numbers are in the form S _{ij} with i and j being the numerical values—note that i and j changes with the infiltration pressure and temperature, respectively.	76
Table 9. Some of the properties of the Aluminum alloy A356 used in our calculations [203]......	83
Table 10. Raw data for the first set of experiments to study the effect of processing parameters on the porosity content of MMC samples.	112
Table 11. Raw data for the second set of experiments to study the effect of matrix shrinkage on the porosity content of MMC samples. The applied infiltration pressure for all these experiments was 200 psi.	117
Table 12. Some micro-geometrical properties of the preform and comparison of the dual-scale permeabilities obtained using the Papathanasiou model and the single-scale permeability obtained using the Kozeny-Carman model.....	128

ACKNOWLEDGEMENTS

First and foremost, I must appreciate all the help and support I received from my supervisor, Prof. Krishna Pillai during my years in UWM for his patience, knowledge and kindness always helped me find my way through difficulties.

Many thanks to Prof. Rohatgi at the department of Material Engineering of University of Wisconsin-Milwaukee, for allowing me to use their facilities to perform experiments and his incredibly valuable advice that has contributed to the outcome of my research. I also express the deepest appreciation to Prof. Rohatgi and Dr. Dsouza who accepted to be in my committee and their great help and special thanks to Dr. Benjamin Schultz and Dr. J.B. Ferguson, for their helpful comments during the laboratory work for this study.

I am also very much thankful to my dear husband, Dr. Sajad Hamidi, who has always been a big support in my life. I would like to gratefully thank my parents that despite the far distance, their prayers are always with me.

Financial help from UWM graduate school and UW-Foundation through their RGI grant and partial ARL funding is gratefully acknowledged.

CHAPTER 1: INTRODUCTION

1.1 INTRODUCTION TO METAL MATRIX COMPOSITES

A composite material consists of two or more separate phases, intimately bonded together at a sufficiently fine scale, which can be considered a new material with its own distinctive properties. A metal matrix composite (MMC) is a composite that contains a continuous metallic matrix, and a reinforcement that represents at least a few volume percentage of the final composite. This class of composites include many different materials that can be distinguished according to their base metal (e.g., aluminum, copper, titanium); according to the reinforcement phase (e.g., fibers, particles, whiskers); or according to their manufacturing process (e.g., powder metallurgy, diffusion bonding, infiltration, stir casting). A wide range of metals and their alloys can be used as matrix materials. The specific application of the composite material mainly determines the selection of proper matrix material [2]. Some common matrix materials include Aluminum and Aluminum alloys, Titanium alloys, Magnesium and its alloys, Cobalt, Copper, Silver, Nickel, Niobium [3].

Figure 1 shows the general classification of the materials based on their atomic bonds. Combinations of metals with ceramics are the most common form of MMCs. While most metallic materials have good electrical and thermal conductivity and are ductile and easy to shape, ceramic materials are poor conductors, hard and brittle. On the other hand, while most ceramic materials retain their stability and stiffness at high temperatures, service life of most metals is limited even at moderate temperatures. Metals undergo microstructural changes and their mechanical properties deteriorate at high temperatures. A ceramic

reinforced metal matrix composite is expected to fill the space between the two materials and offer distinct advantages over conventional monolithic metals and alloys. The advantages are brought about by judicious utilization of such useful properties of the metallic matrix as ductility and toughness and those of the ceramic reinforcements as hardness, low thermal expansion and high temperature stability to fulfill the specific requirements of applications where both materials would fail independently. In other words, MMCs can be custom-made to meet specific application needs through changes in the matrix composition and microstructure, the reinforcement type, volume, size, morphology and distribution, as well as the processing route employed.

Compared to the matrix alloy, metal matrix composites enjoy higher temperature capability, higher stiffness and strength, and lower coefficient of thermal expansion. In addition, many particulate and whisker reinforced metal matrix composites are fabricable with conventional processes. However, presence of ceramic phases may result in lower ductility, fracture toughness and thermal conductivity. Higher cost, rather complex fabrication methods for fiber reinforced composites and recyclability problems are among the disadvantages of metal matrix composites [3]. Aluminum Matrix Composites (AMCs) have the following advantages over unreinforced materials:

- Greater strength
- Improved stiffness
- Reduced density (weight)
- Improved high temperature properties
- Controlled thermal expansion coefficient
- Thermal/heat management

- Enhanced and tailored electrical performance
- Improved abrasion and wear resistance
- Control of mass (especially in reciprocating applications)
- Improved damping capabilities.

It is possible to modify properties of Al/Al alloy by more than two-three orders of magnitude by incorporating appropriate reinforcement with suitable volume fraction [4] .

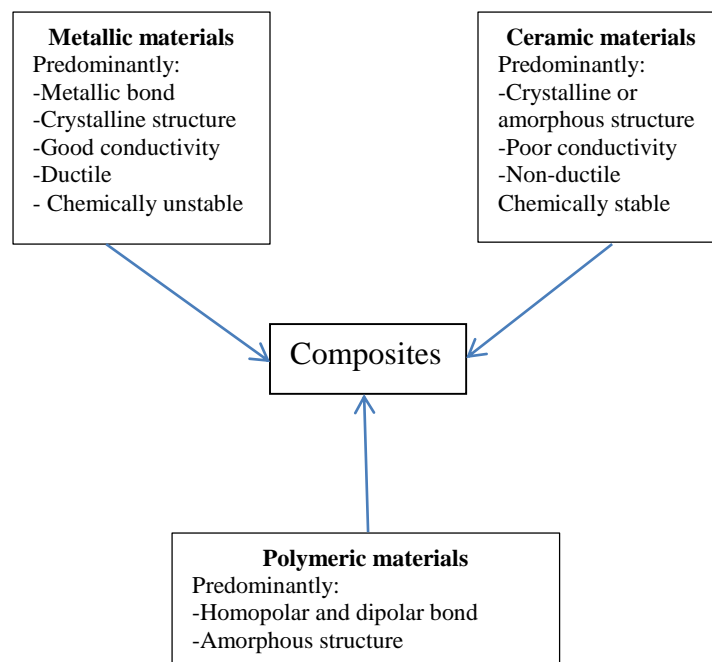


Figure 1. Classification of the composites within the group of materials [2] (This figure is replicated here with permission from "John Wiley and Sons").

Following decades of intensive fundamental research in the field of metal matrix composites, significant progress has occurred in development of these materials in recent years and they began to find commercial applications and become a part of daily life. Some examples of application of metal matrix composites are shown in Table 1. A wide spectrum

of applications from sports equipment to transportation, electronics and aerospace sector is evident from this table.

Table 1. Some examples of application of metal matrix composites [2].

MMC Type	Reinforcement	Application	Potential Benefits	Processing method
Al-MMCs	Silicon carbide particles and fibers	Piston Connecting rod Brake drum and rotor Bicycle frame Golf clubs Aeroengines (Inlet Vanes, outlet guide vanes, rotor casings) Space applications (Joint and attachment fittings) Electronic packaging Thermal management	High specific stiffness Good fatigue properties Relatively low-cost High thermal conductivity Tailorable CTE Low density Conventional processing	Powder metallurgy Vacuum Hot Pressing (VHP) Hot Isostatic Pressing (HIP) Stir casting Squeeze casting
	Boron particles	Space shuttle orbiter (tubular struts frame, landing gear link)	Low density, High Stiffness, Low CTE, Good electrical conductivity	Diffusion bonding
	Graphite particles, Carbon fibers	High-gain antenna boom for the Hubble Space Telescope, Electronic packaging	Low density High thermal conductivity High temperature property Lubricity	Diffusion bonding Casting
	Al ₂ O ₃ particles and fibers	Engine components Drive shaft	Wear resistance, Improved cooling efficiency, High specific modulus	Casting Sinter forging Extrusion
Mg-MMCs	Graphite particles, Carbon fibers	Tubes for truss structure applications	High thermal conductivity, High specific Strength and Stiffness, Low CTE	Vacuum assist casting
Cu-MMCs	Carbon fibers	Liquid oxygen turbo-pump, housing for rocket propulsion, Thermal management	High thermal conductivity, High temperature capability, High specific Strength and stiffness, Stability	Pressure infiltration PVD
Ti-MMCs	Silicon carbide monofilament and fibers	Aeroengines (Blades and vanes, compressor blings, casings, shafts, struts and links) Exhaust valves	Increased stiffness High strength Weight reduction High-temperature resistance	Hot pressing Fiber and foil method Plasma spray technique Matrix coated fiber technique Extrusion and forging
Fe-MMCs	Titanium diboride	Automobile engine parts	High young's modulus, High tensile and fatigue properties, Weight reduction, Improvement in vibration characteristics	Powder extrusion and machining

More recently, 3M™ has developed alumina fiber (continuous) reinforced aluminum composites. Compared to high strength steel, CFAMCs developed by 3M™ offers equivalent strength at less than half the density and retains its strength to 300 °C and beyond. Composites possess four times the electrical conductivity of steel or half that of pure aluminum. These composites have been targeted for several functional Layered composites, high-conductivity composites, nanoscale composites, microcellular metals, and bio-derived composites are new varieties of MMCs which have been added in last decade to ceramic fiber- or particle-reinforced light metals as the traditional MMCs [5].

MATRIX ALLOYS

A wide range of metals and their alloys can be used as matrix materials. The specific application requirement of the composite material is the main factor determining the selection of a proper matrix material [2]. Some common matrix materials include Aluminum, Titanium, Magnesium, Cobalt, Copper, Silver, Nickel, and their alloys [3] Among these various matrix materials, Aluminum and its alloys are widely used in MMCs fabrication. The reason is that they are light in weight, economically viable.

Steel matrix composites have also been fabricated. First type of these composites is what has been labeled as fully steel composites in which all elements of the structure are steel based but differ in microstructure or in chemical composition. An example is dual-phase steel with several percentages of hard martensitic particles in a soft ferritic matrix. A variation of these materials is the dynamic composites. In these materials, the volume fraction of the hard phase changes with plastic deformation. TRIP (transformation-induced

plasticity) and TWIP (twinning-induced plasticity) steels are among these dynamic composites in which during plastic deformation one or more of the phases can either twin or undergo a martensitic transformation [6]. The traditional type in which steel is combined with particles or layers of other material has also been produced but it is less developed than that for aluminum or magnesium matrices [6].

There has been considerable amount of studies on bulk metallic glass (BMG) composites carried out in recent years. Although, BMGs have unique properties such as exceptionally high yield strength, hardness, and elastic limit, they are very brittle. This has limited their use in critical applications. Addition or creation of second phases in the amorphous matrix is one of the approaches taken to improve the ductility of BMGs. This approach seeks to promote homogeneous distribution of shear bands instead of widely spaced (or single) concentrated shear bands which leads to catastrophic failure. Copper base [7], Zr-based [8-10], Cu/Zr-based [11, 12], Zr/Ti-based [13], Mg based [14], Ni based [15] and Pd based [16] BMGs are among the ones investigated.

REINFORCEMENTS

Reinforcement materials for metal matrix composites are produced in the form of continuous fibers or sheets, short fibers or whiskers and particles. They are generally hard and refractory ceramic materials, which combine high strength and elastic modulus with high temperature capability. However, depending on the specific property requirements and applications, soft materials such as graphite flakes and lead particles, as well as refractory metals and intermetallics have been used [17-23].

Table 2 lists some important reinforcements used in metal matrix composites along with their aspect ratios (length/diameter) and diameters. As it is evident from Table 2, SiC and Al_2O_3 are the most commonly used reinforcement in metal matrix composites.

Table 2. Typical Reinforcements of metal matrix composites [24-32]

Type	Aspect Ratio	Diameter, μm	Examples
Particle	1-4	1-25	SiC, Al_2O_3 , BN, TiC, B_4C , WC
Discontinuous fiber: Whisker Short fiber	10-10000	1-5	$\text{Al}_2\text{O}_3+\text{SiO}_2$ SiC, TiB_2 , Al_2O_3 Al_2O_3 , SiC, ($\text{Al}_2\text{O}_3+\text{SiO}_2$), vapor grown carbon fibers
Continuous fiber	>1000	3-150	SiC, Al_2O_3 , C, B, W, Nb-Ti, Nb_3Sn , TiC, B_4C , WC

Based on the production and processing methods and the matrix system of the composite material, a variety of property requirements shall be fulfilled by the reinforcements. These include but not limited to low density, mechanical compatibility (a low thermal expansion coefficient but compatible with the matrix), chemical compatibility, thermal stability, high Young's modulus, high compression and tensile strength, good processability, and economic viability. Selected properties of these reinforcement materials in comparison with those of two aluminum and magnesium alloys are presented in Table 3.

Table 3. Selected properties of some metals and reinforcement particles [33-35]

Particle	Elastic modulus, GN m ⁻²	Density, g cm ⁻³	Coefficient of thermal expansion K ⁻¹	Specific heat, J kg ⁻¹ K ⁻¹	Thermal conductivity, Wm ⁻¹ K ⁻¹	Melting point, °C
Al (6061-T6)	70	2.8	23.4 x 10 ⁻⁶	960	171	580
Mg (AZ31B)	40	1.7	25.2x 10 ⁻⁶	1000	76	570
SiC	420-450	3.2	4.3x10 ⁻⁶	840	10-40, at 1100°C	2730
Al ₂ O ₃	380-450	3.96	7.0 x 10 ⁻⁶	1050	5-10, at 1000°C	2072

In recent years, nano-sized materials have also drawn much interest as reinforcements in metal matrix composites because of their superior properties compared with those of micro-sized particles. Nano-Al₂O₃ [29, 32], nano-SiC [36, 37], Carbon nanotube (CNT) [24, 25, 28, 31, 38-40] and nano-TiB₂ [26, 27, 41], all in discontinuous form are among the reinforcements used by different researches. So far, most of the nano-sized reinforced metal matrix composites have been produced by solid-state processes, which are not appropriate for the production of large and complicated components. Liquid-state processes such as vortex method, squeeze casting and pressure infiltration process provide greater freedom in component design and manufacturing. However, very large specific surface area and high interfacial energy of nano-size reinforcements result in their poor wetting, agglomeration tendency and poor distribution in the melt. Therefore, special techniques are required for the addition of reinforcements to the melt. For example, Abbasipour et al. [24, 38] and Firoozbakht et al. [28, 40] used Ni-P electroless plating technique to co-deposit CNTs on aluminum and magnesium particles, respectively. The CNT deposited particles were then injected into agitated melts in fully liquid or semisolid

conditions to result in gradual release of CNTs in the melt. Their results show significant refinement of cast microstructures as well as improvement of mechanical properties compared with the monolithic samples and composite samples where untreated CNT was injected. Shayan et al. [31, 42] produced strips of pure Al-MW CNT composites by accumulative roll bonding (ARB) method and then melted and stirred predetermined quantities of these with A356 and Al-13%Si ingots in a crucible and squeeze cast the resultant slurry. Their results show improved mechanical properties of the produced nanocomposites. Yang and Schaller [43] used CVD technique to grow CNTs on a porous Al₂O₃ preform and then infiltrated the preform with molten magnesium resulting in potentially uniform distribution of CNTs in the matrix. Other researchers have used ball milling and pressing of mixtures of metallic powders and nano-reinforcements to produce porous preforms which can be infiltrated by melt [44].

An area that has grown significantly over the past decade is ceramic reinforcements having three dimensionally percolating architectures. Notable examples are porous preform structures that are formed by freeze-casting [45], three-dimensional printing [46, 47] or direct-write assembly [48, 49] of ceramics. Once infiltrated with metal, a composite is formed in which both metal and ceramic phases are three-dimensionally percolating. Seleznev et al. [46] describe a method where the preforms are 3-D printed, invested into refractory material, pressure infiltrated with liquid metal and then washed away after solidification to leave behind net-shaped composite parts of such high quality that can be used as prototype aerospace parts.

As for fiber-reinforced metal matrix composites, significant progress has been made in fabrication of high-quality ceramic fibers suitable for the reinforcement of metals. An

example is Nextel™ alumina fibers available in a variety of textile forms. They are light, very strong and have a CTE similar to titanium. At the same time they are flexible and can be woven to very complicated patterns [3].

Bulk metallic glass (BMG) matrix composites were discussed in the previous section. BMGs have also been used as the reinforcement in metal matrix composites with interesting results. So far, however, these seem to be limited to aluminum and magnesium alloys and mostly using powder metallurgy routes [23, 50-54].

Recently, Lucci et al. and Nosonovsky et al. introduced a new interesting role for the reinforcement materials, i.e., self-healing of cracked metal matrix composites [55-57]. They showed that by embedding microcapsules or microtubes filled with a low melting point healing material, cracks formed in the matrix can be healed. Self-healing of aluminium alloy 206 matrix reinforced with carbon fiber microtubes filled with Sn60Pb40 solder was demonstrated as an example. When the cracked samples are heated above 300 °C for five minutes, the cracks are completely or partially filled with the solder. The amount of available solder, the wettability of the cracks with the liquid solder and the crack diameter, which should be smaller than the capillary length of the solder, were recognized as the factors controlling the filling of the crack by the solder. A different technique involving material reinforcement with a shape-memory alloy (SMA) fibers, such as Ni Ti was also introduced. SMA fibers that are embedded in the matrix change their shape (extend) as a crack propagates. Upon heating, SMA fibers restore their original shape and thus the crack is closed.

MMC MARKET DEVELOPMENT

Modern material science has benefited a lot from metal matrix composites since their characteristics can be easily customized by merely changing the preform placement and type for any given application. Nevertheless, the knowledge produced as a result of the research efforts needs more time to be translated into industrial-scale reliable and cost-effective manufacturing technology [46]. Due to insufficient process stability and reliability, production and processing problems, and inadequate economic efficiency, metal matrix composites have not gained widespread industrial applications. Since the application areas of metal matrix composites such as automotive industry are very cost-oriented, manufacturers are not willing to pay additional cost for the use of these materials. The advantages of MMCs are realized only if a reasonable cost-performance relation exists in the component production.

National Composite Network (CNC) has recognized the following as some of the main barriers towards the advancement of metal matrix composites:

- Cost
- Lack of commercial applications
- Lack of standardization test procedures
- Lack of federal and industry standards
- CET mismatch between matrix and reinforcement
- Lack of non-destructive evaluation techniques

- Lack of repair techniques
- Lack of recycling techniques
- Lack of investment incentives
- Long incubation time between need identification and product commercialization

All these reasons have caused MMCs to be located just at the beginning stage of the evolution curve for modern materials (Figure 2) [2].

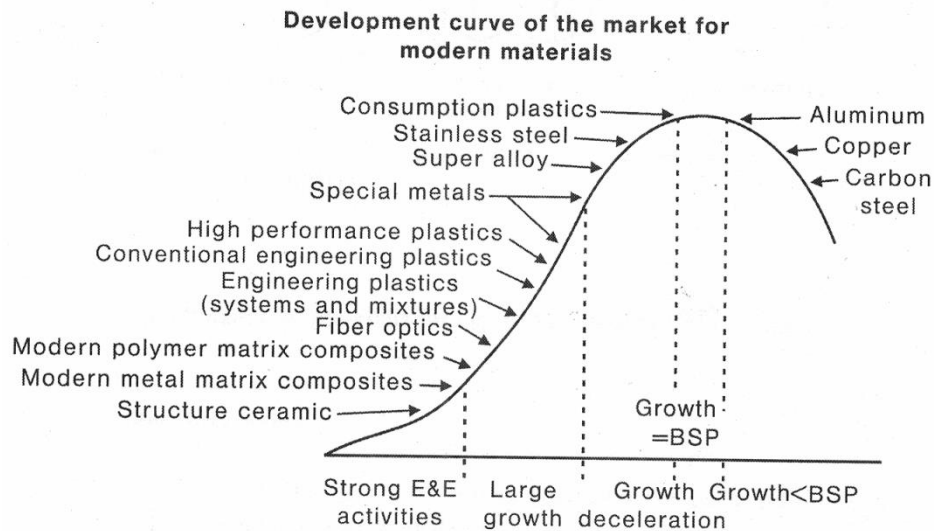


Figure 2. Development curve of the market for modern materials [2] (This figure is replicated here with permission from "John Wiley and Sons").

National Composite Network has also identified the following goals for advancing metal matrix composite technology to support industrial base needs:

- Lowering the cost of producing and using metal matrix composites
- Improving the communications between government, industry and academia
- Improving the commercial viability and increasing the commercial demand for metal matrix composites
- Striving to overcome the shortcomings of MMCs

PRODUCTION AND PROCESSING OF MMCS

Producing a composite consists of bonding one or more reinforcements with a continuous metal or alloy at the atomic level. The fine scale of reinforcement (traditionally between 0.5 and 200 μm in diameter and recently in nano-scale range) and the desire to make a composite free of defects such as pores, agglomerates or unwanted reaction phases, raises many critical issues. Various manufacturing techniques are used for MMCs production. The desired type, quantity, size and distribution of the reinforcement (particles and fibers), the matrix material, and the intended application of the composite are the most important factors in selecting a suitable processing technique. Different characteristic profiles result from using the same composition and amounts of the components but altering the manufacturing method, processing, finishing or the form of reinforcements.

Metal matrix composites can be manufactured by liquid, solid, or gaseous state methods, although the last route is not very common. In each of these methods, the reinforcement can be introduced as an ex-situ phase or can be created in-situ [2, 58, 59].

Solid-state processes include:

- Powder metallurgical processes such as pressing and sintering and/or forging of powder mixtures and composite powders, extrusion or forging of metal-powder particle mixtures or sprayed compatible precursor materials and hot or cold iso-static pressing of powder mixtures and fiber [23, 53, 60-63]
- Deformation based processes such as equal channel angular pressing (ECAP), accumulated roll bonding (ARB), and continual annealing and roll-bonding (CAR) processes [64-67] .

Based on the methods for physically combining the matrix and the reinforcement, the liquid-state processing technologies can be sorted into four major categories:

- **Infiltration** of short or long fibers, particulate or hybrid preforms by squeeze casting, vacuum infiltration, pressure infiltration or reaction infiltration [19, 68-70].
- **Dispersion** of particulate or short fiber reinforcements by stirring the reinforcements in fully liquid or semi-solid matrix metal followed by sand casting, permanent mold casting or high pressure die casting [24, 28, 31, 71, 72]
- **Spray mixing** of molten matrix alloy and the reinforcement particles and their collection on a chill surface [73-75].

In-situ fabrication of the reinforcements in the melt by encouraging given chemical reactions between the melt constituents [76-79]. Since 1960s, a large percentage of metal-matrix composites in the world have been manufactured by liquid-state processing or casting. Currently the liquid-state processes are preferred to other manufacturing techniques as they are more economical while benefiting from the advantages of well-proven casting processes. A majority of the commercially feasible MMCs are now being produced by these methods. Some of the possible methods of liquid-state processing are schematically shown in Figure 3 [2]. The main methods include melt stirring and compocasting (dispersion category), gas pressure infiltration, vacuum pressure casting, squeeze casting, and pressure casting (infiltration category).

An important advantage of infiltration process is the production of near-net shape parts with selective amount of various reinforcements [80]. Despite the apparent advantages of liquid state processes over other methods, there are some major challenges for fabrication of MMCs through these routes. These include poor wettability of the reinforcements by molten metal, non-uniform distribution and agglomeration of the reinforcements, undesirable reactions between the reinforcement and the matrix, and reinforcement initiated gas porosity.

Since this review is mainly concerned with pressure infiltration methods, therefore it is not going to go into the details of other processes. The other methods are presented in other review literature published in recent years [35, 44, 58, 81-83].

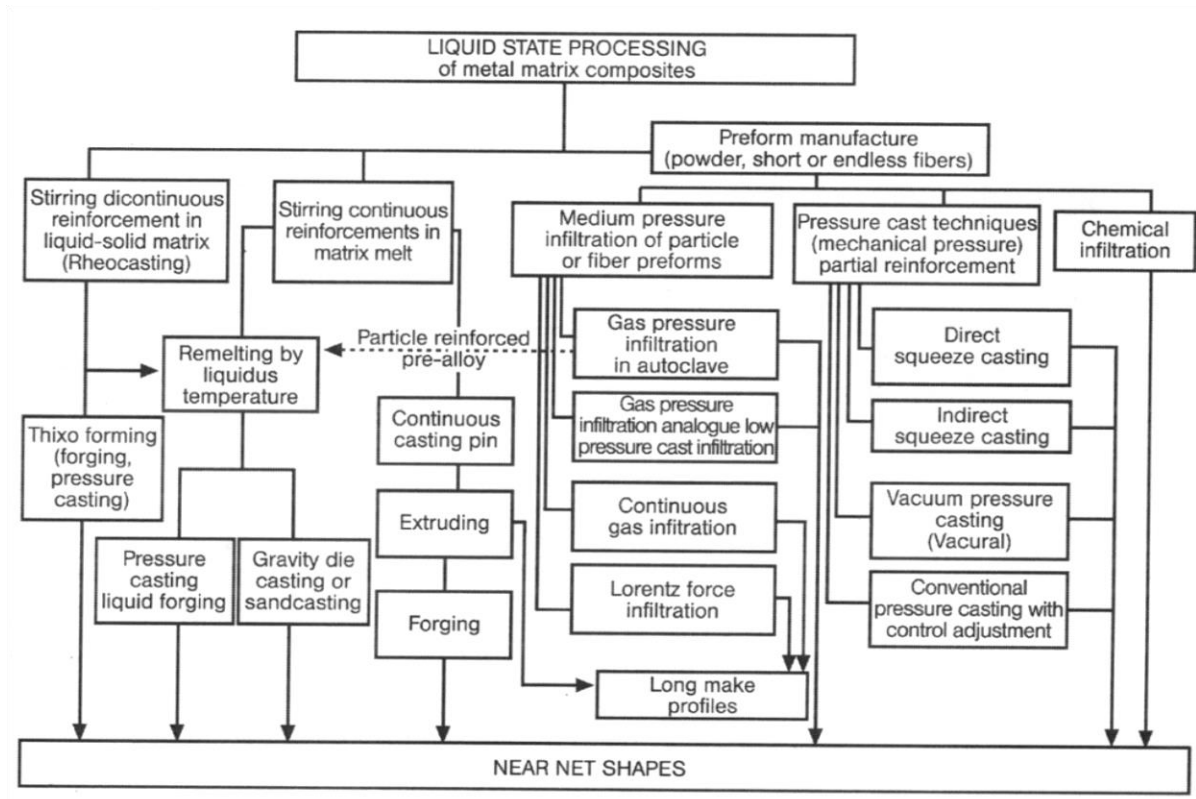


Figure 3. Liquid state processes for fabrication of MMCs [2] (This figure is replicated here with permission from "John Wiley and Sons".)

The pressure Infiltration process (PIP) is an accepted and widely used method for the production of metal matrix composites, especially when high volume fraction and uniform distribution of the reinforcing particles or fibers are desired [84, 85].

The pressure infiltration technology with the aim of producing near-net-shape parts can be subdivided into three important technological processes: ceramic preform manufacturing, mold and core manufacturing, and pressure infiltration technology.

In the liquid infiltration methods, a preformed dispersed phase (ceramic or non-ceramic particles, fibers, woven) is soaked in a molten matrix metal, which fills the spaces between the dispersed reinforcement phases. Driving force of the infiltration process may be either

capillary force of the dispersed phase (spontaneous infiltration) or an external pressure (vacuum, gaseous, mechanical, electromagnetic, centrifugal or ultrasonic) applied to the liquid matrix phase (forced or pressure infiltration).

Pressure infiltration process has emerged as a commercially important process. The most widespread matrix material is aluminum, which is the most common lightweight structural material. Reinforced Al-Al₂O₃ automobile engine components, such as diesel-engine pistons, engine block cylinder liners and crankshaft pulleys have been mass-produced in Japan and Europe by pressure infiltration for more than three decades. In the United States, intricately shaped Al-70vol% SiC electronic circuit substrates have been produced competitively by pressure infiltration. Production of tungsten reinforced copper for electrical contacts is another old application of the process. Figures 4 and 5 show examples of the preforms used in PIP and microstructures of metal matrix composites fabricated by the process.

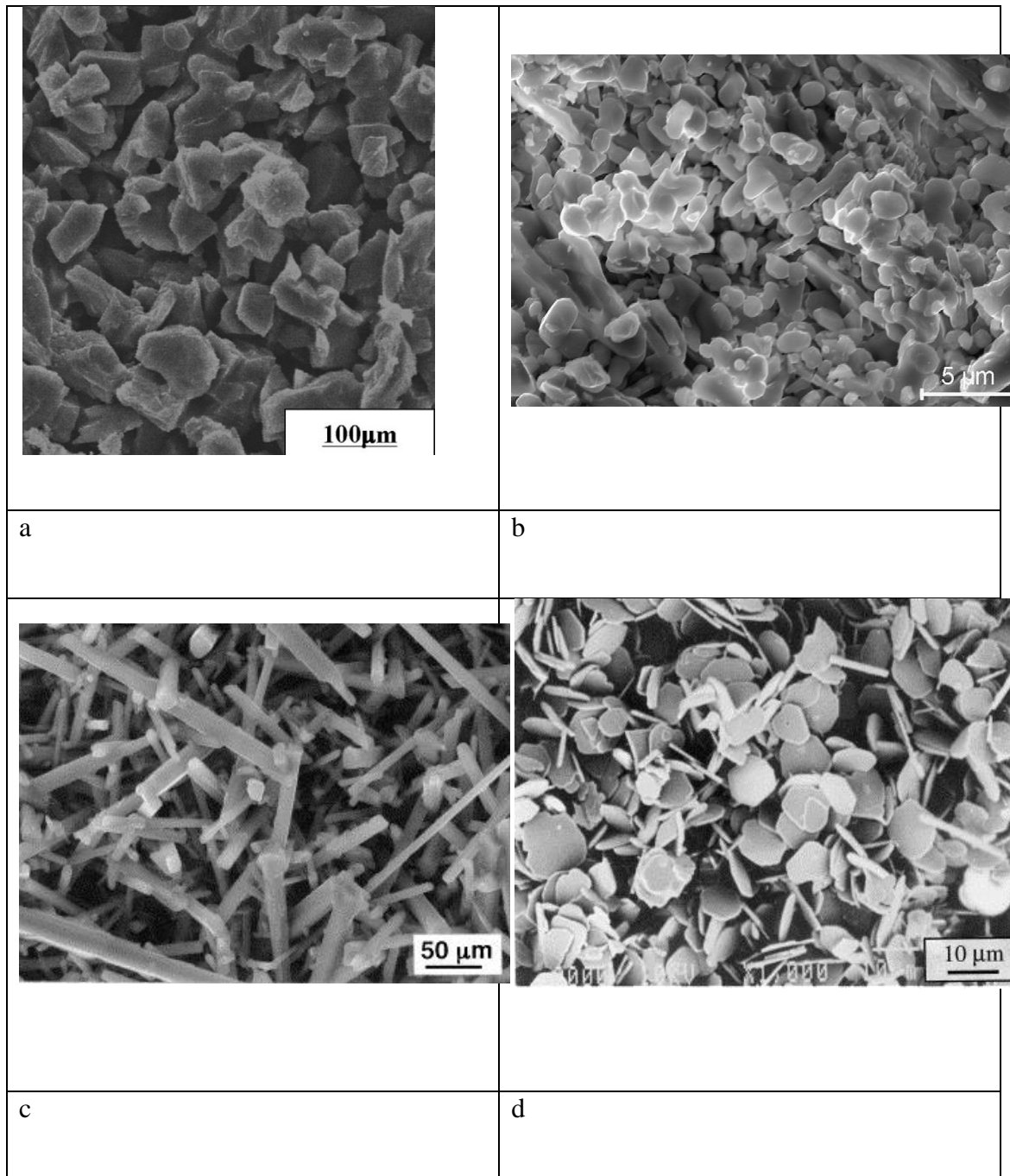


Figure 4. Micrographs of a) SiC particles [86], b) Al₂O₃ particles [87], c) aluminum borate whiskers [88] and d) Alumina platelet [89] preforms used in different pressure infiltration processes. (These figures are replicated here with permission from "Elsevier").

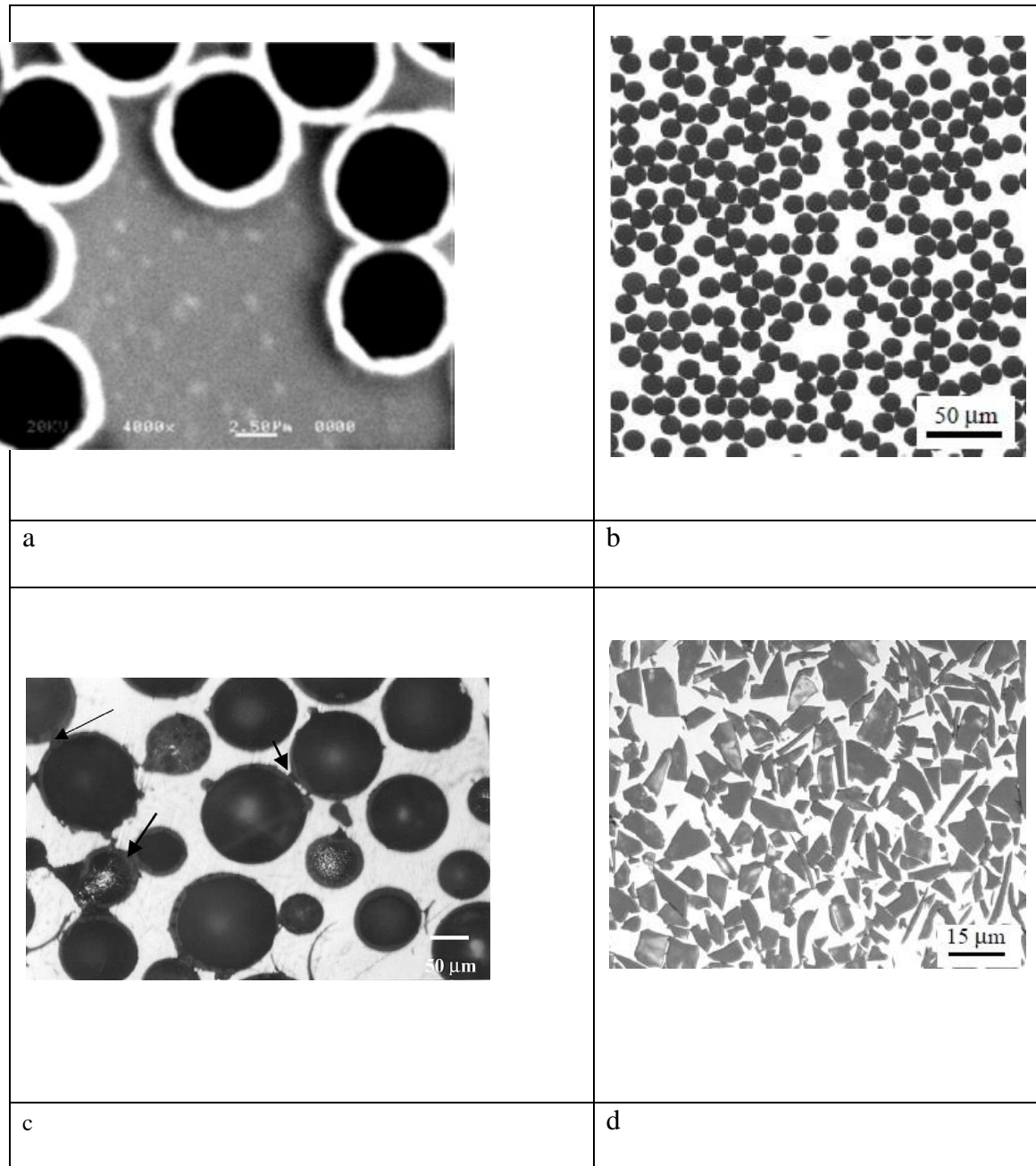


Figure 5. Micrographs of aluminum alloy matrix composites fabricated by pressure infiltration process. Preforms are made from a) nickel coated carbon fibers [90], b) Altex (γ -Al₂O₃) fibers [91], c) fly ash cenospheres [68] and d) SiC particles [91] (These figures are replicated here with permission from “Springer” and “Elsevier”.)

PRESSURE INFILTRATION METHODS

Depending on the pressure source, there are two main methods used for pressure infiltration in non-wetting systems, i.e. the mechanical pressure infiltration in which pressure is directly applied on the melt by a piston, and the gas pressure infiltration in which pressurized gas is employed to generate the required pressure for infiltration [92]. In these processes, the molten metal is forced into the preform using hydrostatic pressurization of the melt. Some other infiltration methods use a directional force to force the melt into the preform. These include the Lorenz force infiltration, ultrasonic infiltration, and centrifugal infiltration which can sometimes be used for continuous MMC production [92] .

GAS PRESSURE INFILTRATION

The basic gas pressure infiltration technology was originally developed at the Massachusetts Institute of Technology as a research tool because the processing parameters such as preform temperature, infiltrating metal temperature, infiltrating pressure and cooling rate could be accurately controlled [93]. In this process, fiber, whisker or particulate preforms are placed in inexpensive throw-away containers into which molten metal is forced through gas pressure. Since gas pressure produces a quasi-hydrostatic pressure condition in the container, the strength requirement of the system is minimal [94]. The process has been used to produce both MMCs [70, 95, 96] and intermetallic matrix composites [97, 98], and has evolved into an eligible industrial process to produce MMCs. The original patent was issued in 1970s [99]. The process invented by Cochran and Ray [100] included the heating of the preform in a mold under a vacuum into which molten metal was introduced through gas pressure. In fact, the molten metal penetrates into the

preform with the aid of an externally applied gas pressure to overcome the adverse capillary forces. The gas used has to be inert with respect to the metal matrix. The typical pressures used are in the order of 1 to 10 MPa. Use of higher pressures has also been investigated for aluminum-matrix composites [101], but safety issues then become a major limiting factor [76].

There are three different variations of the process. In the first method, a heated preform is dipped into the melt and then a gas pressure is applied to the melt surface to cause it to penetrate the preform. The gas pressure can be selected based on the wettability of the preform, which in turn is a function of the type and volume percentage of the reinforcement. In the second variation of the process, the gas pressure is applied on the melt surface in order to force it up a tube to infiltrate the preform. Schematic of such a gas pressure infiltration apparatus is presented in Figure 6 [68]. In the third variation of the process Figure 7, the metal billet is placed on top of the preform in a crucible in the heating chamber. The preform is sometimes covered with a thin refractory felt. First, the chamber is evacuated to remove the air in the preform. Upon heating, the metal melts and seals the crucible, after which the gas pressure is applied on the melt to infiltrate it into the preform.

Other variations of the gas-pressure infiltration apparatus concern the relative position of the heating element and the pressure vessel. In some designs, all the elements are placed inside the pressure vessel while in others, which are more suitable for isothermal infiltration of low-melting point metals such as aluminum, the furnace is located outside the pressure vessel.

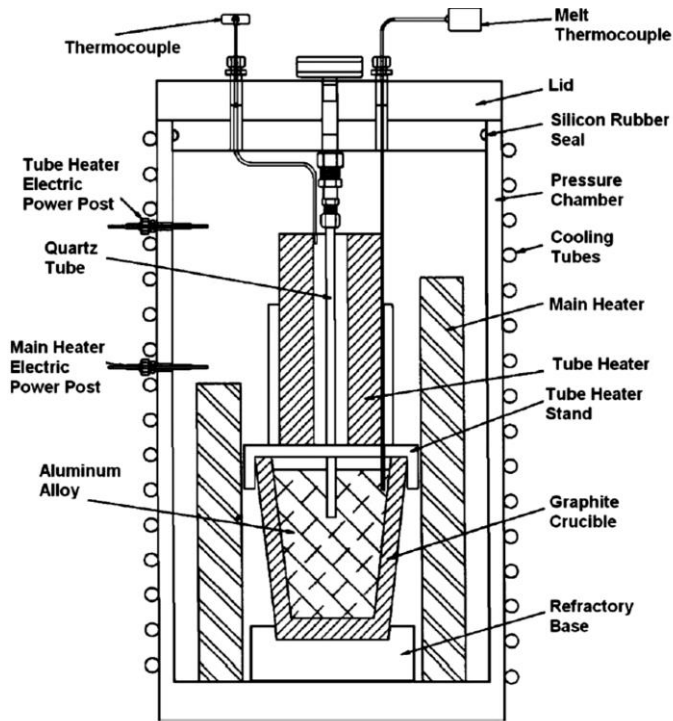


Figure 6. Schematic of a bottom filling gas pressure infiltration apparatus [68]

The four main steps in a typical infiltration cycle are shown in Figure 8. These include:

- 1) Preparation of the reinforcement, generally as a porous preform with interconnected pores, and placing it in the pressure chamber,
- 2) Melting the metal and preheating the preform to slightly above the melting temperature of the matrix material usually after evacuating the preform to avoid entrapment of gases,
- 3) Infiltrating the preform with molten metal, and
- 4) Solidification of the matrix

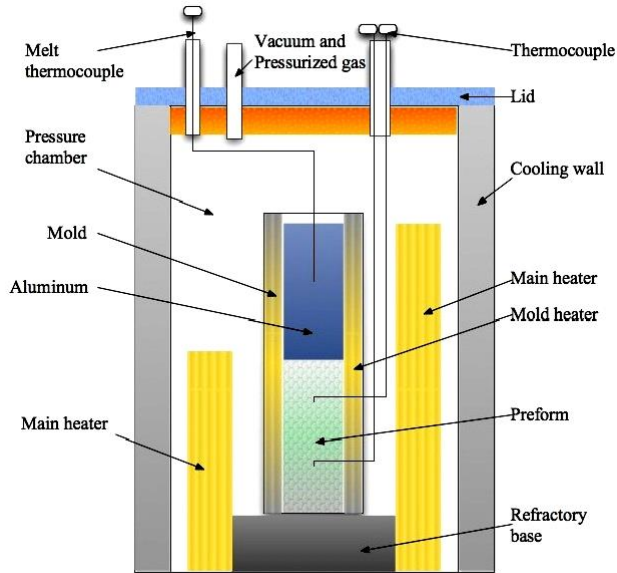


Figure 7. Schematic of a top filling gas infiltration process [102]

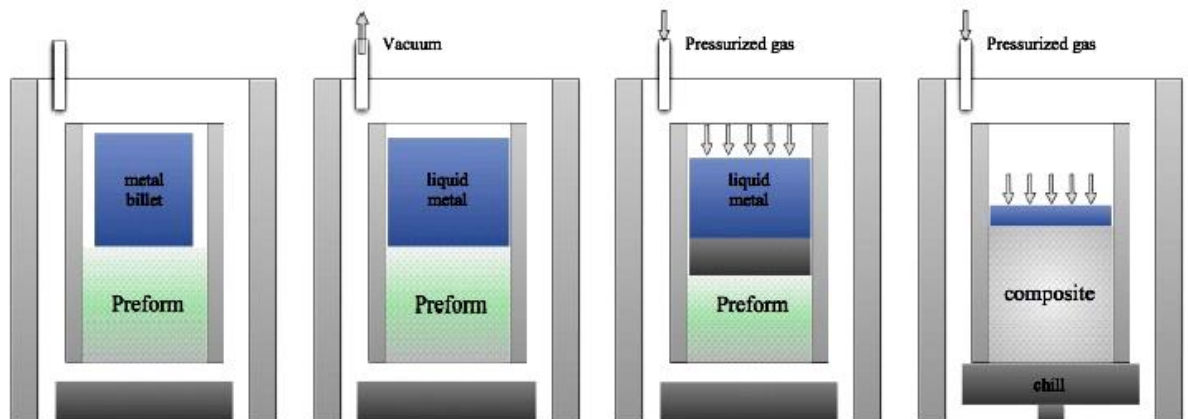


Figure 8. A schematic of the liquid metal gas infiltration process, showing the four basic stages [102]

Following the solidification of the matrix, the system is depressurized and the cycle is thus completed. These steps can be easily followed in batch processing. The method allows for using non-coated reinforcements due to short contact time of the reinforcement and the molten metal. It also results in less damage to the preform compared to the mechanical infiltration processes.

Although gas pressure infiltration is highly controllable for research purposes, it is not suitable for fast throughput because the pressure chamber is tied up for long times for melting of the matrix metal and then cooling down of the composite part upon completion of pressure infiltration and solidification. Moreover, the available space inside the pressure chamber is limited because the heating elements and insulation occupy a lot of space. To overcome these shortcomings, Metal Matrix Cast Composites Inc. (MMCC) has developed a patented process for the purpose of mass production [46]. The main feature of this process is that melting of the metal and heating the preform takes place outside the pressure chamber so that the pressure chamber is no longer a bottleneck for mass production.

Blucher et al. [85, 103] also developed a novel continuous infiltration process for the production of continuous fiber-reinforced MMC wires of up to 65% volume fraction reinforcement and few millimeters in diameter. The employed fibers include Al_2O_3 , Si-Ti carbide, SiC, and carbon fibers. The produced composite wires which are believed to be suitable for the introduction of fiber reinforcements into aluminum castings as well as the production of double composite, sandwich and preferentially reinforced structures. Mechanical tests have shown significantly higher load carrying capacity of the structures reinforced with the composite wires compared with the structures reinforced directly with fibers or structures without any reinforcement.

MECHANICAL PRESSURE INFILTRATION

Mechanical pressure infiltration includes the two main methods of squeeze casting infiltration and pressure die infiltration.

SQUEEZE CASTING INFILTRATION

Squeeze casting infiltration is a pressure infiltration method for liquid state fabrication of MMCs using a movable mold part (ram) for applying mechanical pressure on the molten metal [104]. The molten metal is forced to penetrate into a preform-dispersed phase placed in the lower fixed mold part. The applied pressure, which is maintained during solidification of the matrix metal, is generally much higher than those in the gas pressure infiltration processes and ranges from about 10 to 100 MPa or even higher. The method is a direct adaptation of the established squeeze casting process used for near-net-shaping of unreinforced molten metals and reinforced metal slurries produced by dispersion methods [105-107].

Squeeze casting infiltration is the most common technique employed for the commercial production of MMCs. Composites produced by this method are generally believed to have a pore-free matrix. However, it has been recognized that to avoid air entrapment in poorly vented preforms and porosity in the composites, very high pressures are required [104].

Application of high pressure may induce preform deformation or breakage during infiltration, as is often observed experimentally [108-112]. To avoid this problem, this process often consists of two stages. In the first stage, the molten metal is pressed into the preform at a lower pressure to avoid too fast infiltration that may damage the preform. Then a higher pressure is applied during the solidification phase to create a fine-grained high quality structure with minimum porosity.

Figure 9, illustrates the first variation of this method, i.e. direct squeeze casting infiltration.

Direct squeeze casting infiltration process follows the following steps:

- A preform of dispersed phase (particles, fibers, woven) is placed into the lower (fixed) die half,
- A predetermined amount of molten metal is poured into the lower die half,
- The upper (movable) die half (ram) moves downwards, touches the melt surface and forces the liquid metal to infiltrate the preform (Figure 9a),
- The infiltrated material solidifies under pressure (Figure 9b), and
- The part is removed from the die by means of the ejector pin (Figure 9c).

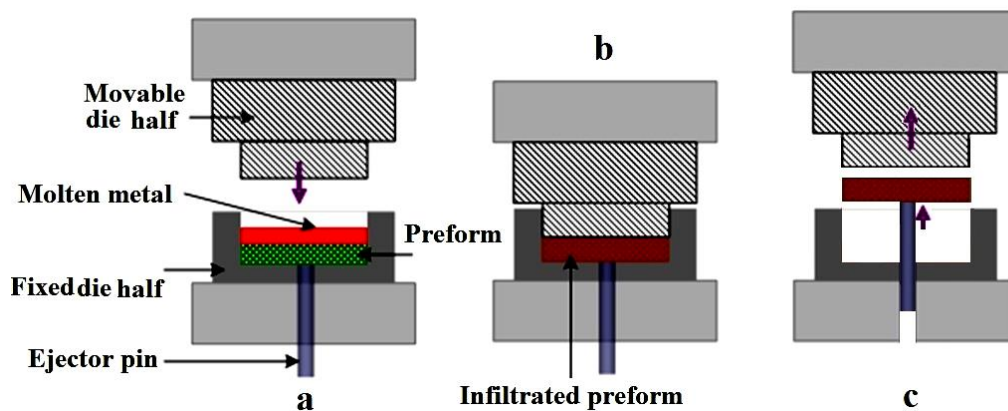


Figure 9. Direct squeeze casting infiltration

Figure 10, shows the second variation of the process, i.e. indirect squeeze casting infiltration. Note that in this method, the parting line of the die may be vertical and the die is bottom filled through a gating system. First, the vertical shot sleeve tilts to accept a measured amount of molten metal from a ladle and returns to its vertical position (Figure 10.a). Then a piston pushes the molten metal into the die cavity and the preform (Figure 10.b). At the end of the stroke, a high-pressure intensification is applied. When the solidification is complete, die opens and the infiltrated preform is removed.

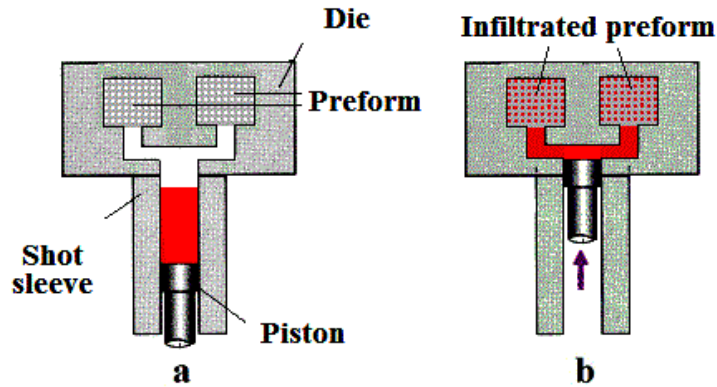


Figure 10. Indirect squeeze casting infiltration

The direct method is used for manufacturing relatively simpler parts with aspect ratios (height to section thickness ratio) not greater than 2.5:1 [113]. An example of such products is the automotive engine pistons made from aluminum alloys and reinforced by alumina short fibers in selected areas [2]. The advantages of this method are application of pressure on all parts of the composite throughout the solidification, simplicity of the die and the squeeze casting machine, and near 100% casting yield. The indirect method has less shape limitations. However, the mold and the casting machine is more complicated and expensive, and the casting yield is lower. Pressure has to be applied through a gating system, which may have a solidification time less than the composite itself. In such a situation, the final stages of solidification of the composite may not occur under pressure, increasing the risk of microporosity formation in the hot spots of the composite. Moreover, the casting of wrought alloys, which very often suffer from low casting fluidity, may be challenging. In both methods, all or part of the casting can be reinforced.

The main processing parameters for squeeze casting infiltration include applied pressure and infiltration speed, the reinforcement/melt contact angle, reinforcement spacing,

permeability of the preforms, melt temperature, die and preform temperatures, and viscosity and chemistry of the liquid metal. Influence of processing parameters on infiltration has been investigated by many researchers. Aguilar-Martinez et al. [114], for example, investigated the effect of SiC particle size, SiC type and Mg content on the degree of infiltration in an Al-Si-Mg-SiC_p system using experimental and statistical methods. Their results show that particle size is the parameter that most significantly affects the degree of infiltration, followed by magnesium content in the alloy. Regardless of the type of SiC, the degree of infiltration increases with increase in the magnesium content and the rate of increase is higher for high-purity green SiC (GC-SiC) than black SiC (CSiC) usually containing unreacted SiO₂ and C as impurities. Although the degree of infiltration increases with Mg content for all particles sizes, the effect is more significant for preforms made from smaller particles.

Squeeze casting infiltration has also been used for synthesis of metal reinforced MMCs. For instance, Lapin et al. [115] squeeze infiltrated aluminum into steel fibers and studied the formation of iron aluminides on the interface and the matrix. They found that volume fraction of intermetallic phases increased when the fiber volume fraction and size decreased. Increasing the die, melt and preform temperatures improved the infiltration, avoided premature choking of the preforms, and increased the extent of exothermic reactions.

Gas pressure infiltration process involves contact times on the order of tens of seconds to a few minutes between the reinforcement and liquid metal at high temperatures. This may result in unwanted reactions and phases, such as formation of Al₄C₃ on the reinforcement/matrix interface in Al-SiC and Al-C systems. Squeeze casting infiltration

process, on the other hand, typically involves lower infiltration temperatures and much shorter infiltration times followed by rapid solidification.

It must be noted that characteristic differences of different processes may call for tailored alloy design. For example, Beffort et al. [116] studied the effects of alloying elements and heat treatment on the microstructure and mechanical properties of high volume fraction Al-SiC_p MMCs produced by squeeze casting infiltration. They showed that when squeeze casting infiltration was used for infiltration of high purity aluminum in SiC preforms, the formation of Al₄C₃ was widely prevented owing to the non-equilibrium conditions prevailing during solidification. Surprisingly, however, magnesium addition to the melt under similar condition led to the formation of Al₄C₃. It was argued that silicon released from direct reaction between aluminum and SiC reacted with magnesium to form Mg₂Si. This reaction decreases silicon activity and favors the formation of Al₄C₃ in squeeze cast AlMg-SiC_p composites. The embrittling effect of the interfacial reaction products will counterbalance any potential positive effect of magnesium on interfacial bonding strength and the mechanical properties of the composite. Beffort et al. showed that while single addition of magnesium catalysed Al₄C₃ formation, addition of Cu or (Zn+Mg) provided opportunities to enhance the composite strength.

Long et al. [117, 118] studied squeeze casting infiltration of an aluminum alloy melt in preforms made from Saffil chopped fibers. Their experimental results indicated that during infiltration, the melt preferentially penetrated into the large interspaces in the preform whose degree of saturation was dominated by local infiltration pressure and that variation of the saturation degree at a given infiltration depth was determined by fiber distribution uniformity at the microscopic level. They also statistically established the relationships

between the melt flow and process parameters, and discussed distribution of stress and saturation as well as porosity and defect formation due to air entrapment in the preform during infiltration [117-119].

Long et al. [120] also indicated that premature melt solidification during pressure infiltration of fibrous preforms must be avoided as it results in non-uniformity in chemical, microstructural and mechanical characteristics as well as non-infiltration defects and weak matrix-fiber bonding of the cast composites. They suggested that preforms should be preheated to a temperature above the liquidus temperature of the melt. According to their findings, increasing the melt superheat, rather than eliminating the problem, induces a high temperature gradient in the casting, which prompts shrinkage and microsegregation defects during post infiltration solidification.

PRESSURE DIE INFILTRATION

Pressure die infiltration is another mechanical infiltration method for liquid state fabrication of MMCs. In this process, which is adapted from the die-casting technique for unreinforced metals [110, 121, 122], a preformed dispersed phase (particles, fibers, woven) is placed into a die which is then filled with a molten metal entering the die under the pressure of a piston and through a gating system to infiltrate the preform. Schematic of the process is shown in Figure 11.

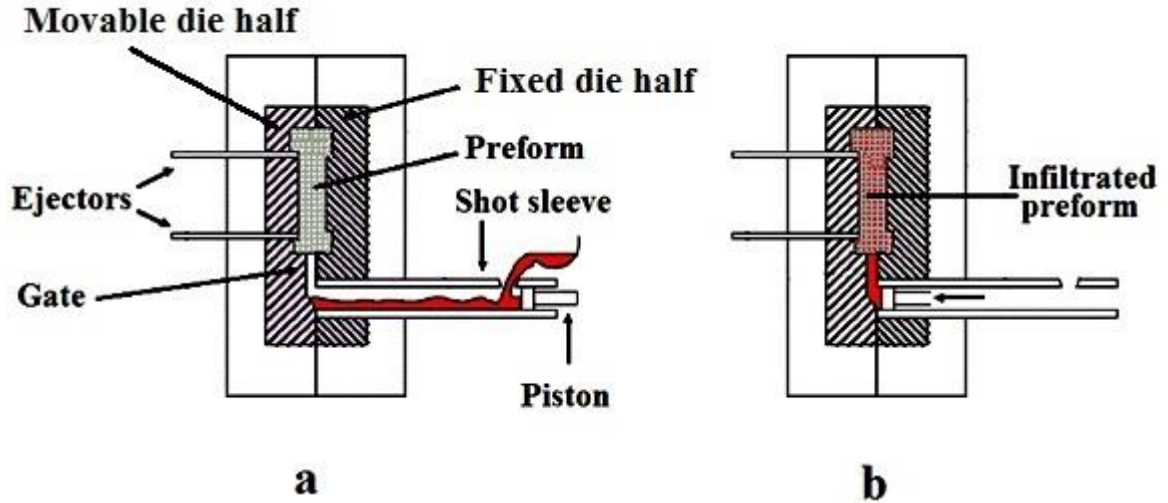


Figure 11. Schematic of the pressure die infiltration: a) before infiltration and b) after infiltration.

The main advantage of pressure die infiltration process is that net or near-net shape components can be mass produced using conventional pressure die casting machines. Similar to squeeze casting infiltration, the contact time between the reinforcement and the molten metal is short and solidification is fast. Therefore, more reactive materials can be used in comparison with gas pressure infiltration or dispersion methods [123]. However, similar to the squeeze casting infiltration, rapid prototyping of the components is not possible and care must be taken to avoid preform deformation and breakage or premature solidification of the gating system [120]. Using hybrid preforms has been suggested to overcome the problem of preform breakage [33, 34, 89].

Long et al. [91] studied the dependence of matrix void formation on the processing parameters and geometry of the gating system in a high pressure infiltration system and showed that a proper gating system design is crucial to obtain sound castings. They showed that with a conventional narrow gating system, the melt solidification is completed first in the gating system, thus isolating the partially solidified composite casting from the

pressurized melt reservoir in the injection chamber. This resulted in formation of internal shrinkage voids as well as seaming of the casting surface despite the use of a 100 MPa infiltration pressure. To eliminate shrinkage voids in the matrix, the gating system should be optimized to ensure a sequential solidification from the far end of the composite casting to the melt reservoir in the injection chamber through the gating system. Furthermore, the preforms preheat temperature and the melt superheat should be selected to avoid premature melt solidification. They recommended 750-800 °C preform preheat and 800 °C melt superheat for pressure infiltration casting of AlCu₄MgAg /Saffil composites with a 280-300 °C die temperature and strict process timing. In order to prevent preform damage, the infiltration speed should be selected in such a way that the pressure on the preform during infiltration is kept below the elastic compression strength of the preform. For the infiltration of Saffil preforms in their chosen infiltration system, they recommended infiltration speeds of less than 100 mm/s.

OTHER INFILTRATION PROCESSES

There are a few other infiltration methods that use a directional force to force the molten matrix into the preform [124]. In Lorenz force infiltration, the electromagnetic forces are used to assist infiltration of the melt into the preform. However, the preform position must be suitably oriented with respect to the force axis. In ultrasonic infiltration, highly-transient pressure pulses created by an ultrasonic probe in contact with the melt are used to overcome the adverse capillary force and wetting difficulties. In centrifugal infiltration, the forces created by rotation of the melt and the preform about an axis of rotation propel the melt

inside the preform. All these processes have been used for batch as well as continuous production of non-wetting MMC systems such as aluminum-carbon fibers [18, 20].

In addition to all above mentioned pressure infiltration techniques, vacuum assisted infiltration has also been used for some matrix-reinforcement systems. However, since the magnitude of the negative pressure that can be achieved is limited, vacuum infiltration is usually coupled with other techniques to enhance the infiltration process.

1.2 MODELING OF RESIN FLOW THROUGH DUAL-SCALE FIBER MATS AND POROSITY FORMATION DURING LCM PROCESSING OF POLYMER MATRIX COMPOSITES

INTRODUCTION

In pressure infiltration process (PIP) for making metal matrix composites (MMCs), liquid metal is injected under pressure into a mold packed with reinforcing fibers. PIP is very similar to the resin transfer molding (RTM) process, which is used for the manufacture of near-net shaped parts out of polymer matrix composites [125]. Both are characterized as liquid molding processes and consist of the following steps: 1) Dry fiber preforms made out of fabrics or fiber mats are placed in the mold. 2) Liquid matrix (monomeric thermosetting resin such as unsaturated polyesters or epoxies for PMCs, and molten metal or alloys for MMCs) is injected into the preform. 3) The liquid is allowed to harden through temperature control of the mold (exothermic thermosetting reaction for the resin and phase change for the metal). 4) The final net-shaped composite part is removed from the mold. An important advantage of the liquid infiltration processes is the production of near-net

shape composite parts from preforms designed using different reinforcements for optimal mechanical and other properties [125, 126]. The use of the woven or stitched fabrics as reinforcements is increasing as they provide a convenient way of improving the mechanical properties by ensuring higher fiber volume fractions through clustering of fibers as fiber tows or bundles. Porosity¹ is a major defect found in these fabricated composites, which adversely affects their fatigue properties.

The phenomenon of porosity formation during the making of MMC using PIP from 3D-woven reinforcements (classified as dual-scale porous media in the next section) has not been addressed in the literature. However, one can find large literature on porosity formation mechanisms in such dual-scale reinforcements during the manufacture of polymer matrix composites using RTM, which, as mentioned before, is a very similar to PIP used for the synthesis of MMCs.

To study the mechanisms of porosity formation in MMCs reinforced with 3D-woven fabrics, a thorough understanding of the physics of infiltration process is necessary. After a review of research done so far in the simulation and modeling of PIP, and the similar RTM process (which is the pre-requisite to understanding porosity formation mechanisms), a brief review of the research conducted on porosity formation in MMCs will be presented. The review reveals a gap in the literature, in terms of the theoretical/computational explorations and experimental investigations, on the effects of the dual-scale nature of woven, braided or stitched fabrics used as reinforcement in MMCs on metal flow in PIP and the resultant porosity formation. Thus, in this study, results of a series of experiments,

¹In this study, the term “void volume fraction” is used to quantify the void space inside a preform as a fraction of the total preform volume, while the presence of voids inside the composite will be referred to as the “porosity”.

conducted using the gas PIP for making MMC samples after varying the material and process parameters, will be presented. The effects of the processing parameters, such as the infiltration pressure (i.e., the net pressure applied on the infiltrating metal), the infiltration temperature (i.e., the temperature of the infiltrating metal), and the matrix shrinkage, on porosity formation in MMC samples are studied.

Liquid composite molding (LCM) is a cost effective process for manufacturing net-shaped parts from fiber reinforced polymer composites. LCM includes processes such as Resin Transfer Molding (RTM), Structural Reaction Injection Molding (SRIM), Vacuum Assisted Resin Transfer Molding (VARTM), and Seemann Composites Resin Infusion Molding Process (SCRIMP) [127].

Woven and stitched fabrics inherently induce a dual-scale flow behavior since they are comprised of the distinct macro- and micro-flow regions, each with different impregnation/flow rates corresponding to the different permeability values. The pores of the macro region (to be also called the inter-tow region as it comprises of the large spaces found between fiber tows or bundles) are much bigger and will fill more rapidly, while the pores in the microscopic region (to be also called the intra-tow region as it comprises of the smaller pores found between individual fibers) inside the tows will saturate more slowly. This order-of-magnitude difference in the pore length-scales in the same medium is the basis for their classification as a “dual-scale” porous medium [128]. Due to the delay that occurs in the complete saturation of the preform, the distinction between these separate macro- and micro- flow regions is important. The macro flow-front first fills the more permeable pores between the tows and then the fluid from this region fills the less permeable pores within the tows. At this point, the more slowly advancing micro flow-

front dictates the filling progress. Therefore, in a dual-scale porous medium, the location of the macro flow-front seldom coincides with the boundary of the fully saturated region of the preform. For these preforms, a partially-saturated region exists behind the macro flow-front in which the pores of the inter-tow region may be filled but the fiber tows are still just partially filled. In case of the one-dimensional overall flow created in a preform, a partially saturated length, L_s , can be defined as the distance between the macro flow-front and the fully-saturated secondary ‘front’ as shown in Figure 12 [129, 130]. This partially-saturated length decreases as the intra-tow permeability of fiber tows gets closer to the inter-tow permeability. The coexistence of these micro- and macro- flows due to the dual-scale nature of the preform has well-documented effects on resin flow during the RTM processing such as the porosity formation [130-132] and the existence of a partially-saturated region behind the flow front [130, 133-137].

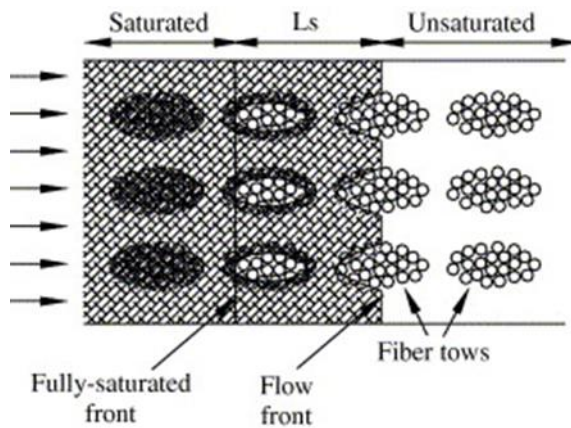


Figure 12. A schematic depicting the saturated, partially saturated (L_s), and unsaturated flow regions within dual-scale preforms, and highlights the delayed impregnation of the fiber tows [130].

Many RTM mold-filling simulations have been developed in an effort to optimize the mold filling process and to avoid incomplete filling of RTM molds and the resultant dry spots or

porosity formation in composites. These numerical simulations are accomplished by incorporating the fundamental balance laws for the conservation of mass, momentum, energy and species into the physics of resin flow through the fibrous preform. In most LCM simulations, the flow of resin is considered as the flow of a Newtonian fluid through a *single-scale* porous medium. It is also assumed that a sharp front exists between the wet and dry portions of the porous medium during infiltration, and the flow behind the front is considered fully saturated. With this assumption, the following equations {Darcy's law, Eqn. (1); Continuity Equation, Eqn. (2)} for single-phase flow are applicable for modeling the resin flow:

$$V = -\frac{K}{\mu} \cdot \nabla p \quad (1)$$

$$\nabla \cdot V = 0 \quad (2)$$

Here V is the volume-averaged Darcy velocity, K is the permeability tensor for the preform, μ is the viscosity, and p is the pore-averaged resin pressure [128]. Note that the gravity term in Darcy's law is ignored as this term is small in the high-pressure infiltration conditions found in PIP and RTM molds. Using the quasi steady-state approximation, the pressure distribution behind the front can be calculated using an elliptic equation, which is obtained by substituting the expression for Darcy velocity from, Eqn. (1), in the continuity equation, Eqn. (2):

$$\nabla \cdot \left(\frac{K}{\mu} \cdot \nabla p \right) = 0 \quad (3)$$

The resin flow is a non-isothermal flow due to the single or multiple exothermic chemical reactions occurring as the resin state changes from liquid to solid during its curing. Since the resin viscosity has a dependence on both the resin temperature and the state of resin cure, the equations for predicting resin temperatures and resin cure in the preforms have also to be solved simultaneously. (These equations are not listed here, but have been described in detail by Dessenberger and Tucker [138]). However, this physics developed for single-scale porous media characterized by a mono-modal pore-size distribution is not applicable to the case of woven or stitched fabrics, which are characterized as dual-scale porous media and are marked by a bi-modal pore-size distribution. During resin flow in RTM, the latter displays the presence of unsaturated regions behind the front, thus violating the assumption of the preform being fully-saturated.

There have been several attempts to develop RTM mold filling simulations for the dual-scale preforms [128, 130, 139, 140]. When the resin is flowing through such a media, it faces less resistance in the large pores between fiber tows than in the micro pores inside fiber tows, so it goes quickly around the tows and fills up the large pores before starting to penetrate the tows. These tows continue to absorb liquid after the macroscopic resin-front has passed, acting like sinks of liquid in the macroscopic flow field. To describe such flows, a new mass-balance equation has been proposed with a nonzero sink function on the right hand side of Eqn. (2) [128, 141]:

$$\nabla \cdot v = -S \quad (4)$$

Here S is the sink function equal to the volumetric rate of liquid absorption [128, 130, 139, 140].

Voids² in polymer matrix composites are formed when air bubbles are cast into the final composite in the form of permanent air pockets. Since the presence of bubbles signifies incomplete saturation of pore space by resin, the process of bubble formation and movement can be explained in terms of the unsaturated flow. Many experimental investigations have been conducted to study the mechanism of bubble formation at the microscopic level [142-146]. Bubble formation during the RTM process, is mainly caused by mechanical trapping of air rather than the presence of volatiles in the resin. Patel et al. [142] and Chen et al.[147] identified two basic types of bubbles or voids: (1) macrovoids, which are formed between the fiber bundles, and (2) microvoids which are formed inside the tows. The formation of voids was correlated with the capillary number { given later in Eqn. (6), Sec. 3.2}: for $Ca < 0.01$, the formation of macrobubbles is predominant as the wicking flow inside the tows is faster than the inter-tow flow; for $Ca > 0.01$, the creation of microbubbles is dominant since the inter-tow flow overtakes the wicking flow inside the tows [142]. As shown in Figure 13, $Ca = 0.01$ corresponds to a minimum in the percentage of voids formed during infiltration and forms the most optimum condition for resin injection in the mold.

² The term “void” used in the polymer matrix composites community is equivalent to the term “porosity” used in metal matrix composites community, and represents the dry spots present in the matrix.

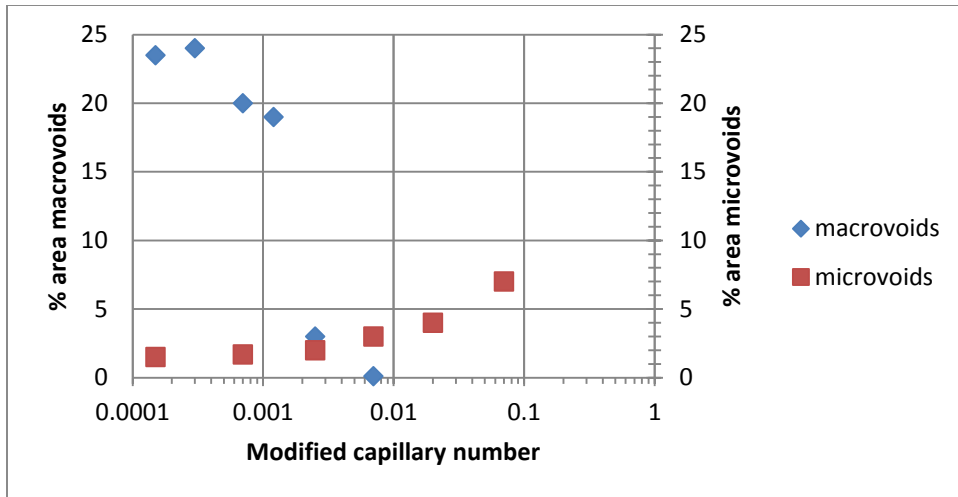


Figure 13. Percent area macro- and microvoids as a function of modified capillary number in RTM (This approximate graph is based on the information provided in reference [148].)

Many authors have developed “tow impregnation” models to predict the microvoid formation inside fiber bundles. In many of these models, fiber tows are modeled as porous cylinders, which are impregnated radially by a microfront of resin after the macrofront has quickly engulfed the surrounding gap region. Parnas and Phelan [130] used this concept to develop the flow equation for dual-scale fabrics where they predicted cylindrical air bubbles, following the ideal gas law, forming inside the tows as a result of the microfront movement. Fong and Advani used the same approach and predicted a rather unrealistic, almost uniform distribution of voids in a 1-D LCM mold [149] while the actual bubble distribution is like a step function near the macroscopic front [132]. Chan and Morgan also predicted void formation in a bi-directional mat [139]. Chen, Macosko, and Davis used the simplistic linear impregnation physics of Washburn to propose a similar model [147] which could qualitatively predict the off-centered, non-cylindrical voids seen in the experiments [145]. Chang and Hourng used Darcy’s law in both the intra and inter tow regions to

numerically study the bubble formation in cylindrical tows [150]. These models have some deficiencies such as (1) the absence of any physics for bubble mobilization, (2) the assumption of cylindrical geometry for the tows (rather unrealistic since tows in woven fabrics are like wavy thick threads with elliptical cross-sections) leads to unrealistic void-distribution predictions.

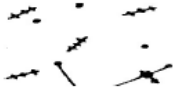




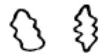

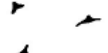
The formation and migration of bubbles near the flow front is an indication of a two-phase (resin and air) flow through the porous media and can be explored within the classical theoretical framework for multiphase flows in porous media. Hahn et al. used a transient mass-balance equation for the diffusion of saturation to predict the distribution of saturation near a very slow moving front [151]. Mohan et al. developed a pure finite element-based algorithm for mold filling in LCM using the concept of fill-factor which is similar to saturation while they assumed a zero pressure for the unsaturated region [152]. As mentioned before, Patel et al. conducted a series of studies on bubble creation and migration [142] and linked the dual-scale nature of fiber mats to the types of bubbles observed near the flow front. They observed *small micro-bubbles* (or micro-voids) inside the tows at high resin velocities when the macro front in the gaps led the micro-front inside the tows, and *large macro-bubbles* (or macro-voids) in inter-tow gaps at low speeds where the liquid front inside the tows is ahead of the liquid front in the gaps. Patel and Lee modeled the bubble formation using a two-channel model while using the conventional equations for multiphase flow [153, 154]. Their model was quite successful in the prediction of macrobubble distribution at very slow speeds, but not in prediction of microbubbles at relatively rapid resin injections typical of the RTM process. Departing from the usual tow-based models, Pillai and Advani qualitatively predicted the formation

and migration of bubbles at the macroscopic level by using the “shock” in the transient saturation distribution predicted by the Buckley-Leverette (B-L) equation [155]. The B-L formulation is a first-order hyperbolic equation and is based on the two-phase flow of resin and air in single-scale porous media, which included the generalized Darcy’s law for averaged momentum balance and a transient saturation-based equation for mass balance. Chui et al. later applied the same B-L formulation numerically and were able to predict the step-like porosity distribution observed near the macroscopic flow fronts in fabrics [156].

1.3 POROSITY FORMATION IN CAST METAL MATRIX COMPOSITES DURING PRESSURE INFILTRATION PROCESS

Porosity in cast metal matrix composite (MMC) has been known as a defect affecting the enhancement of strength. From previous reviews, among the causes of porosity formation are air bubbles entering the melt matrix material, water vapor on the reinforcement surfaces, gas entrapment, evolution of hydrogen and shrinkage during solidification. Many studies had shown that processing parameters are the main factors affecting porosity formation. Optimum properties of cast MMC are attained with least porosity content. Generally, increasing porosity content in MMC will decrease the mechanical properties such as tensile strength, Young’s modulus, Poisson ratio, and damping capacity. The presence of porosity decreases the mechanical properties of cast MMC as the failure process is initiated from the voids formed [157].

Table 4. Four different types of pores, their development and characterization in the solidifying casting of Al-7Si-Mg [158].

Types of pores	Round pores	Long, broad pores	Long, fissured pores	Small, fissured pores
Solidification process and bubble formation.	 <p>Bubbles formation in liquids</p>			
Pore morphology in the structure.				
Characterization:	<ul style="list-style-type: none"> - Precipitation in the liquid melt or in the beginning of solidification. - Unrestricted bubble growth. - High H₂ concentration required. 	<ul style="list-style-type: none"> - Bubble formation with still high liquid fraction. - Arrangement between growing bubbles and dendrites. - High to medium H₂ concentration. 	<ul style="list-style-type: none"> - Bubble formation during formation of the dendrite network. - Bubble expansion limited by still open melt channels. - Medium to low H₂ concentration. 	<ul style="list-style-type: none"> - Precipitation shortly before the end of solidification. - Shape and size of pores determined by closed interdendritic spaces. - Low H₂ concentration.

As was discussed in previous sections, the liquid metal infiltration process for fabrication of metal matrix composites is very similar to RTM process. It consists of the injection and subsequent solidification of liquid metal within interstitial spaces of a fibrous preform, which is a very complex process. Essentially three classes of phenomena govern the infiltration process: fluid flow and capillarity, transport/mechanical phenomena and heat flow and solidification [159]. The capillarity forces dictate the initial path of the flowing liquid metal to the preform. Transport phenomena during infiltration govern the

temperature and solute distributions at and behind the infiltration front. Often mechanical compression of the preform also happens during infiltration and finally the solidification of the metal matrix creates the final MMC part. All these phenomena including metal and heat flow, species transport, preform deformation and segregation of alloying elements, the chemical interfacial reactions and so on happen during infiltration.

PROCESS SIMULATION IN PRESSURE INFILTRATION PROCESS

Although a great number of experimental efforts in the last few decades have shed light to many of these aspects, the complexity of the interactions of the mentioned phenomena calls for more rigorous analysis of the infiltration process. Therefore, various efforts have been dedicated to numerical simulation of the pressure infiltration processes. For such complex phenomena, the mathematical analysis and numerical simulation may allow prediction and understanding of many features of the infiltrated composites. In addition, numerical models have been developed to predict the appearance of defects in the end products and optimize the mold design and processing parameters.

Due to complexity of the infiltration process, for realistic simulations, pressure infiltration process must be modeled in a coupled manner in three dimensions. A quantitative understanding of pressure infiltration to enable process modeling and prediction of the composite microstructure requires an understanding of its governing physical laws. Several research groups have concentrated on this subject. The first attempt to model the pressure infiltration process can be attributed to Mortensen [160], where the traditional equations

for flow in porous media were employed to develop an analytical model to describe fluid flow and heat transfer during infiltration of fibrous preforms by a pure metal. The model included several simplifications. Use of such simplifications allowed the development of some analytical solutions for temperature and porosity distributions for a simple 1-D infiltration. Thereafter, several researchers made attempts to model the pressure infiltration process aimed at different physical laws by means of various numerical techniques. Table 5 summarizes some of these efforts.

Table 5. Summary of various works on mathematical modeling of pressure infiltration for making of MMCs.

Researchers, year	Models and remarks	Ref.
	Fluid flow: slug-flow, Darcy's law	
Mortensen, 1989	Heat transfer: no viscous dissipation of heat, Plane infiltration front, saturation behind front 1 Dimension, pure metal, phase change	[160]
	Fluid flow: Forseheimer equation	
Mortensen, 1993	Heat transfer: conduction, convection and changes in fraction solid Mass flow: neglect diffusion	[161]
	Fluid flow: Forseheimer equation, consider body force (Lorentz force) by exerted magnetic field	
Mortensen, 1991	1 Dimension	[162]
	Fluid flow: Darcy's law, low injection	
Dopler, 1998	Heat transfer: isothermal 1 Dimension	[163]
Dopler, 2000	Darcy's law, isothermal, similar to drainage phenomena in soil	[164]
Trochu, 1994	Darcy's law	
	Remeshing technique of the domain at every moment starting from the position of the flow front	
Mal, 1998		[165]
Kang, 1999	Control volume finite element method to calculate a filling volume	[166-
Bruschke, 1994	fraction and define the position of the front	168]
Joshi, 2000	Isothermal	
Lam, 2000	Non-isothermal	[169]
Kuan, 2000	Using VOF to track the front (donor-acceptor)	[170]
	A model based on the solution of 'equation assessment' and VOF, Darcy's flow	
Voller, 1995		[171]
Shojaei, 2002	Voller's model, control volume FEM	[172]
Lin, 1998	Voller's model, FEM	[173]

Sommer, 1996	Boltzmann transformation	[174,
Preziosi, 1996	Deformation porous medium, Darcy's law	175]
Ambrosi, 1998,		[176-
2000	Finite difference method	178]
Danis, 1999		
Michaud, 1999	Using bounding approach	[179]
Antonelli, 1999	Isothermal numerical simulation, Porous medium has a nonlinear elastic behavior	[180]
Gutowski, 1987	Consider the relation between stress and porosity	[181]
Chen, 2001	Propose a conceptual model for predicting the non-linear compaction behavior of fibrous preform	[182]
Jespersen, 2008	Isothermal steady state impregnation of a porous medium with a Newtonian fluid: Darcy's law; Thermoplastics composite processing, stress equilibrium, 1 Dimension	[183]
Lacoste, 1991, 1993	Phase change, pure metal Enthalpy method	[184, 185]
Voller, 1991	A source term is used to treat the phase change	[186]
Mantoux, 1995	A source term is used to treat the phase change	[187]
Tong, 1996	Slug-flow, Darcy's law, movement of the remelting front is governed by the energy conservation at the remelting front 2 dimension	[188]
Biswas, 1998	Similar to Khan's model	[189]
Lacoste, 2002	Coupled Darcy's law, VOF, phase change	[190]
Chang, 2006	Slug-flow model, Darcy's flow, Isothermal	[191]
Jung, 2008	Slug-flow model, Darcy's flow, enthalpy model, phase change	[192]
Mortensen, 1990	Alloy, Darcy's flow, heat transfer included a variation term of fraction solid, mass transport (ignore diffusion term), 1 Dimension	[193]

Tong, 1996	Alloy, 1 Dimension, Darcy's flow, phase change process is governed by	[188,
Khan, 1998	equilibrium phase diagram, mass transport (ignore diffusion term)	194]
Lee, 2007	Alloy, 2 Dimension, Darcy's flow, enthalpy model, phase change	[195]
Wang, 2013	3 Dimension, Darcy's flow, pseudo dual-scale approach was used to simulate the flow in the tows and between tows	[102]

As mentioned before, the liquid metal infiltration process in PIP for the fabrication of MMCs is very similar to the RTM process used for the manufacture of polymer matrix composites. It consists of the injection and subsequent solidification of liquid metal within interstitial spaces of a fibrous preform, which is a very complex process. Currently the liquid-state processes are preferred to other manufacturing techniques for MMC production as they are more economical while benefiting from the advantages of well-proven casting processes. It should be mentioned here that *MMCs produced by pressure infiltrations are considered to be in the category of cast composites.*

According to metallurgists and material scientists, essentially three classes of phenomena govern the infiltration process: fluid flow and 'capillarity', transport/mechanical phenomena, and heat flow and solidification [159]. The capillary forces (governing the 'capillarity') dictate the initial path of the flowing liquid-metal inside the preform. Transport phenomena during infiltration govern the temperature and solute distributions at and behind the infiltration front. Often mechanical compression of the preform also happens during infiltration and finally, the solidification of the metal matrix creates the final MMC part. All these phenomena, including metal and heat flow, species transport, preform deformation, segregation of alloying elements, chemical reactions at the metal-

fiber interface, and so on, happen during the infiltration of metal into the dry preform. As a result, for realistic simulation of the process, the PIP must be modeled in a coupled, multi-dimensional manner. During the past few decades, many researchers have tried to develop mathematical models and numerical simulations to predict and understand the flow during the PIP process to improve the quality of infiltration. The first and perhaps the most comprehensive attempt to model PIP can be attributed to Mortensen et al. [160]. The traditional equations for single-phase flow in porous media (Darcy's law and the continuity equation) were employed to develop an analytical model for fluid flow and heat transfer during infiltration of fibrous preforms by a pure metal. The model was based on several simplifications including the "slug flow" or sharp-front flow assumption, which means that the pore space behind a clearly-defined front is saturated with metal while the previously existing air has been squeezed out ahead of the front. After applying these simplifications, some analytical solutions were developed for the temperature and porosity distributions during a simple 1-D infiltration.

Numerical models have been developed to predict the appearance of defects in the end products and optimize the mold design and processing parameters. PIP mold-filling simulations have been confined to single-scale porous media so far and the verified flow effects in dual-scale fiber mats such as absorption/trapping of liquid metal by fiber tows or other possible flow effects such as premature freezing of metal after coming in to contact with colder tows, have not yet been studied. However, the use of woven or stitched fabrics (dual-scale porous media) is increasing as they provide a convenient way of improving the mechanical properties of MMCs through the inherently higher fiber volume fractions. As mentioned in the previous section, research in RTM has shown that there are some clear

discrepancies between the numerical predictions based on the single-scale porous-media models and the experiments observations of flow in dual-scale fabrics. Although significant research has been done to model resin flow and void formation in dual-scale preforms, *no equivalent work has been done in PIP to study the effect of dual-scale nature of the preform on metal flow and subsequent porosity formation.* Only recently, Wang and Pillai [196] developed a numerical simulation for pressure infiltration of dual-scale preforms. They addressed the dual-scale nature of the preform by assigning different permeabilities and void volume fractions to the inside (intra-tow) and outside (inter-tow) regions while using the same governing equations. Their results show an irregular flow front in dual-scale fabrics and an unsaturated region behind the front due to the formation of gas pockets inside the fiber tows.

Due to the complexity of defect formation mechanisms in the synthesis of MMCs by pressure infiltration, the production of porosity-free MMCs has remained a technical challenge. It has been demonstrated that the porosity defects are deleterious to the mechanical properties of cast MMCs and are adversely affected by the porosity content of the composite casting [197-199]. The control of such casting defects should be achieved through optimization of the casting temperature, temperature of the mold, pressure, and cooling rate [200]. Another source of porosity formation is poor infiltration. Assuming a complete infiltration, the other important source of porosity is metal shrinkage during solidification [199]. This problem is tackled by employing directional solidification toward a riser in a temperature gradient or by applying very high pressure during solidification [199]. The porosity defect is more significant in composites with high volume fraction of reinforcement because the high volume fraction of reinforcement hinders the flow of

interdendritic liquid as well as obstructs any bulk movement of the metal matrix in the semi-solid state during solidification. To avoid this defect, Al-Si alloys are recommended because of its good fluidity³ [201] and its compatibility with several reinforcements [199].

Apart from the normal casting porosity resulting from dissolved gases and shrinkage, there are additional causes related to the process. In cast composites, porosity can be classified into two types: (1) those away from the reinforcement inside the matrix, and (b) those at the boundary of matrix and reinforcement (See Figure 15). The second type of porosity is more undesirable because it leads to the debonding of the reinforcement from the matrix under low stress. In composites, gas porosity may nucleate heterogeneously on the surface of the reinforcement during solidification [202]. To summarize, the main sources of porosity formation in MMC castings are: (1) Gas entrapment due to incomplete evacuation of the preform during infiltration, (2) ‘Preporosity’ formation due to incomplete infiltration, (3) Precipitation of inclusions and dissolved gas present in the melt, and (4) Solidification shrinkage.

Gas porosity can be present in a casting when there is dissolved gas in the molten metal or alloy together with the presence of favorable nucleation sites. Hydrogen is the only gas known to dissolve to any significant extent in molten aluminum. During solidification, the gas is rejected at the solid/liquid interface and enriched at the later stages of freezing. Gas precipitation will only occur in presence of favorable nucleation sites as non-wetted or poorly bonded interfaces [203, 204].

³Fluidity in metallurgical terms is a material’s ability to flow into and fill a given cavity, as measured by the dimensions of that cavity under specified experimental conditions.

Solidification shrinkage occurs when the pressure gradient is insufficient to overcome the resistance offered by the reinforcement and dendritic networks to feed voids formed by matrix shrinkage during phase change. In their study, Ghomy and Campbell [204] concluded that as the number of effective pore nuclei increases in a casting, the central internal macro-pores, caused by solidification shrinkage, will disperse into fine micropores and the porosity will convert from external to internal. Other factors such as surface roughness, interface wetting, reaction, and so on, can also affect porosity [205] along with metal feedability [41].

While considerable literature is available on porosity formation in unreinforced metals or alloys and in powder technology, relatively little has been done to investigate porosity formation in reinforced castings produced by infiltration processing. Notable examples of studies done on porosity formation in MMCs include the works of Ray [202], Long et al.[119], Samuel et al. [41] and Emamy et al.[204]. High pressures used in MMC production generally suppress porosity formation, but such defects were detected in MMCs made at moderate pressures (10 MPa) by Mortensen et al.[206] and high pressures (100 MPa) by Asthana [207].

A study by Ilegbusi and Yang [208] investigated the effect of processing conditions and reinforcement characteristics, such as matrix alloying, reinforcement coating, and cooling condition, on the formation of local negative pressures and subsequent nucleation of shrinkage porosity after assuming a planar matrix/reinforcement interface in the pressure infiltration casting of metal matrix composites. Their results showed that the degree of susceptibility to porosity nucleation in the composite depends on the type of matrix/reinforcement system. For example, porosity nucleation in Al/Al₂O₃ system is found

to be more energetically favorable than the Al/SiC system. The appropriate application of metal alloying, such as Mg in the Al/Al₂O₃ system and Mg and Cu in the Al/SiC system, or reinforcement coating such as Cu coating on SiC, significantly reduces the contact angle and improves the wettability at the interface enhancing infiltration by increasing the pressure barrier to porosity formation. Increasing the void volume fraction of the preform as well as the reinforcement (particles/fibers) size also increases fracture pressure and improves the infiltration. They concluded this means there is a lower potential for porosity nucleation in fiber reinforced composites, which typically have larger reinforcement size than particulates and whiskers. In another study, Ilegbusi and Yang [205] investigated the mechanisms of porosity nucleation on five interfacial configurations shown in Figure 14 for a variety of matrix/reinforcement systems. They found that interfaces with negative curvatures such as the cavities are potential sites for porosity formation. Other effective methods to avoid porosity include careful control of the cooling condition as well as the applied pressure.

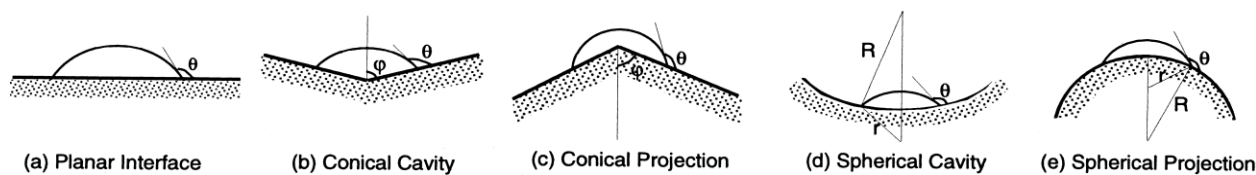


Figure 14. Five different interfacial configurations studied by Ilegbusi and Yang for porosity nucleation.

Calin et al [209] studied the effects of fiber volume fractions (f_{vf}) on porosity and thermal conductivity in Al-MgO particulate-reinforced MMCs of 5%, 10% and 15% f_{vf} produced by melt stirring. They observed that an increase in f_{vf} leads to an increase in the porosity.

As commented earlier, the interface between the matrix and reinforcement has a crucial effect on the properties of MMCs, which is affected during their fabrication. The interface related problems, which are system-specific, include the interfacial chemical reaction, degradation of the reinforcement, and the lack of wettability with the matrix. The nucleation of pores in MMCs is strongly dependent on the matrix-reinforcement interface characteristics. The modification of interface properties, such as the addition of alloy elements to a metal matrix, has been experimentally shown to suppress porosity formation [210]. Another effective way for interface modification is the coating of reinforcement to improve the interface wettability [211]. Rajan et al. [212] reviewed the surface treatment methods and coating work carried out on reinforcements such as carbon/graphite, silicon carbide (SiC), and alumina (Al_2O_3), and their effects on the interface, structure and properties of aluminum-alloy MMCs. The metallic coatings improve the wettability of the reinforcement, but change the matrix alloy composition by alloying with the matrix. Ceramic coatings reduce the interfacial reaction by acting as a diffusion barrier between the reinforcement and the matrix. Multilayer coatings have multiple functions, such as promoting wetting, acting as diffusion barrier, and releasing thermal residual stresses.

1.4 AIM OF THE PRESENT STUDY AND JUSTIFICATION

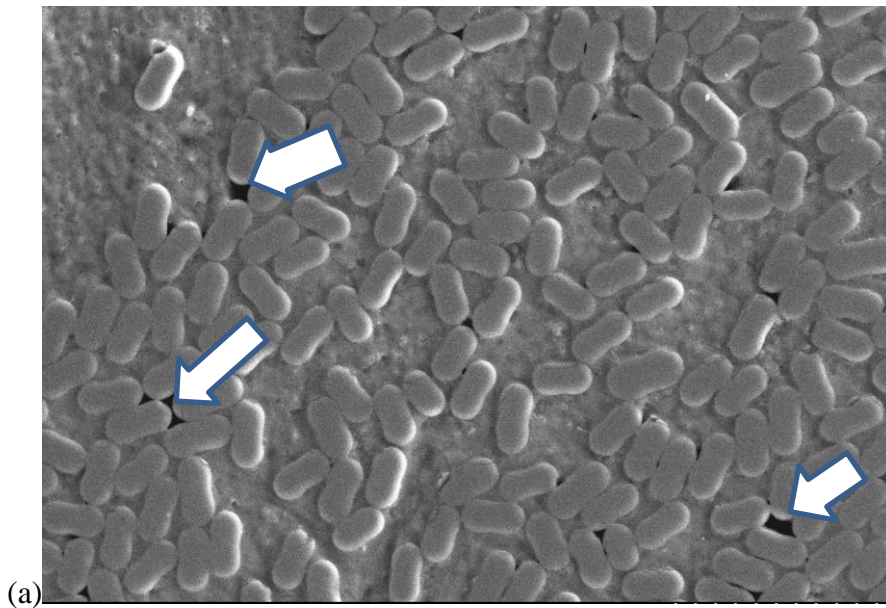
This brief literature review reveals that although significant research has been done on the phenomenon of bubble formation and migration in dual-scale preforms during the RTM processing of polymer matrix composites resulting in porosity in the final product, no equivalent research has been done so far to study the effect of the dual-scale nature of the preform on the metal flow during PIP and the resultant porosity caused by the delayed

impregnation of the fiber tows in this type of preforms. Flow visualization using transparent Plexiglas molds, which is a popular technique to study resin flow in RTM, is not possible in PIP because of the very high temperatures encountered in the PIP mold.

As a result, though significant research has been done to model resin flow and void formation in dual-scale preforms in RTM, *no equivalent work has been done in PIP to study the effect of dual-scale nature of the preform on metal flow and subsequent porosity formation*. Only recently, Wang and Pillai [196] developed a numerical simulation for pressure infiltration of dual-scale preforms. They addressed the dual-scale nature of the preform by assigning different permeabilities and void volume fractions to the inside (intra-tow) and outside (inter-tow) regions while using the same governing equations. Their results show an irregular flow front in dual-scale fabrics and an unsaturated region behind the front due to the formation of gas pockets inside the fiber tows. However no experimental validation of this preliminary effort has been done.

This work is the first attempt to study the mechanisms of porosity formation during gas pressure infiltration of metal into dual-scale ceramic preforms, and to study the factors affecting these mechanisms. The parameters affecting the infiltration process, can be classified into five groups: (a) fiber-preform properties (related to unit-cell structure, void volume fraction, pore size distribution, fiber and tow dimensions), (b) liquid-metal properties (surface tension and viscosity), (c) solidification-related (related to shrinkage, etc), (d) liquid/solid interface properties (the contact angle, surface reactivity, etc.), and (e) experimental conditions (applied pressure, infiltration time (which is defined as the

time during which the constant infiltration pressure is applied) , temperature and atmosphere of infiltration) [207, 213]. The aim of this work is to investigate the effect of some of these parameters on the porosity content in the Al-Si alloys/ 3D-woven Nextel fabric infiltrated using the gas PIP. Effectiveness of a new dimensionless parameter called the modified capillary number, which includes some of those above listed parameters in a dimensionless grouping, is also explored.



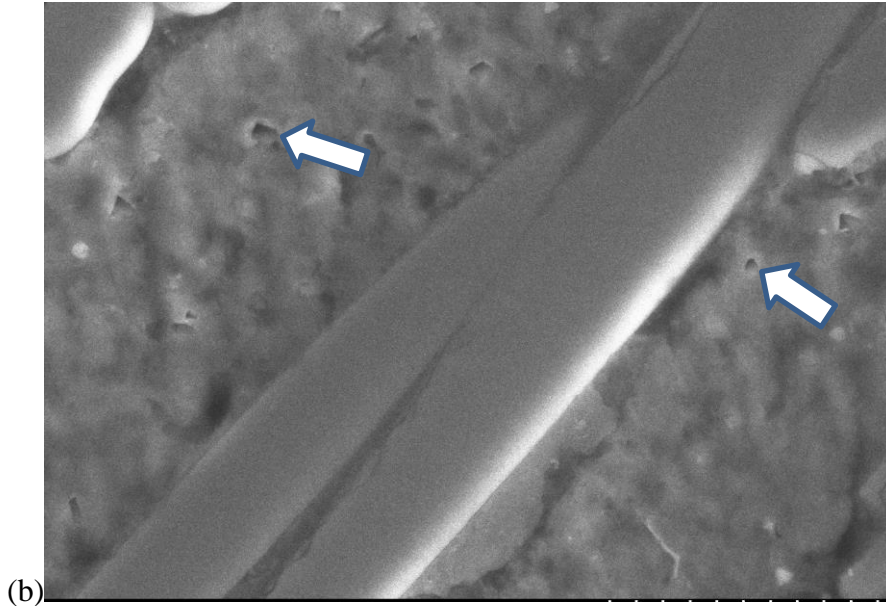


Figure 15. Scanning Electron Micrographs showing (a) porosity between Nextel fibers and also (b) porosity within the matrix .

Of the two types of PIPs, we will be studying the gas PIP (gas-pressure infiltration process) where a pressurized gas is used to push the liquid metal into the dry preform. The processing conditions have a major influence on the porosity content of MMC composites synthesized by the gas PIP. Another major source for porosity formation during this process is solidification shrinkage, which happens during the metal phase change. In the present study, the effect of changes in the processing parameters of infiltration temperature and pressure on the porosity content of MMC samples synthesized by gas PIP is studied. In addition, the effect of matrix shrinkage on the porosity content of MMC samples is explored by using a zero-shrinkage alloy as the matrix.

CHAPTER 2: INSTRUMENTATION AND EXPERIMENTAL PROCEDURE

A series of Experiments were conducted using the gas pressure infiltration process (i.e., the gas PIP) to make MMC samples corresponding to different material and processing parameters. The effects of the above mentioned parameters, such as infiltration pressure, infiltration temperature, and matrix shrinkage, along with the capillary number on the phenomenon of porosity formation in MMC samples were studied.

Molten Aluminum alloy was infiltrated into preforms made of a 3D woven fabric using a pressurized gas in our PIP setup. The supplier of the 3D Nextel weave was 3TEX Inc. The weave was cut into 2.3 in x 2.3 in square pieces and then heat cleaned by a specific process recommended by the manufacturer to remove the sizing and other contaminations. It was then placed at the bottom of a square steel tube, which was used as the mold with cross-section dimensions of 2.3 in x 2.3 in and height of 5 in. The inner surface of the mold was coated with a thin layer of graphite to avoid reactions between the metal and mold surface. Then a specific amount of the alloy was placed on top of the preform inside the mold. After that, the mold was placed inside our gas PIP apparatus (see Figure 16) which was then used for the gas- pressure infiltration of Al alloys into the preforms. The pressure chamber is made of an 18 cm inside diameter, 19.7 cm outside diameter, and 27.5 cm long steel cylinder. The lid assembly and the bottom portion of the chamber are made of 2014 Al alloy. The lid and steel cylinder have copper tubing for water cooling. The melting furnace is composed of two semi-cylindrical heating elements. The apparatus can handle infiltration pressures up to 300 psi through the pressurized inert Argon gas. After placing the mold inside the pressure chamber, the lid was closed and the vacuum pump was turned

on to evacuate the furnace, and then the heater was set at the specified temperature. After reaching that temperature and waiting for an hour to equilibrate, the metal was infiltrated into the preform by applying gas-pressure. In order to perform a constant-pressure infiltration experiment, the pressure was increased as fast as possible to the chosen value and then it was kept constant for half an hour during the infiltration process. (This time is called the infiltration time which was kept constant during these experiments.) After this period, it was abruptly reduced to atmospheric pressure through the pressure relief valve. Later the lid was removed and the sample was left to cool down. The resulting MMC pieces were cut and their densities were estimated as a measure of the porosity content in each sample. The fabricated samples were then further studied using the optical microscope and SEM. For this, the specimens cut from the castings were ground and polished using our automatic polishing equipment; the final polishing used the $0.25\mu\text{m}$ silica colloid to obtain the best possible surface.

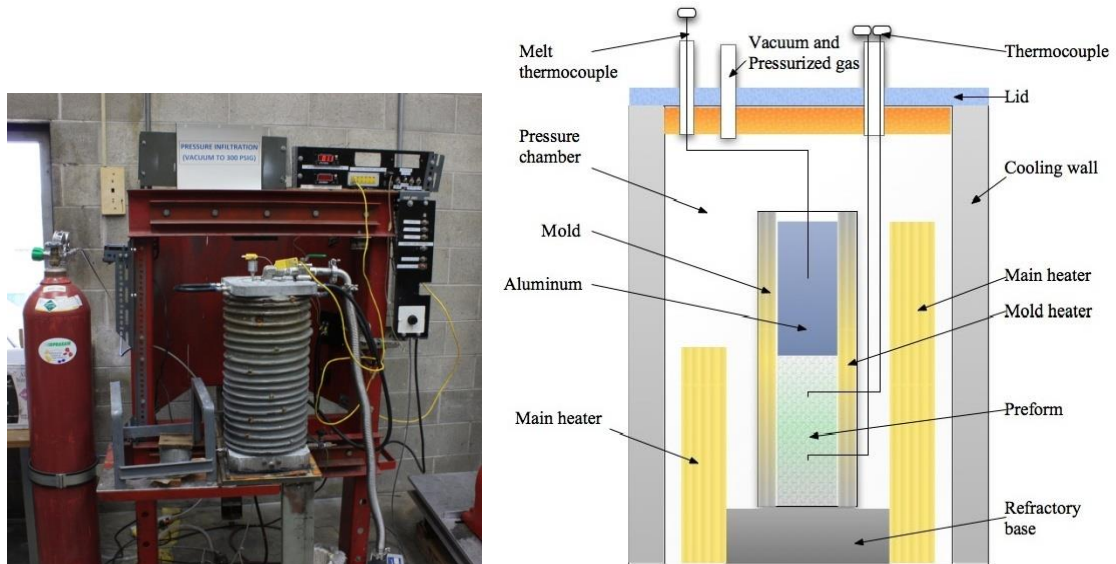


Figure 16. Gas pressure infiltration equipment and its schematic.

In this work, Al-Si alloys (A356 and Mercusil) were selected as the matrix materials for our MMCs made using the gas PIP. Their chemical compositions are shown in Table 6. A356 alloy is an important alloy in automotive and other applications. Its density is 2.685 g/cm^3 , and its solidus and liquidus temperatures are 555°C and 615°C , respectively. To study the effect of matrix shrinkage on the porosity content in the composite, a hypereutectic Al-Si alloy with zero volume shrinkage [214] was used as the matrix in some of our experiments. This alloy, called Mercusil, was made by stir casting and its chemical composition was confirmed by ICP (inductive couple plasma) analysis. The Nextel 3D-woven fabric produced by 3TEX Inc. was used as the preform for reinforcement purposes and the main properties of its fibers are listed in

Table 7. The 3M™ Nextel™ 720 fiber, composed of 85% alumina and 15% silica, offers the lowest creep of any Nextel™ Fiber at temperatures up to 2102°F (1150°C).

Table 6. Chemical composition of Aluminum alloys A356 and Mercusil

Alloy	Element (Wt. %)						
	Si	Mg	Ti	Fe	Cu	Mn	Al
A356	6.5-7.5	0.34	0.013	0.08			Bal.
Mercusil	20-30	0.4-1.6		1.4	0.25	0.3	Bal.

Table 7. Important properties of 3M™ Nextel™ 720 ceramic fibers

Property	Unit	Nextel 720
Sizing color	color	Green
Chemical Composition	Wt. %	85 Al ₂ O ₃ 15 SiO ₂
Melting Point	Celsius	1800
Filament Diameter	μm	10-12
Crystal size	Nm	<500
Density	g/cc	3.40

As shown in Figure 17, the 3D weaving incorporates multiple layers of warp and fill yarns in a single fabric. In the non-crimp 3D orthogonal weaving, invented at North Carolina State University, the fabric is composed of a number of warp and fill direction tows, with the latter being one more than the former. The yarns aligned in the length direction, called the Z yarns, traverse multiple fill and warp layers, looping over the top fill yarn, then going through the fabric thickness, and then going under the bottom fill yarn, and finally pulling the warp and fill layers together. The Z yarns thus create a 3-D weave pattern. The yarns consisting of 3M™ Nextel™ 720 fibers were used in this pattern to create the Nextel 3D fabric. The fabric thickness was approximately 3mm and its architecture was based on six warp yarns per inch, seven fill yarns per inch, and the Z yarns. A schematic of the weave pattern and a magnified cross section of the 3M's 3D-woven Nextel fabric are shown in Figure 17.

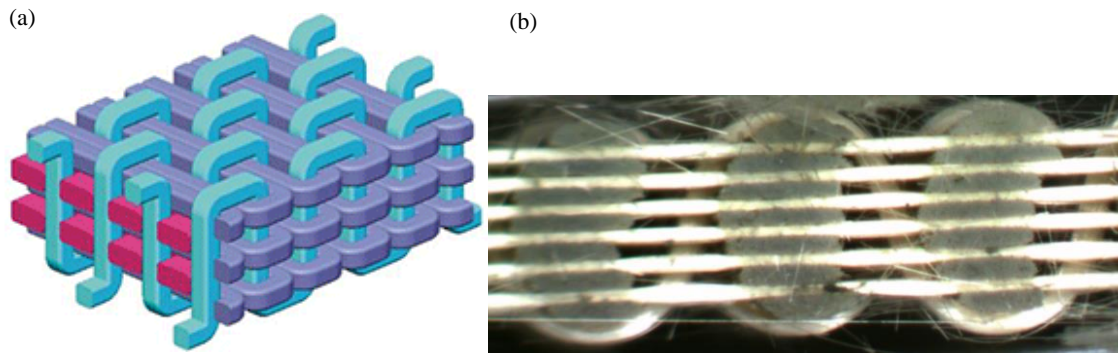


Figure 17. (a) Non-crimp orthogonally woven alumina fabric with 3D weave pattern [215],(b) Longitudinal cross section of the 3D woven Nextel fabric with 10X magnification.

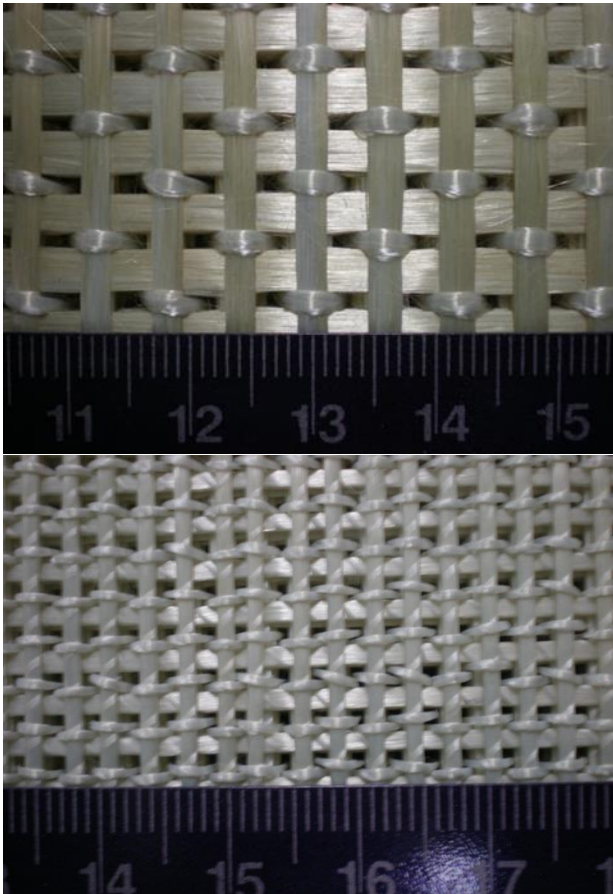


Figure 18. Different patterns of 3D woven Nextel fibers. Tighter pattern has more inherent structural integrity and may produce stronger and stiffer composites

Some advantages for using 3D-woven Nextel fabrics as reinforcements include:

- Non-crimp fiber architecture leads to higher strength composites
- Simultaneous multiple fill insertions speed production
- Best suited for relatively flat shapes
- Thicknesses of 0.1” at widths up to 120 inches
- Thicknesses to 2 ½” at widths up to 24”

PRESSURE INFILTRATION SET-UP

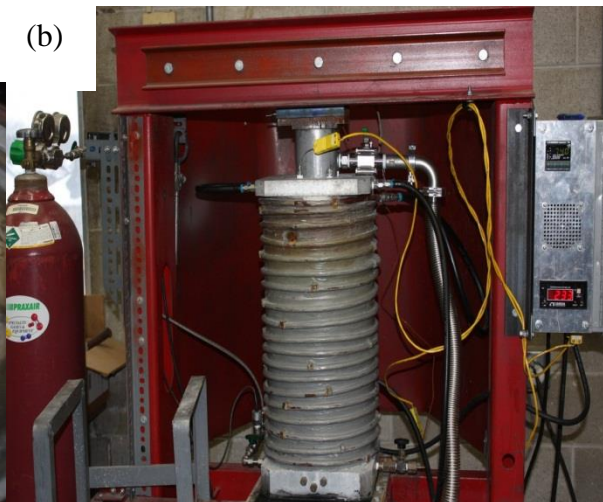
Experiments were done in a Pressure infiltration set-up in UWM Composite Material Lab.

This pressure infiltration set-up can apply an infiltration pressure up to 300 psi (20.41 atm, 2.068 Mpa).

(a)



(b)



(c)



Figure 19. (a) Samples being heated in the furnace under vacuum followed by pressurizing with Ar.(b), (c) Pressure infiltration setup available at the Composite Center, University of Wisconsin-Milwaukee

TEMPERATURE MAP OF THE FURNACE

To investigate the temperature distribution inside the furnace, three thermocouples were inserted at different heights inside the furnace. These thermocouples were fixed in place through fittings inserted in the ports located in the top cap. The first thermocouple attached to channel ai5 is located 12 in below the lid and the temperature curve for which is recorded with green color. The second one located 11 in below the lid and its temperature curve is drawn in red color and finally the third thermocouple was attached 9 in below the bottom of the cap. Its temperature curve is specified with white color. One more thermocouple was also inside the furnace that was connected to temperature control unit of the furnace. A schematic of the set-up is presented in the Figure 20. After the completion of the set-up,

the furnace was turned on and temperatures were recorded by defining a Labview Signal Express project for temperature acquisition. Results are shown in the Figure 22, which shows a maximum temperature difference of 10 C between these points in the furnace. So it was concluded that during PIP experiments, the infiltration temperature can be assumed constant and equal to the value shown on the system temperature screen.

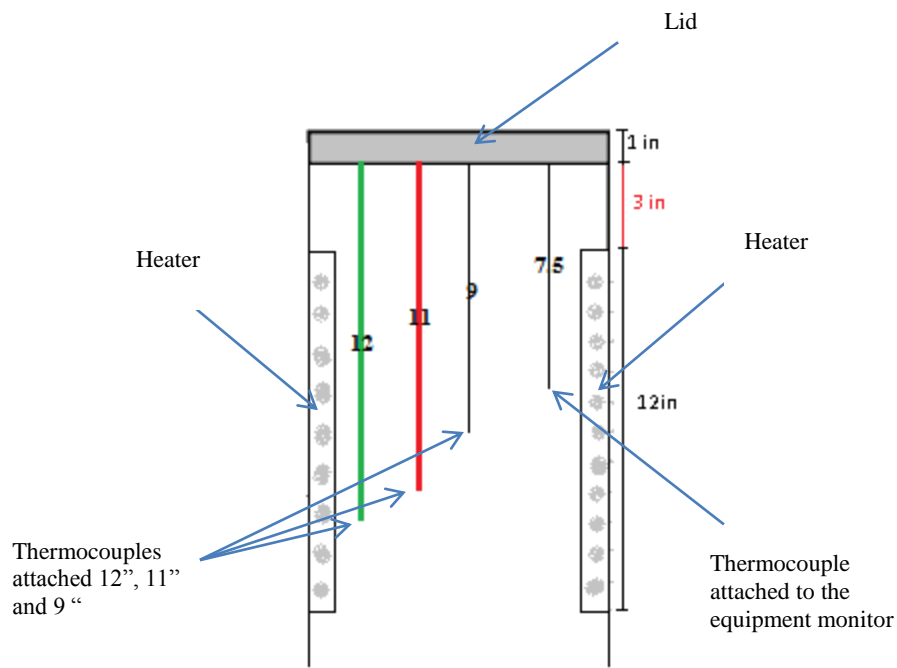


Figure 20. Experimental set-up for investigating the temperature map of the furnace



Figure 21. Labview Signal Express software was used to find the temperature map of the furnace.

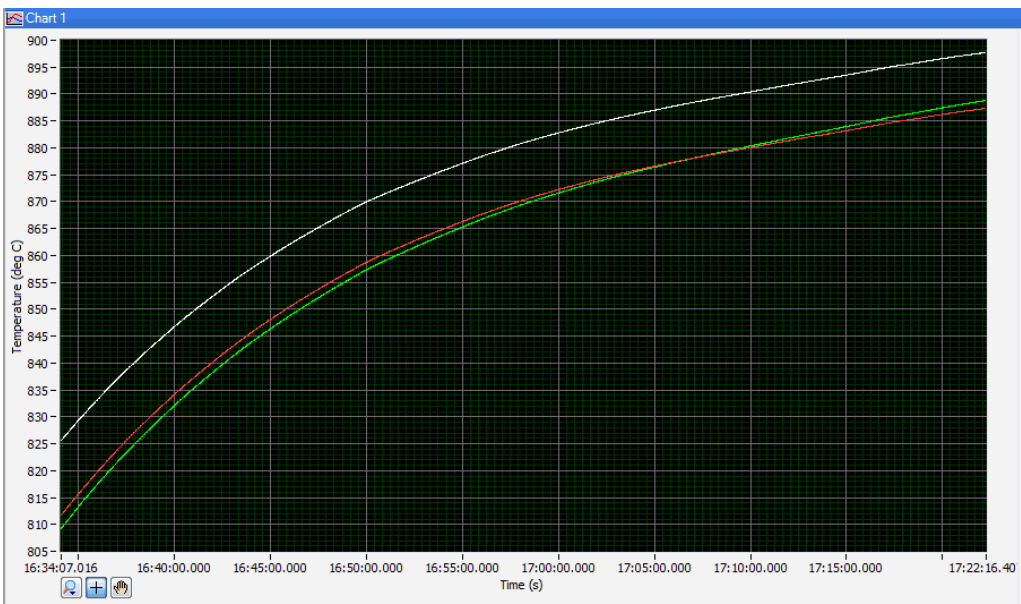


Figure 22. Resultant Temperature map of the furnace

EXPERIMENTAL PROCEDURE

The procedure to perform an experiment follows these steps:

1. Preparation of alloys by stir casting
2. Preparation of preform (diamond saw cutting, sizing burning)
3. Preparation of mold: mold machining and welding
4. Pressure Infiltration
5. Metallographic sample preparation of the sections

PREFORM PREPARATION

3D woven Nextel fibers were used as preform in the experiments. First step in preform preparation is to cut the fiber mat according to the mold dimensions. After that, the Nextel Ceramic textiles should be *heat cleaned*. Heat cleaning was used to remove all of the organic coatings from the surface of the Nextel Fibers.

MOLD

A square steel tube supplied by Speedy Metals is used as the mold (Figure 23). The mold is coated with a refractory material (Zirconia wash, graphite, boron nitride, etc) to prevent reaction between melt and crucible (Graphite was used in these sets of experiments). Reinforcement was placed into the tube and then Yttria Felt was placed on top of the preform to prevent reactions between the melt and reinforcement during heating.



Figure 23. Square tube that was used as mold in the experiments.

The typical procedure in conducting an experiment was as follows:

1. *Fabricate the mold.* Square cross-sectioned hollow steel tubes were procured from Speedy Metal, Inc. They were bottom welded and then the internal surfaces were coated with a refractory material (Zirconia wash, graphite, boron nitride, etc) to prevent reaction between melt and crucible.
2. *Cut the fiber according to mold dimensions.* In the present study, dimensions were 2.3"x 2.3".
3. *Heat-clean the fiber preform.* In the present study, the cut Nextel fiber preform was heated first to 250°C for 1 hour followed by heating at 500°C for 1 hour and finally keeping at 700°C for 20 minutes to remove the sizing.

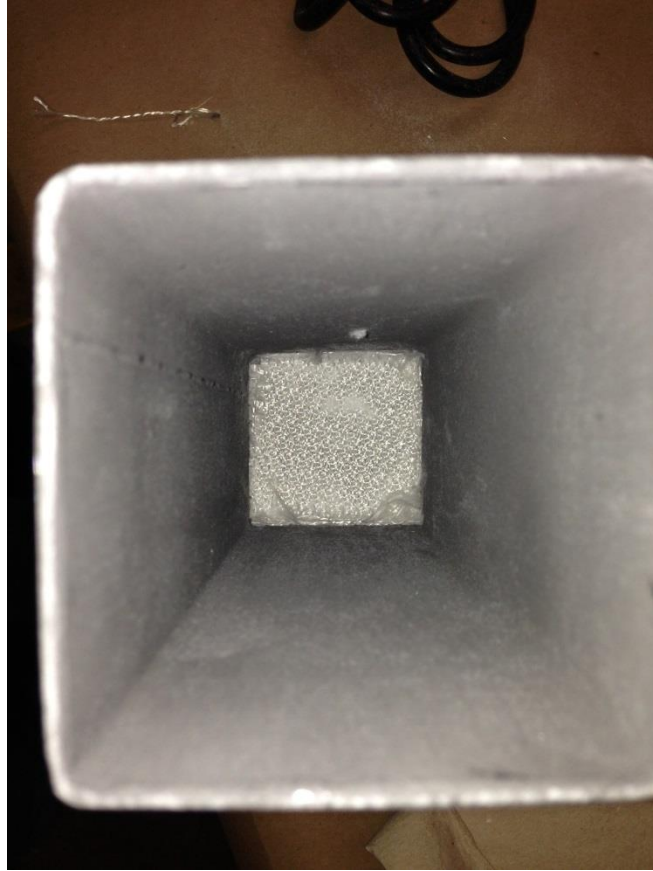


Figure 24 .The reinforcement is placed at the bottom of the mold.

4. *Insert the fiber into the bottom welded tube mold.* (Figure 24)
5. *Prepare alloys for matrix material.* The matrices were A356 and Mercusil alloy [214]. Mercusil alloy was prepared by stir mixing and casting into rods that would fit in the mold. Its chemical composition was confirmed by ICP (inductive couple plasma) analysis.
6. *Insert a filter (Yittria felt) on top of the preform and then the cast matrix alloy to the mold containing the preform.*



Figure 25. After placing the filter on top of the reinforcement, the metal is placed on top of the filter inside the mold.

7. *Place the mold in the center of the PIP furnace.*
8. *Cover the top with ceramic plate and close the lid.*
9. *Evacuate the furnace and turn on the heating to the planned temperature for the experiment⁴.*
10. *Wait for an hour after reaching the infiltration temperature for equilibrium and then infiltrate the metal into the preform by applying gas-pressure.*
11. *Shut down the furnace.*

⁴ Vacuum pressure could not be monitored due to the limitation of our setup. Moreover, it was difficult to maintain the vacuum due to leakage. Hence, very likely only partial vacuum was created inside the chamber.

12. *Wait for 30 min and release the pressure using the relief valve.*
13. *Take the mold out and let it air cool.* (It may be quenched or furnace cooled based on preference for the desired microstructure.)

The sample thus prepared was milled out from the mold. It was a square piece of about 2.3"x 2.3" with 0.118" thickness. A square piece of 1"x 1" was cut from the sample for further analysis including density measurement and also preparing samples for micrographs and SEM pictures.

CHAPTER 3: RESULTS AND DISCUSSION

The experiments conducted using the 3TEX Nextel preform infiltrated with A356 alloy at different pressures and temperatures are summarized in Table 8 (See Appendix A for details). The initial void volume fraction of the Nextel weave was measured to be 65%. Each experiment S_{ij} (Table 8) was repeated three times. The density of the MMC samples, synthesized using gas PIP at different processing conditions specified in Table 8, were measured with direct Archimedian method using the Mettler Toledo standard level analytical balance with its density determination kit (See Figure 26) . In this method, the density of MMC samples was determined with the aid of a reference liquid (here distilled water) whose density ρ_0 is known. The sample were weighed first in the air, and then in the reference liquid. The density could be calculated from these two weights as

$$\rho = \frac{A}{A-B}(\rho_0 - \rho_L) + \rho_L \quad (5)$$

where ρ is the density of the MMC sample, A is the sample weight in air, B is the sample weight in distilled water, ρ_0 is the density of the reference liquid, and ρ_L is the air density (0.0012 g/cm³).

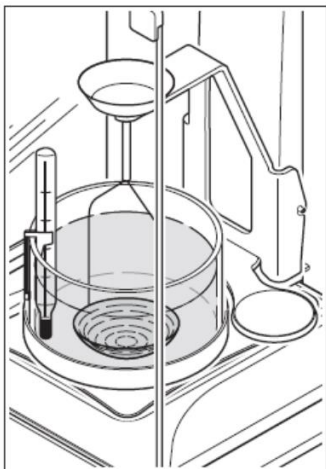


Figure 26. Mettler Toledo standard level analytical balance with density determination kit.

Then the relative densities were calculated, which were the actual densities as percentages of the theoretically maximum density (the latter defined as the ideal density of the MMC with the assumption that all the void volume in the preform is infiltrated with the metal). The results of the 3-sample averaging of densities as well as the scatter bars corresponding to 95% confidence level⁵ of the MMC samples are shown in Figure 28. As we can see, an increase in the temperature of the infiltrating metal as well as an increase in its pressure leads to the increase in the density of the samples. A detailed explanation of this phenomenon is given in the following section.

⁵ The 95% confidence level refers to the fact that the measured value of a sample is likely to fall within a certain band 95 times on the average out of 100.



Figure 27. A typical MMC sample created after the PIP experiment.

Table 8. Some details of the experiments conducted to study the effect of infiltration pressure and temperature on the quality of infiltration and porosity content in the MMC samples created using the gas PIP. The sample numbers are in the form Sij with i and j being the numerical values—note that i and j changes with the infiltration pressure and temperature, respectively.

Sample No.	Infiltration Temperature (°C)	Infiltration Pressure (psi)	Density (g/cm ³)	Relative Density (%)
S11	750	100	1.60	54.63
S12	800	100	2.20	74.84
S13	850	100	2.45	83.59
S14	900	100	2.59	88.25
S21	750	200	1.83	62.24
S22	800	200	2.32	78.93
S23	850	200	2.54	86.54
S24	900	200	2.69	91.65
S31	750	300	2.27	77.23
S32	800	300	2.51	85.63
S33	850	300	2.65	90.18
S34	900	300	2.73	93.13

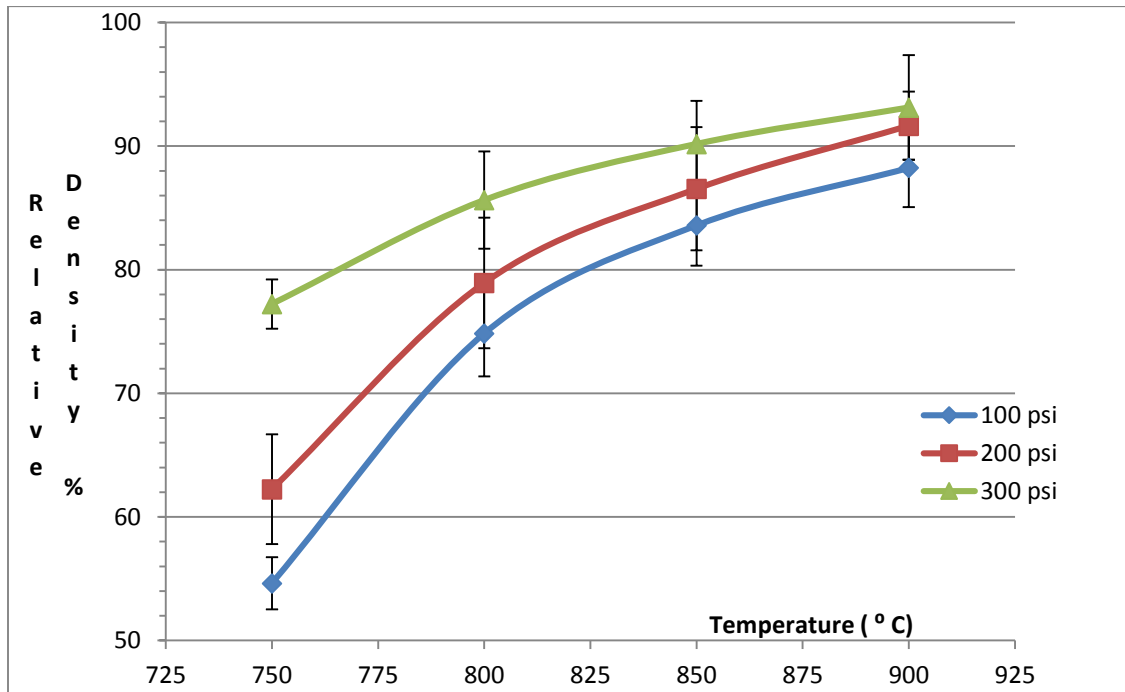


Figure 28. Relative density of the MMC samples made using gas PIP increases with the infiltration temperature and pressure.

The fabricated samples were studied by optical and SEM microscopes. The specimens cut from castings were ground and polished using automatic polishing equipment. The final polishing of MMCs used 0.25 μ m silica colloid to obtain the best possible surface.

The 95% confidence level error bars in Figure 28 indicate that 95 out of 100 times that this experiment is done, the results are expected to fall in the range specified with the corresponding error bar for each case [216]. For the confidence level of $1-\alpha$, the allowable range of a random parameter with student's t-distribution can be found by

$$\xi = \bar{x} \pm t_{\alpha/2} \frac{S}{\sqrt{n}} \quad (6)$$

where ξ shows the upper and lower limits for the allowed numerical value of such parameter, \bar{x} is the mean value of the test samples (here: the average density of the MMC samples), $t_{\alpha/2}$ is the non-dimensional variable defined for any value of α , S is the standard deviation of the test samples and n is the number of samples. In the present study, the number of samples at each time is 3 ($n=3$), and the 95% confidence level will be corresponding to $\alpha/2 = 0.025$. Note that the degree of freedom ν is defined as $\nu = n - 1$ and is equal to 2 in this test. Therefore, the parameter t can be found as a function of α and ν , and is equal to 4.303. Using this method, one can obtain the acceptable range for 95% confidence level when plotting the experimental data. Error bars of 95% confidence level are shown for each experiment at Figure 28.

The value of the density quoted in each row is the average of the density values of the three experiments conducted at that specific temperature and pressure. Then relative densities were calculated based on the percentage of the theoretical density, which is defined as the ideal density of the composite with the assumption that all the void volume in the preform is infiltrated with the metal.

3.1 EFFECT OF PROCESSING CONDITIONS ON THE QUALITY OF INFILTRATION AND POROSITY CONTENT

Increases in the infiltration temperature and pressure are both effective means of achieving full infiltration. Let us discuss the effects of these two processing parameters in greater detail.

Many of the problems in the processing of metal matrix composites, such as poor wetting of the reinforcement by molten metal, are related to the interface between the metal and reinforcement [217]. The interfacial zone that links the reinforcement phase with the matrix phase can be either in the form of a single surface of atomic bonds (simple interface), or one (or even several) new reaction phases and simple interfaces located between the reinforcement and matrix. Most MMCs form non-equilibrium systems during processing—a chemical potential gradient exists at the matrix-reinforcement interface, and this gradient is the driving force for diffusion or chemical reactions at high temperatures during processing [200]. Desirable interfacial properties sometimes force contradictory demands. For example, high chemical affinity between the matrix and reinforcement is desired to ensure spontaneous combination of the two phases, yet low chemical affinity is desired to avoid unwanted chemical reactions at the interface during the processing. In general, wetting of the matrix-reinforcement interface can be classified into two broad categories based on the nature of attractive forces at the interface: 1) physical wetting, and 2) chemical wetting. In polymer-matrix composites, the physical wetting predominates, while in MMCs, both the physical and chemical wettings are important.

Increasing the infiltration temperature improves the quality of infiltration in two ways: Firstly, it improves the wetting between the matrix and the reinforcement (For further details about this phenomena see Appendix D), and thus decreases the contact angle. Secondly, it decreases the viscosity of the molten metal. These two affects facilitates the feeding of the liquid metal to regions undergoing solidification. This explains the gain in density of MMC samples with increasing infiltration temperatures, as observed in Table 8 and Figure 28,

Due to the dual-scale nature of the preform, the infiltrating liquid fills the pore spaces between the tows at a much faster rate than the filling of empty pore spaces within the tows [196] (See Figure 12). As a result, there will be two distinct types of flow-fronts during infiltration: the first flow-front corresponds to the gap (inter-tow) flow and is called the open flow-front; the second type of flow-fronts, which form gas pockets inside the tows, are called the closed flow-fronts. These closed flow fronts are formed behind the open flow fronts and are surrounded by the melt. These macro- and micro-flows have a significant influence on infiltration and solidification during PIP. For example, they lead to the formation of a partially-saturated region, rich in porosity, behind the open flow-fronts. Because of the poor wettability of Alumina by Aluminum, a pressure greater than the thermodynamic gas pressure needs to be applied to the surrounding melt to infiltrate the fiber tows and eliminate the trapped porosity [218].

The compression and disappearance of the gas pockets during infiltration is dependent on the local melt pressure around the gas pockets, which in turn is a function of the applied inlet pressure. Therefore, by increasing the inlet infiltration pressure, we are able to decrease the volume and number of gas pockets, which in turn led to lesser

porosity content in the final product. As shown in Figure 29, the metal content inside the fiber tows increases as the infiltration pressure increases from 100 psi to 300 psi. This increase in the tow saturations with infiltrations is reflected in the increasing sample densities seen in Table 8 and Figure 28.

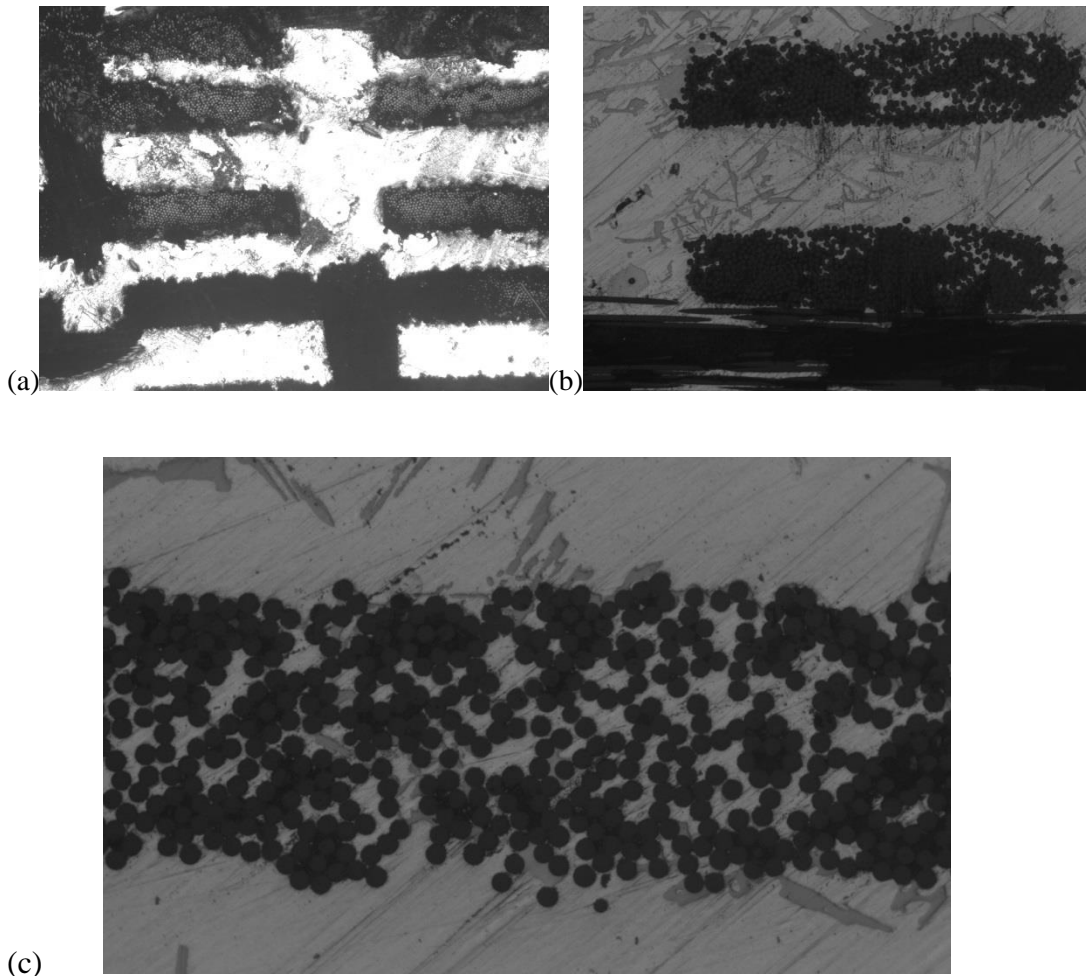


Figure 29 . Optical micrographs of the infiltrated fabric: (a) The 100 psi infiltration pressure case showing large gaps between fiber tows infiltrated with metal while almost no metal can be seen in the pores inside the fiber bundles due to low infiltration pressure. (Magnification 50x) (b) By increasing the infiltration pressure to 200 psi, some metal is observed to have infiltrated inside the fiber tows. (Magnification 100x)(c) More metal infiltration occurred inside the tows as the pressure increases to 300 psi.(Magnification 200x) (Note that the bright areas in these figures correspond to the matrix while the dark areas represent either the fibers or empty voids between them.)

3.2 EFFECT OF MODIFIED CAPILLARY NUMBER ON POROSITY FORMATION IN MMC SAMPLES

Since the balance between viscous and capillary forces present during infiltration significantly affects the process, their relative importance can be assessed by means of the capillary number defined as the ratio of the two forces. Patel et al., in their study of the RTM process for the synthesis of polymer matrix composites, demonstrated that porosity formation in dual-scale fibrous porous media can be correlated to a modified capillary number (Ca^*) [1]. The porosity formation in such media involves two types of micro flows: flow through inter-tow gaps, and the capillary-pressure driven wicking of tows. Competition between these two flows created the lead-lag pattern or fingering in the main flow front. These flows were deemed to be dependent on the balance of viscous and capillary forces, and hence a modified Capillary number, Ca^* , representing the ratio of these forces in the flow field was proposed:

$$Ca^* = \frac{\mu \cdot V}{\sigma_{LV} \cdot \cos \theta} \quad (7)$$

Here μ is the viscosity of the liquid metal, V is some representative metal velocity, σ_{LV} is the surface tension of the liquid metal, and θ is the contact angle. Due to a lack of any means to directly measure metal velocity in the PIP mold cavity, the Darcy velocity at the middle of the mold filling process was chosen as the representative melt velocity. This velocity was estimated by using the 1-D form of Eqn. (3) to determine an analytical expression for the pressure distribution, then using it in Eqn. (1) to estimate Darcy velocity at the center of the mold (see Appendix B for details). The permeability of the dual-scale

preform, which is also required for these calculations, was estimated using the method described in Appendix C. Wang et al. [219] used an oscillating-cup viscometer to measure the absolute viscosities of molten metals at different temperatures and proposed the following empirical Arrhenius-type equation for the viscosity of A356 alloy at different temperatures:

$$\mu = Ae^{B.T^{-1}} \quad (8)$$

Here T is the temperature of the alloy in Kelvin. For A356, A is 0.157 mPa.s , and B is 1850 K [219]. Eqn. (8) was used to estimate viscosities for A356 at different temperatures while calculating Ca^* . The other values needed for the modified capillary number calculations of Eqn. 6 were extracted from references [203, 219, 220]. (See Table 9)

Table 9. Some of the properties of the Aluminum alloy A356 used in our calculations [203].

Material	σ (N/m)	Contact Angle θ	Volumetric Shrinkage (Pct)
A356	0.79	135	5.7

Figure 30 shows the relative densities of the samples increasing with the modified capillary numbers. The high Ca^* in these experiments, indicates that flow leads in the gaps between the axial tows and no macro-porosity is formed between tows. Micro-pores are formed inside the tows due to the axial wicking of the aligned tows from the inter-tow gaps (in-plane roundup type mechanism) and also due to the impregnation of transverse tows occurring after the liquid has flowed around the transverse tows (transverse roundup type mechanism) [1]. Petal et al., in this same study of void formation in LCM processes, found that the voids or air pockets formed inside the tows increased in number as Ca^* increased

beyond 0.01 [1] (See Figure 13). This observation is *contradicted* by the trend seen in Figure 30 where increase in the relative density is due to the increased saturation of tows. Such an unexpected result can be explained as follows. For the present set of experiments, the increase in Ca^* is directly related to the increase in the melt-front velocity through the preform (Eqn. 7), which in turn is directly proportional to the magnitude of the infiltration pressure (Eqn. 15 of Appendix B). Therefore the increase in Ca^* is directly caused by an increase in the infiltration pressure, and hence, the micro bubbles trapped inside the tows shrink or even possibly disappear due to the dissolution of trapped air in the alloy melt. As a result, the trend seen in Figure 28 of increasing relative density with infiltration pressure is replicated in Figure 30 with relative density increasing with Ca^* .

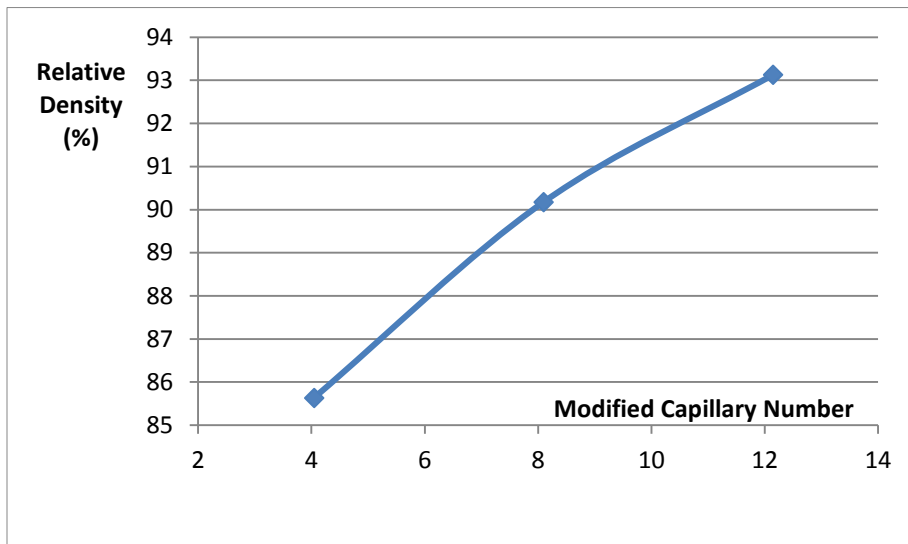


Figure 30. Experimentally observed increase in the relative density with an increase in the modified capillary number, Ca^* .

3.3 EFFECT OF MATRIX SHRINKAGE ON POROSITY IN MMC SAMPLES

As mentioned in the introduction, the shrinkage that occurs on solidification is the primary source of porosity formation in solidifying castings. Solidification shrinkage is a contraction that occurs at the liquid-solid transition as a result of the more open atomic arrangement in liquid metals changing to the denser solid phase. In most cast alloys, the volume shrinkage is typically between 3.2-7.2% [221]. If a region of liquid in the casting becomes isolated from additional feed liquid, then after solidification and shrinkage, the pressure in the liquid drops, causing an increasing pressure difference between the inside and outside of the casting. In this case, there are two possibilities: (i) internal shrinkage porosity may form in the presence of favorable nuclei, (ii) the solidified shell of the casting collapses plastically inwards leading to external porosity or sink. (See Appendix F for further details)

To experimentally investigate the effect of matrix shrinkage on void fraction in MMC samples, a hypereutectic aluminum-silicon alloy called Mercusil, with chemical composition shown in Table 1, was used as the metal matrix. With this composition, the aluminum-silicon alloy system exhibits near zero shrinkage on solidification [214]. Figure 31 shows the plot of the relative density of MMC samples resulting from a series of experiments where the samples infused with Mercusil alloy (at 200 psi infiltration pressure and under infiltration temperatures of 750, 800, 850 and 900 C temperatures) are compared with the samples made from the A356 matrix under similar conditions. As the graph suggests, eliminating the shrinkage porosity results in density gain for MMC samples produced with Mercusil.

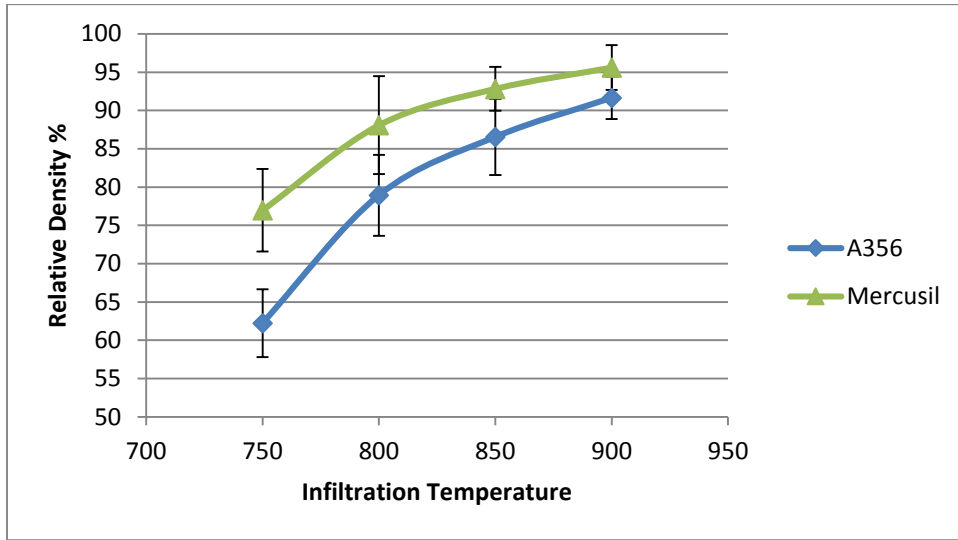


Figure 31. A plot of Relative Densities as a function of infiltration temperature for pressure infiltration of 3D-Nextel fabric with A356 and Mercusil alloy at 200 psi.

CHAPTER 4: SUMMARY AND CONCLUSIONS AND FUTURE WORK

An experimental study of porosity formation in MMCs, which were made using gas PIP with a dual-scale reinforcement, was conducted successfully. The effect of processing parameters of infiltration temperature and pressure on the porosity content of such MMC samples was investigated. The effect of dual-scale nature of the chosen 3D-woven ceramic fabric on metal flow during PIP was studied experimentally through micrographs prepared from samples created by infiltration of these preforms with Al alloy at different temperatures and pressures. A measure of average overall porosity was established through relative density, which can be defined as the ratio of the current MMC density to the hypothetical MMC density created by filling all the pore space with infiltrating metal. It was observed that at lower infiltration temperature and pressures, most of the fiber tows were not infused with metal and this caused high overall porosities in the samples. However, increasing these two parameters led to higher infiltrations and lower porosities in the samples. Increasing the infiltration pressure caused the gas pockets formed inside tows to shrink, while increasing the infiltration temperature caused lower viscosity of the metal and hence more metal wetting and improved feedability.

The porosity formation was also studied in terms of the parameter of modified Capillary number, Ca^* , used in the study of void formation in polymer composites made using RTM. For the estimation of Ca^* , the velocity of open or global front at the center of the preform was used. In the considered method of gas PIP with high Ca^* infiltration, flow leads in the gaps between the axial tows, and as predicted by previous observations, no macro pores were formed. However, as observed in [1], micro pores were indeed

formed inside the tows due to the delayed impregnation of metal into the aligned tows. Since the velocity of open or global front at the center of the preform was used in the estimation of Ca^* , the increase in relative density with Ca^* is caused due to the increase in the infiltration pressure and subsequent shrinkage and disappearance of micropores inside the tow. This decrease in MMC porosity with an increasing Ca^* contradicted the trend of increasing void percentages with Ca^* seen in [1]. However, this study indicates that the parameter of modified Capillary number, Ca^* , can be used to control porosity formation in MMCs produced using gas PIP.

In addition, it was shown experimentally that metal shrinkage plays an important role in porosity formation in this set of MMCs. At identical processing conditions, the use of a zero-shrinkage Al-Si alloy (Mercusil) resulted in higher densities in MMC samples compared with the samples produced using the regular A356 alloy.

Suggested future work includes:

- Actual in-situ measurement of velocities and void formation in PIP molds.
- Further validation of Ca^* experimentally using visual images of voids.
- Extension of Patel's %void vs Ca^* for higher Ca^* seen in PIP.

REFERENCES

1. Patel, N. and L.J. Lee, *Effects of fiber mat architecture on void formation and removal in liquid composite molding*. Polymer Composites, 1995. **16**(5): p. 386-399.
2. Kainer, K.U., *Metal Matrix Composites: Custom-made Materials for Automotive and Aerospace Engineering*, 2006: Wiley.
3. Chawla, K.K. and N. Chawla, *Metal Matrix Composites*, 2006: Springer.
4. Surappa, M.K., *Aluminium matrix composites: Challenges and opportunities*. Sadhana, 2003. **28**(1-2): p. 319-334.
5. Mortensen, A. and J. Llorca, *Metal matrix composites*. Annual review of materials research, 2010. **40**: p. 243-270.
6. Embury, D. and O. Bouaziz, *Steel-Based Composites: Driving Forces and Classifications*. Annual review of materials research, 2010. **40**: p. 213-241.
7. Qin, C.L., et al., *A novel Cu-based BMG composite with high corrosion resistance and excellent mechanical properties*. Acta Materialia, 2006. **54**(14): p. 3713-3719.
8. Inoue, A. and A. Takeuchi, *Recent development and application products of bulk glassy alloys*. Acta Materialia, 2011. **59**(6): p. 2243-2267.
9. Zong, H., et al., *W f/Zr 41.2 Ti 13.8 Cu 12.5 Ni 10 Be 22.5 bulk metallic glass composites prepared by a new melt infiltrating method*. J Alloy Compd, 2010. **504**: p. 106-109.
10. Kong, J., et al., *Effect of flash temperature on tribological properties of bulk metallic glasses*. Tribology letters, 2009. **35**(3): p. 151-158.

11. Wu, Y., et al., *Formation of Cu–Zr–Al bulk metallic glass composites with improved tensile properties*. Acta Materialia, 2011. **59**(8): p. 2928-2936.
12. Liu, Z., et al., *Microstructural tailoring and improvement of mechanical properties in CuZr-based bulk metallic glass composites*. Acta Materialia, 2012. **60**(6): p. 3128-3139.
13. Narayan, R.L., et al., *On the microstructure–tensile property correlations in bulk metallic glass matrix composites with crystalline dendrites*. Acta Materialia, 2012. **60**(13–14): p. 5089-5100.
14. Xu, Y.-K., et al., *Mg-based bulk metallic glass composites with plasticity and gigapascal strength*. Acta Materialia, 2005. **53**(6): p. 1857-1866.
15. Wang, K., et al., *Micromechanisms of serrated flow in a Ni50Pd30P20 bulk metallic glass with a large compression plasticity*. Acta Materialia, 2008. **56**(12): p. 2834-2842.
16. Hu, X., et al., *Glass forming ability and in-situ composite formation in Pd-based bulk metallic glasses*. Acta Materialia, 2003. **51**(2): p. 561-572.
17. Aggour, L., et al., *Thin coatings on carbon fibers as diffusion barriers and wetting agents in Al composites*. Thin Solid Films, 1977. **40**: p. 97-105.
18. Matsunaga, T., et al., *Fabrication of continuous carbon fiber-reinforced aluminum–magnesium alloy composite wires using ultrasonic infiltration method*. Composites Part A: Applied Science and Manufacturing, 2007. **38**(8): p. 1902-1911.
19. Rohatgi, P., N. Ranganathan, and H. Shetty, *The use of metal coated refractory powders to make particulate composites by infiltration*. Composites, 1978. **9**(3): p. 153-156.
20. Sánchez, M., J. Rams, and A. Ureña, *Fabrication of aluminium composites reinforced with carbon fibres by a centrifugal infiltration process*. Composites Part A: Applied Science and Manufacturing, 2010. **41**(11): p. 1605-1611.

21. Seong, H., et al., *Interface structure in carbon and graphite fiber reinforced 2014 aluminum alloy processed with active fiber cooling*. Materials Science and Engineering: A, 2008. **487**(1): p. 201-209.
22. Seong, K., Rohatgi, Lee and Amano, *Solidification Structures in Aluminum Composites by heat extraction through reinforcing carbon fibers*. Affordable Metal Matrix composites for high performance applications II, 2003: p. 135-146.
23. Scudino, S., et al., *Mechanical properties of Al-based metal matrix composites reinforced with Zr-based glassy particles produced by powder metallurgy*. Acta Materialia, 2009. **57**(6): p. 2029-2039.
24. Abbasipour, B., B. Niroumand, and S.M. Monir Vaghefi, *Compocasting of A356-CNT composite*. Transactions of Nonferrous Metals Society of China, 2010. **20**(9): p. 1561-1566.
25. Abbasipour, B., B. Niroumand, and M. Monir-Vaghefi. *Mechanical Properties of A356-CNT Cast Nano Composite Produced by a Special Compocasting Route*. in *TMS Annual Meeting & Exhibition*. 2012. USA.
26. Božić, D., et al., *In-situ Processing of TiB₂ Nanoparticle-Reinforced Copper Matrix Composites*. Science of Sintering, 2009. **41**(2).
27. Božić, D., et al., *Hardening mechanisms in Cu-Ti-TiB₂ composites*. Metalurgija, 2009. **15**(3): p. 159-168.
28. Firoozbakht, M., B. Niroumand, and S.M. Monirvaghefi, *Production of Cast AZ91-CNT Nano-Composite by Addition of Ni-P-CNT Coated Magnesium Powder to the Melt*, in *Supplemental Proceedings 2012*, John Wiley & Sons, Inc. p. 741-748.
29. Habibi, M.K., M. Gupta, and S.P. Joshi, *Size-effects in textural strengthening of hierarchical magnesium nano-composites*. Materials Science and Engineering: A, 2012. **556**(0): p. 855-863.
30. Hosseininezhad, M.M., *Synthesis of cast A356-SiO₂ nano composite using ARB produced metal matrix nanocomposite*. Thesis, M.Sc., 2013, Isfahan university of Technology.

31. Shayan, M. and B. Niroumand, *Synthesis of A356-MWCNT nanocomposites through a novel two stage casting process*. Materials Science & Engineering A, 2013. **582**: p. 262-269.
32. Shehata, F., et al., *Preparation and properties of Al₂O₃ nanoparticle reinforced copper matrix composites by in situ processing*. Materials & Design, 2009. **30**(7): p. 2756-2762.
33. Asthana, R., *Reinforced cast metals: Part II Evolution of the interface*. Journal of Materials Science, 1998. **33**(8): p. 1959-1980.
34. Asthana, R., *Reinforced cast metals: Part I Solidification microstructure*. Journal of Materials Science, 1998. **33**(7): p. 1679-1698.
35. Lloyd, D.J., *Particle reinforced aluminium and magnesium matrix composites*. International Materials Reviews, 1994. **39**(1): p. 1-23.
36. Celebi Efe, G., S. Zeytin, and C. Bindal, *The effect of SiC particle size on the properties of Cu-SiC composites*. Materials & Design, 2012. **36**(0): p. 633-639.
37. Erman, A., et al., *Nanoparticle effects in cast Mg-1 wt% SiC nano-composites*. Materials Science and Engineering: A, 2012. **558**(0): p. 39-43.
38. Abbasipour, B., M. Monir-Vaghefi, and B. Niroumand, *Electroless Ni-P-CNT Composite Coating on Aluminum Powder*. Journal of Metals and Materials International, 2012. **18**: p. 1015-1021.
39. Calin, P., Pehlivanli, *The effect of reinforcement volume ratio on porosity and thermal conductivity in Al-MgO composites*. Materials research, 2012: p. 1057-1063.
40. Firoozbakht, M., M. Monir-Vaghefi, and B. Niroumand, *Electroless Composite Coating of Ni-P-Carbon Nanotubes on Magnesium Powder*. Journal of Alloys and Compounds, 2011. **5095**: p. S496-S502.

41. Samuel, A.M., A. Gotmare, and F.H. Samuel, *Effect of solidification rate and metal feedability on porosity and SiC/Al₂O₃ particle distribution in an Al-Si-Mg (359) alloy*. Composites science and technology 1995. **53**: p. 301-315.
42. Shayan, M., B. Niroumand, and M. Toroghinejad, *Effect of Applied Pressure on Mechanical Properties of Squeeze Cast Al-MWCNT Composites*, in *Materials Science and Technology (MS&T)2012*: USA. p. 128-135.
43. Yang, J., et al., *Fabrication and Characterization of Soluble Multi-Walled Carbon Nanotubes Reinforced P (MMA-co-EMA) Composites*. Macromolecular materials and engineering, 2004. **289**(9): p. 828-832.
44. Bakshi, S.R., D. Lahiri, and A. Agarwal, *Carbon nanotube reinforced metal matrix composites ; a review*. International Materials Reviews, 2010. **55**(1): p. 41-64.
45. Clarke, D.R., *Interpenetrating Phase Composites*. Journal of the American Ceramic Society, 1992. **75**(4): p. 739-758.
46. Seleznev, M.L., et al., *Development of Novel tool-less net-shape pressure infiltration casting technology for manufacturing metal matrix composites*. State of the art in cast metal matrix composites in the next millenium [SiC] : proceedings of a symposium, 2000: p. 81-88.
47. San Marchi, C., et al., *Alumina–aluminum interpenetrating-phase composites with three-dimensional periodic architecture*. Scripta Materialia, 2003. **49**(9): p. 861-866.
48. Young, M.L., et al., *Load partitioning in Al₂O₃–Al composites with three-dimensional periodic architecture*. Acta Materialia, 2009. **57**(8): p. 2362-2375.
49. Young, M.L., et al., *Effect of ceramic preform geometry on load partitioning in Al₂O₃–Al composites with three-dimensional periodic architecture*. Materials Science and Engineering: A, 2009. **526**(1–2): p. 190-196.
50. Dudina, D.V., et al., *Cu-based metallic glass particle additions to significantly improve overall compressive properties of an Al alloy*. Composites Part A: Applied Science and Manufacturing, 2010. **41**(10): p. 1551-1557.

51. Dudina, D.V., et al., *A magnesium alloy matrix composite reinforced with metallic glass*. *Composites Science and Technology*, 2009. **69**(15–16): p. 2734-2736.
52. Lee, M.H., et al., *Fabrication of Ni–Nb–Ta metallic glass reinforced Al-based alloy matrix composites by infiltration casting process*. *Scripta Materialia*, 2004. **50**(11): p. 1367-1371.
53. Scudino, S., et al., *Powder metallurgy of Al-based metal matrix composites reinforced with β -Al₃Mg₂ intermetallic particles: Analysis and modeling of mechanical properties*. *Acta Materialia*, 2009. **57**(15): p. 4529-4538.
54. Yu, P., et al., *Fabrication and mechanical properties of Ni–Nb metallic glass particle-reinforced Al-based metal matrix composite*. *Scripta Materialia*, 2006. **54**(8): p. 1445-1450.
55. Lucci, J.M., et al. *Self-Healing in an Aluminum Alloy Reinforces With Microtubes*. in *ASME 2008 3rd Energy Nanotechnology International Conference*. 2008. Jacksonville, Florida, USA: ASME.
56. Lucci, J.M., et al. *Experiment and Computational Analysis of Self-Healing in an Aluminum Alloy*. in *ASME 2008 International Mechanical Engineering Congress and Exposition*. 2008. Boston, Massachusetts, USA: ASME.
57. Nosonovsky, M., et al., *Physical chemistry of self-organization and self-healing in metals*. *Physical Chemistry Chemical Physics*, 2009. **11**(41): p. 9530-9536.
58. Chawla, N.C., *Metal Matrix Composites*, 2006: Springer.
59. Hutchinson, J.W., et al., *Fundamentals of Metal Matrix Composites*. 1993: p. 158-173.
60. Li, S., et al., *Powder metallurgy Ti–TiC metal matrix composites prepared by in situ reactive processing of Ti-VGCFs system*. *Carbon*, 2013. **61**: p. 216-228.

61. Moreno, M.F. and C.J.R.G. Oliver, *Densification of Al powder and Al–Cu matrix composite (reinforced with 15% Saffil short fibres) during axial cold compaction*. Powder Technology, 2011. **206**: p. 297-305.
62. Samal, C.P., J.S. Parihar, and D. Chaira, *The effect of milling and sintering techniques on mechanical properties of Cu–graphite metal matrix composite prepared by powder metallurgy route*. Journal of Alloys and Compounds, 2013. **569**: p. 95-101.
63. Tjong, S.C. and K.C. Lau, *Properties and abrasive wear of TiB₂/Al-4% Cu composites produced by hot isostatic pressing*. Composites Science and Technology, 1999. **59**(13): p. 2005-2013.
64. Amirkhanlou, S., R. Jamaati, and B. Niroumand, *Fabrication and Characterization of Al/SiCp Composites by CAR Process*. Journal of Materials Science and Engineering, 2011. **A528**: p. 4462-4467.
65. Amirkhanlou, S., et al., *Using ARB Process as a Solution for Dilemma of Si and SiCp Distribution in Cast Al-Si/SiCp Composites*. Journal of Materials Processing Technology, 2011. **211**: p. 1159-1165.
66. Jamaati, R., et al., *Effect of particle size on microstructure and mechanical properties of composites produced by ARB process*. Materials Science and Engineering: A, 2011. **528**(4): p. 2143-2148.
67. Ramu, G. and R. Bauri, *Effect of equal channel angular pressing (ECAP) on microstructure and properties of Al–SiCp composites*. Materials & Design, 2009. **30**(9): p. 3554-3559.
68. Rohatgi, P., et al., *Compressive characteristics of A356/fly ash cenosphere composites synthesized by pressure infiltration technique*. Composites Part A: Applied Science and Manufacturing, 2006. **37**(3): p. 430-437.
69. Asthana, R., P. Rohatgi, and S. Tewari, *Infiltration processing of metal–matrix composites: a review*. Process Adv Compos, 1992. **2**: p. 1-17.
70. Masur, L., et al., *Infiltration of fibrous preforms by a pure metal: Part II. Experiment*. Metallurgical Transactions A, 1989. **20**(11): p. 2549-2557.

71. Amirkhanlou, S. and B. Niroumand, *Development of Al356/SiCp Cast Composites by Injection of SiCp Containing Composite Powders*. Journal of Materials & Design, 2011. **32**: p. 1895-1902.
72. Ghahremanian, M., B. Niroumand, and M. Panjepour, *Production of Al-Si-SiCp cast composites by injection of low-energy ball-milled Al-SiCp powder into the melt*. Metals and Materials International, 2012. **18**(1): p. 149-156.
73. Yang, B., F. Wang, and J. Zhang, *Microstructural characterization of in situ TiC/Al and TiC/Al-20Si-5Fe-3Cu-1Mg composites prepared by spray deposition*. Acta Materialia, 2003. **51**(17): p. 4977-4989.
74. Yandouzi, M., P. Richer, and B. Jodoin, *SiC particulate reinforced Al-12Si alloy composite coatings produced by the pulsed gas dynamic spray process: Microstructure and properties*. Surface and Coatings Technology, 2009. **203**(20): p. 3260-3270.
75. Khor, K.A., et al., *Preparation of Al-Li/SiCp composite powder by a plasma spray atomisation (PSA) technique*. Journal of Materials Processing Technology, 1995. **48**: p. 541-548.
76. Michaud, V.J., *Liquid-state processing (of metal matrix composites)*, in *Fundamentals of metal-matrix composites*, S. Suresh, Editor 1993, Butterworth-Heinemann. p. 3-22.
77. Daniel, B., V. Murthy, and G. Murty, *Metal-ceramic composites via in-situ methods*. Journal of Materials Processing Technology, 1997. **68**(2): p. 132-155.
78. Hwang, S.-Y., J.-W. Lee, and Z.-H. Lee, *Microstructure of a lead-free composite solder produced by an in-situ process*. Journal of electronic materials, 2002. **31**(11): p. 1304-1308.
79. Liu, Y., et al., *Study on Ti fiber reinforced TiAl3 composite by infiltration-in situ reaction*. Journal of Materials Science, 2009. **44**(16): p. 4258-4263.
80. Suresh, M., Needleman, *Fundamentals of metal matrix composites*, 1993: BH.

81. Clyne, W., *An introduction to metal matrix composites*, 1993: Cambridge university press.
82. Noguchi, T. and A. Magario, *Carbon fiber-metal composite material and method of producing the same*, 2008, Google Patents.
83. Cui, C., et al., *Review on fabrication methods of in situ metal matrix composites*. Journal of Materials Science and Technology, 2000. **16**(6): p. 619-626.
84. Orbulov, I.N., Á. Németh, and J. Dobránszky. *Composite production by pressure infiltration*. in *Materials Science Forum*. 2008. Trans Tech Publ.
85. Blucher, J., et al., *Continuous manufacturing of fiber-reinforced metal matrix composite wires—technology and product characteristics*. Composites Part A: Applied Science and Manufacturing, 2001. **32**(12): p. 1759-1766.
86. Liu, J., et al., *Pressureless infiltration of liquid aluminum alloy into SiC preforms to form near-net-shape SiC/Al composites*. Journal of Alloys and Compounds, 2008. **465**(1): p. 239-243.
87. Scherm, F., et al., *Microstructural characterization of interpenetrating light weight metal matrix composites*. Materials Science and Engineering: A, 2009. **518**(1–2): p. 118-123.
88. Zhu, S.J. and T. Iizuka, *Fatigue behavior of Al18B4O33 whisker-framework reinforced Al matrix composites at high temperatures*. Composites Science and Technology, 2003. **63**(2): p. 265-271.
89. Cardinal, S., M. R'Mili, and P. Merle, *Improvement of high pressure infiltration behaviour of alumina platelet preforms: manufacture and characterization of hybrid preforms*. Composites Part A: Applied Science and Manufacturing, 1998. **29**(11): p. 1433-1441.
90. Rohatgi, P.K., V. Tiwari, and N. Gupta, *Squeeze infiltration processing of nickel coated carbon fiber reinforced Al-2014 composite*. Journal of Materials Science, 2006. **41**(21): p. 7232-7239.

91. Long, S., et al., *Processing of Al-based MMCs by indirect squeeze infiltration of ceramic preforms on a shot-control high pressure die casting machine*. Aluminium, 2000. **76**(1-2): p. 82-89.
92. Clyne, T.W., *Metal Matrix Composites*, in *Comprehensive composite materials A*. Kelly and C. Zweben, Editors. 2000, Elsevier. p. 521-554.
93. Cornie, A.J., *Advanced pressure infiltration casting technology produces near-absolute net-shape metal matrix composite components cost competitively*. Materials technology, 1995: p. 43-48.
94. Blucher, T., *Discussion of a liquid metal pressure infiltration process to produce metal matrix composites*. Journal of Materials Processing Technology, 1992: p. 381-390.
95. Isaacs, J., et al., *Chemical stability of zirconia-stabilized alumina fibers during pressure infiltration by aluminum*. Metallurgical Transactions A, 1991. **22**(12): p. 2855-2862.
96. Michaud, V.J., *Infiltration of fiber preforms by a binary alloy*. Thesis, 1991, Massachusetts Institute of Technology, Department of Materials Science and Engineering.
97. Nourbakhsh, S., et al., *Pressure casting of a zirconia-toughened alumina fiber-reinforced NiAl composite*. Metallurgical Transactions A, 1991. **22**(12): p. 3059-3064.
98. Nourbakhsh, S. and H. Margolin, *Processing of continuous-ceramic-fiber-reinforced intermetallic composites by pressure casting*. Materials Science and Engineering: A, 1991. **144**(1): p. 133-141.
99. Premkumar, M.K., W.H. Hunt, and R.R. Sawtell, *Aluminum Composite Materials for Multichip Modules*. JOM, 1992: p. 24-28.
100. Cochran, C.N. and R.C. Ray, 1970,

101. Yang, J. and D. Chung, *Casting particulate and fibrous metal-matrix composites by vacuum infiltration of a liquid metal under an inert gas pressure*. Journal of Materials Science, 1989. **24**(10): p. 3605-3612.
102. Wang, B. and K.M. Pillai, *Numerical simulation of pressure infiltration process for making metal matrix composites using dual-scale fabrics*. Metallurgical and Materials Transactions A, 2013. **44**(13): p. 5834-5852.
103. Blucher, J., J. Dobranszky, and U. Narusawa, *Aluminium double composite structures reinforced with composite wires*. Materials Science and Engineering: A, 2004. **387**: p. 867-872.
104. Chadwick, G.A., *Squeeze casting of metal matrix composites using short fibre preforms*. Materials Science and Engineering: A, 1991. **135**: p. 23-28.
105. Zantout, B., A. Das, and J. Franklin. *Squeeze-Cast Aluminum-Matrix Composite: Strength at Higher Temperature*. in *The Metallurgy of Light Alloys Spring Residential Conf, The Institute of Metallurgists (March 1983) No.* 1983.
106. Yue, T., Y. Dai, and W. Lau, *An examination of wire electrical discharge machining (WEDM) of Al₂O₃ particulate reinforced aluminum based composites*. MATERIAL AND MANUFACTURING PROCESS, 1996. **11**(3): p. 341-350.
107. Schultz, B.F., J.B. Ferguson, and P.K. Rohatgi, *Microstructure and hardness of Al₂O₃ nanoparticle reinforced Al-Mg composites fabricated by reactive wetting and stir mixing*. Materials Science and Engineering: A, 2011. **530**: p. 87-97.
108. Fukunaga, H., *Processing aspects of squeeze casting for short fiber reinforced metal matrix composites*. MATERIAL AND MANUFACTURING PROCESS, 1988. **3**(4): p. 669-687.
109. Fukunaga, H., *Squeeze casting processes for fiber reinforced metals and their mechanical properties*. Ref, 1988. **34**: p. 101-107.
110. Jarry, P., et al., *Infiltration of fiber preforms by an alloy: Part III. Die casting experiments*. Metallurgical Transactions A, 1992. **23**(8): p. 2281-2289.

111. Rasmussen, N., P. Hansen, and S. Hansen, *High pressure die casting of fibre-reinforced aluminium by preform infiltration*. Materials Science and Engineering: A, 1991. **135**: p. 41-43.
112. Imai, T., et al., *K₂O-6TiO₂ whisker-reinforced aluminium composite by a powder metallurgical method*. Journal of Materials Science Letters, 1987. **6**(11): p. 1257-1258.
113. Chadwick, G.A. and T.M. Yue, *Principles and applications of squeeze casting*. Metals and materials, 1989. **5**(1): p. 6-12.
114. Aguilar-Martinez, J.A., et al., *Effect of processing parameters on the degree of infiltration of SiCp preforms by Al-Si-Mg alloys*. Materials Letters, 2003. **57**(26): p. 4332-4335.
115. Lapin, J., D. Tiberghien, and F. Delannay, *On the parameters affecting the formation of iron aluminides during pressure-assisted infiltration of aluminium into a preform of steel fibres*. Intermetallics, 2000. **8**(12): p. 1429-1438.
116. Beffort, O., et al., *Alloying effects on microstructure and mechanical properties of high volume fraction SiC-particle reinforced Al-MMCs made by squeeze casting infiltration*. Composites Science and Technology, 2007. **67**(3): p. 737-745.
117. Long, S., Z. Zhang, and H.M. Flower, *Characterization of liquid metal infiltration of a chopped fibre preform aided by external pressure—I. Visualization of the flow behaviour of aluminium melt in a fibre preform*. Acta Metallurgica et Materialia, 1995. **43**(9): p. 3489-3498.
118. Long, S., Z. Zhang, and H.M. Flower, *Characterization of liquid metal infiltration of a chopped fibre preform aided by external pressure—II. Modelling of liquid metal infiltration process*. Acta Metallurgica et Materialia, 1995. **43**(9): p. 3499-3509.
119. Long, S., Z. Zhang, and H.M. Flower, *Hydrodynamic analysis of liquid infiltration of unidirectional fibre arrays by squeeze casting*. Acta Metallurgica et Materialia, 1994. **42**(4): p. 1389-1397.

120. Long, S., et al., *Effect of Squeeze Infiltration Speed on Infiltration Quality and Tensile Properties of Cast Saffil/AlCu4MgAg Composite*. Proceedings: Metal matrix composites and physical properties, 1997. **3**: p. 274.
121. Charbonnier, J., *Machine for pressure casting of metal parts possibly containing fibres of ceramic materials*, 1988, Google Patents.
122. Girot, P., et al., *Composite affinity sorbents and their cleaning in place*. Journal of Chromatography A, 1990. **510**: p. 213-223.
123. Bhagat, R.B., *High pressure infiltration casting: manufacturing net shape composites with a unique interface*. Materials Science and Engineering: A, 1991. **144**(1): p. 243-251.
124. Kelly, A. and C. Zweben, *Comprehensive Composite Materials*. Vol. 3. 2000: Elsevier
125. Benjamin, W.P. and S.W. Beckwith, eds. *Resin Transfer Molding, SAMPE Monograph No.3*. 1999, SAMPE: USA.
126. Suresh, S., A. Mortensen, and A. Needleman, *Fundamentals of metal-matrix composites*, 1993: Butterworth-Heinemann.
127. Gutowski, T.G., ed. *Advanced composites manufacturing*. 1997, John Wiley & Sons: New York.
128. Tan, H. and K.M. Pillai, *Multi-scale modeling of unsaturated flow in dual-scale fiber preforms of liquid composite molding I: Isothermal flows*. Composites: Part A, 2012. **43**: p. 1-13.
129. Pillai, K.M., *Modeling the unsaturated flow in liquid composite molding processes: A review and some thoughts*. Journal of Composite Materials, 2004. **28**(23): p. 2097-2118.
130. Parnas, R.S. and J.F.R. Phelan, *The Effect of heterogeneous Porous Media on Mold Filling in Resin Transfer Molding* SAMPE Quarterly, 1990. **22**(2): p. 53-60.

131. Chan and Morgan, *Tow impregnation during resin transfer molding of bi-directional nonwoven fabrics*. Polymer Composites, 1993: p. 335-340.
132. Binetruy, C., B. Hilaire, and J. Pabiot, *Tow impregnation model and void formation mechanisms during RTM*. . Journal of Composite Materials, 1998. **32**(3): p. 223-245.
133. Parseval, Y.D., K.M. Pillai, and S.G. Advani, *A simple model for the variation of permeability due to partial saturation in dual scale porous media*. Transport in Porous Media, 1997. **27**: p. 243.
134. Breard, J. and e. al, *Analysis of dynamic flows through porous media. Part I: comparison between saturated and unsaturated flows in fibrous reinforcements*. . Polymer Composites, 2003. **24**(3): p. 391-408.
135. Babu, B.Z. and K.M. Pillai, *Experimental investigation of the effect of fiber-mat architecture on the unsaturated flow in liquid composite molding*. journal of Composite Materials, 2004. **38**(1): p. 57-79.
136. Tan, H., T. Roy, and K.M. Pillai, *Variations in unsaturated flow with flow direction in resin transfer molding: an experimental investigation*. Composites: Part A, 2007. **38**(8): p. 1872-92.
137. Lekakou, C. and M.G. Bader, *Mathematical modelling of macro- and micro-infiltration in resin transfer moulding (RTM)*. Composites: Part A, 1998. **29**(1-2): p. 29-37.
138. Dessenberger, R.B. and C.L. Tucker, *Thermal dispersion in resin transfer molding*. Polymer Composites, 1995. **16**(6): p. 495-506.
139. Chan, A.W. and R.J. Morgan, *Tow impregnation during resin transfer molding of bidirectional nonwoven fabrics*. Polymer Composites, 1993. **14**(4): p. 335-340.
140. Pillai, K.M. and S.G. Advani, *A model for unsaturated flow in woven fiber preforms during mold filling in resin transfer molding*. Journal of Composite Material, 1998. **32**(19): p. 1753-83.

141. Pillai, K.M., *Modeling the unsaturated flow in liquid composite molding processes: A review and some thoughts*. Composite materials, 2004: p. 2097-2118.
142. Patel, N., V. Rohatgi, and L.J. Lee, *Micro Scale Flow Behavior and Void Formation Mechanism During Impregnation Through a Unidirectional Stitched Fiberglass Mat*. Polymer Engineering and Science, 1995. **35**(10): p. 837-851.
143. Lundstorm, T.S., *Void formation and transport in RTM*, 1993, Swedish institute of composites.
144. Peterson, R.C. and R.E. Robertson. *Mechanism affecting void distribution and elimination in Resin Transfer Molding*. in *Proceedings of the 8th advanced composites conference*. 1992. Chicago, Illinois, USA: .
145. Chen, Y.T., H.T. Davis, and C.W. Macosko, *Wetting of fiber mats for composite Manufacturing: I Visualization Experiments*. AIChE Journal, 1995. **41**(10): p. 2261-2273.
146. Lundström, T.S. and B.R. Gebart, *Influence from process parameters on void formation in resin transfer molding*. Polymer Composites, 1994. **15**(1): p. 25-33.
147. Chen, Y.T., C. Macosko, and Davis, *wetting of fiber mats for composite manufacturing: II Air entrapment model*. AIChE Journal, 1995: p. 2274-2281.
148. Rohatgi, V., N. Patel, and L.J. Lee, *Experimental Investigation of Flow-Induced Microvoids During Impregnation of Unidirectional Stitched Fiberglass Mat*. Polymer Composites, 1996. **17**(2): p. 161-170.
149. Fong, L. and S.G. Advani, *The role of Dual permeability in mold filling simulation of resin transfer molding*, in *proceedings of international conference on composite engineering ICCE1994*. p. 301.
150. Chang, C.Y. and L.W. Hourng, *Numerical Simulation for the transverse impregnation in resin transfer molding*. Journal of reinforced plastics and composites, 1998. **17**(2): p. 165-182.

151. Lin, M., H.T. Hahn, and H. Huh, *A finite element simulation of resin transfer molding based on partial nodal saturation and implicit time integration Composites part A*, 1998. **29**(5-6): p. 541-550.
152. Mohan, R.V., N.D. Ngo, and K.K. Tamma, *On a pure finite-element-based methodology for resin transfer mold filling simulations*. *Polymer Engineering Science* 1999. **39**(1): p. 26-43.
153. Patel, N. and L.J. Lee, *Modeling of void formation and removal in liquid composite molding. Part I: Wettability analysis*. *Polymer Composites*, 1996. **17**(1): p. 96-103.
154. Patel, N. and L.J. Lee, *Modeling of void formation and removal in liquid composite molding. Part II: Model development and implementation*. *Polymer Composites*, 1996. **17**(1): p. 104-114.
155. Pillai and Advani, *Modeling of void migration in Resin Transfer Molding Process*, in *Proceedings of the 1996 ASME International Mechanical Engineering Congress and Exhibition* 1996.
156. Chui, W.K., et al., *Process Modeling in Resin Transfer Molding as a method to enhance product quality*. *SIAM REV.*, 1997. **39**(4): p. 714-727.
157. Llorca, J., *3.04 - Void Formation in Metal Matrix Composites*, in *Comprehensive Composite Materials*, A. Kelly and C. Zweben, Editors. 2000, Pergamon: Oxford. p. 91-115.
158. Chen, X.G. and S. Engler, *Formation of gas porosity in aluminum alloys*. *American Foundry Society Transactions*, 1993. **92-94**: p. 673-682.
159. Mortensen, A., *Melt infiltration of metal matrix composites*. *Comprehensive composite*, 2000. **3**: p. 521-554.
160. Mortensen, A., et al., *Infiltration of fibrous preforms by a pure metal: Part I. Theory*. *Metallurgical Transactions A*, 1989. **20**(11): p. 2535-2547.
161. Mortensen, A., V.J. Michaud, and M.C. Flemings, *Pressure-infiltration processing of reinforced aluminum*. *JOM*, 1993. **45**(1): p. 36-43.

162. Mortensen, A., *Interfacial phenomena in the solidification processing of metal matrix composites*. Materials Science and Engineering: A, 1991. **135**: p. 1-11.
163. Dopler, T., A. Modaressi, and V. Michaud, *Simulation of metal matrix composite infiltration processing*. Processing and Fabrication of Advanced Materials VII, TMS, 1998: p. 381-392.
164. Dopler, T., A. Modaressi, and V. Michaud, *Simulation of metal-matrix composite isothermal infiltration processing*. Metallurgical and materials Transactions B, 2000. **31**(2): p. 225-234.
165. Mal, O., A. Couniot, and F. Dupret, *Non-isothermal simulation of the resin transfer moulding press*. Composites Part A: Applied Science and Manufacturing, 1998. **29**(1): p. 189-198.
166. Kang, M.K. and W.I. Lee, *A flow-front refinement technique for the numerical simulation of the resin-transfer molding process*. Composites Science and Technology, 1999. **59**(11): p. 1663-1674.
167. Bruschke, M. and S. Advani, *A numerical approach to model non-isothermal viscous flow through fibrous media with free surfaces*. International Journal for numerical methods in fluids, 1994. **19**(7): p. 575-603.
168. Joshi, S., Y. Lam, and X.-L. Liu, *Mass conservation in numerical simulation of resin flow*. Composites Part A: Applied Science and Manufacturing, 2000. **31**(10): p. 1061-1068.
169. Lam, Y., S.C. Joshi, and X. Liu, *Numerical simulation of the mould-filling process in resin-transfer moulding*. Composites Science and Technology, 2000. **60**(6): p. 845-855.
170. Kuan, Y.d. and A.S. El-Gizawy, *Numerical characterization of mold injection in resin transfer molding process*. Advances in Polymer Technology, 2000. **19**(3): p. 173-179.

171. Voller, V. and S. Sundarraj, *A model of inverse segregation: the role of microporosity*. International journal of heat and mass transfer, 1995. **38**(6): p. 1009-1018.
172. Shojaei, A., S. Ghaffarian, and S. Karimian, *Numerical simulation of three-dimensional mold filling process in resin transfer molding using quasi-steady state and partial saturation formulations*. Composites Science and Technology, 2002. **62**(6): p. 861-879.
173. Lin, H., et al., *Macroporosity and initial moisture effects on infiltration rates in vertisols and vertic intergrades*. Soil Science, 1998. **163**(1): p. 2-8.
174. Sommer, J.L. and A. Mortensen, *Forced unidirectional infiltration of deformable porous media*. Journal of Fluid Mechanics, 1996. **311**: p. 193-217.
175. Preziosi, L., *The theory of deformable porous media and its application to composite materials manufacturing*. Surveys on Mathematics for Industry, 1996. **6**: p. 167-214.
176. Ambrosi, D. and L. Preziosi, *Modeling injection molding processes with deformable porous preforms*. SIAM Journal on Applied Mathematics, 2000. **61**(1): p. 22-42.
177. Ambrosi, D. and L. Preziosi, *Modelling matrix injection through elastic porous preforms*. Composites Part A: Applied Science and Manufacturing, 1998. **29**(1): p. 5-18.
178. Danis, M., et al. *Infiltration of fibrous preform by a liquid metal: Modelization of the preform deformation*. in *Proceeding of the ICCM*. 1999.
179. Michaud, V., A. Mortensen, and J. Sommer, *Infiltration of fibrous preforms by a pure metal: Part V. Influence of preform compressibility*. Metallurgical and Materials Transactions A, 1999. **30**(2): p. 471-482.
180. Antonelli, D. and A. Farina, *Resin transfer moulding: mathematical modelling and numerical simulations*. Composites Part A: Applied Science and Manufacturing, 1999. **30**(12): p. 1367-1385.

181. Gutowski, T.G., T. Morigaki, and Z. Cai, *The consolidation of laminate composites*. Journal of Composite Materials, 1987. **21**(2): p. 172-188.
182. Chen, B., A.-D. Cheng, and T.-W. Chou, *A nonlinear compaction model for fibrous preforms*. Composites Part A: Applied Science and Manufacturing, 2001. **32**(5): p. 701-707.
183. Jespersen, S., et al., *Film stacking impregnation model for a novel net shape thermoplastic composite preforming process*. Composites Science and Technology, 2008. **68**(7): p. 1822-1830.
184. Lacoste, E., et al., *Numerical simulation of the infiltration of fibrous preforms by a pure metal*. Metallurgical Transactions A, 1993. **24**(12): p. 2667-2678.
185. Lacoste, E., et al., *Numerical simulation of the injection moulding of thin parts by liquid metal infiltration of fibrous preforms*. Materials Science and Engineering: A, 1991. **135**: p. 45-49.
186. Voller, V. and C. Swaminathan, *ERAL Source-based method for solidification phase change*. Numerical Heat Transfer, Part B Fundamentals, 1991. **19**(2): p. 175-189.
187. Mantaux, O., E. Lacoste, and M. Danis, *Heat-conduction with phase-change in a pure substance-resolution formulated with temperature terms*. Revue Generale de Thermique, 1995. **34**(402): p. 339-347.
188. Tong, X., J.A. Khan, and M. RuhulAmin, *Enhancement of heat transfer by inserting a metal matrix into a phase change material*. Numerical Heat Transfer, Part A Applications, 1996. **30**(2): p. 125-141.
189. Biswas, D.K., J.E. Gatica, and S.N. Tewari, *Dynamic analysis of unidirectional pressure infiltration of porous preforms by pure metals*. Metallurgical and Materials Transactions A, 1998. **29**(1): p. 377-385.
190. Lacoste, E., O. Mantaux, and M. Danis, *Numerical simulation of metal matrix composites and polymer matrix composites processing by infiltration: a review*. Composites Part A: Applied Science and Manufacturing, 2002. **33**(12): p. 1605-1614.

191. Chang, C.Y., *Numerical simulation of the pressure infiltration of fibrous preforms during MMC processing*. *Advanced Composite Material*, 2006. **15**(3): p. 287-300.
192. Jung, C., J. Jang, and K. Han, *Numerical simulation of infiltration and solidification processes for squeeze cast Al composites with parametric study*. *Metallurgical and Materials Transactions A*, 2008. **39**(11): p. 2736-2748.
193. Mortensen, A. and V. Michaud, *Infiltration of fiber preforms by a binary alloy: Part I. Theory*. *Metallurgical Transactions A*, 1990. **21**(7): p. 2059-2072.
194. Khan, J.A. and X. Tong, *Unidirectional infiltration and solidification/remelting of Al-Cu alloy*. *Journal of thermophysics and heat transfer*, 1998. **12**(1): p. 100-106.
195. Lee, E., R.S. Amano, and P.K. Rohatgi, *Metal matrix composite solidification in the presence of cooled fibers: numerical simulation and experimental observation*. *Heat and mass transfer*, 2007. **43**(8): p. 741-748.
196. Wang, B. and K.M. Pillai, *Numerical simulation of pressure infiltration process for making metal matrix composites using dual-scale fabrics*. *Metallurgical and materials transactions A*, 2013: p. 5834-5852.
197. Samuel, A.M., H. Liu, and F.H. Samuel, *Effect of melt, solidification and heat-treatment processing parameters on the properties of Al-Si-Mg/SiC(p) composites*. *Journal of Materials Science*, 1993. **28**(24): p. 6785-6798.
198. Aqida, S.N., M.I. Ghazali, and J. Hashim, *Effects of porosity on mechanical properties of metal matrix composites: An overview*. *Jurnal Teknologi*, 2004. **40**(A): p. 17-32.
199. Mortensen, A., et al., *Alloy Microstructures in Cast Metal Matrix Composites*. *JOM*, 1986. **38**(3): p. 30-35.
200. Chou, T.W., A. Kelly, and A. Okura, *Fibre-reinforced metal-matrix composites*. *Composites*, 1985. **16**(3): p. 187-206.
201. Flemings, M.C., *Solidification processing*, 1974: McGraw-Hill.

202. Ray, S., *Synthesis of cast metal matrix particulate composites*. Journal of Materials Science, 1993. **28**(20): p. 5397-5413.
203. Emadi, D., J.E. Gruzleski, and J.M. Toguri, *The effect of na and Sr modification on surface tension and volumetric shrinkage of A356 alloy and their influence on porosity formation*. Metallurgical Transactions B, 1993. **24**(6): p. 1055-1063.
204. Emamy Ghomy, M. and J. Campbell, *Solidification shrinkage in metal matrix composites*. Cast Metals, 1995. **8**(2): p. 115-122.
205. Ilegbusi, O. and J. Yang, *Porosity nucleation in metal-matrix composites*. Metallurgical and Materials Transactions A, 2000. **31**(8): p. 2069-2074.
206. Mortensen, A. and J.A. Cornie, *On the infiltration of metal matrix composites*. Metallurgical and Materials Transactions A, 1987. **18**(13): p. 1160-1163.
207. Asthana, R., *Solidification Processing of Reinforced Metals*. Transtech Publishers Switzerland, 1997: p. 46.
208. Ilegbusi, O. and J. Yang, *Effect of matrix and interface properties on porosity nucleation in metal-matrix composites*. Journal of materials processing and manufacturing science, 1999. **8**(2): p. 106-112.
209. Calin, R., M. Pul, and Z.O. Pehlivanli, *The Effect of Reinforcement Volume Ratio on Porosity and thermal conductivity in Al-Mgo composites*. Journal of Materials Research, 2012. **15**(6): p. 1057-1063.
210. Liu, T.M. and C.G. Chao, *Effect of magnesium on mechanical properties of alumina-fiber-reinforced aluminum matrix composites formed by pressure infiltration casting*. Materials science and engineering, 1993. **169**: p. 79-84.
211. Kang, B.S., et al., *Preparation of nickel-coated alumina composite powder by an aqueous-phase reduction process*. Journal of Materials Science, 1995. **30**(15): p. 3883-3887.

212. Rajan, T.P.D., R.M. Pillai, and B.C. Pai, *Review Reinforcement coatings and interfaces in aluminum metal matrix composites*. Journal of materials science 1998. **35**: p. 3491-3503.
213. Garcia-Cordovillaa, C., E. Louis, and J. Narcisoc, *Pressure infiltration of packed ceramic particulates by liquid metals*. Acta Materialia, 1999 **47**(18): p. 4461–4479.
214. Donahue and e. al., Hypereutectic Aluminum Silicon alloy, 1990, U. patent, 4969428
215. Mohamed, M.H., et al., *A new generation of 3D woven fabric preforms in composites*. SAMPE Journal, 2001. **37**(3): p. 8-17.
216. Wheeler, A.J. and A.R. Ganji, *Introduction to Engineering Experimentation*, 2010: Prentice Hall PTR.
217. Suresh, Mortensen, and Needleman, *Fundamentals of metal matrix composites*, 1993: BH.
218. Asthana, R., P.K. Rohatgi, and S.N. Tewari, *Infiltration processing of metal-matrix composites: a review*. Processing of advanced materials, 1992: p. 1-17.
219. Overfelt, D. and Wang, *Oscillating Cup Viscosity Measurement of Aluminum Alloys: A201, A319 and A356*. International Journal of Thermophysics, 2002: p. 1063-1076.
220. Schoutens, J.E., *Some theoretical considerations of the surface tension of liquid metals for metal matrix composites*. Journal of Materials Science, 1989. **24**(8): p. 2681-2686.
221. Campbell, J., *Complete Casting Handbook - Metal Casting Processes, Metallurgy, Techniques and Design*, 2011: Elsevier.
222. Papathanasiou, T.D., *Flow across structured fiber bundles: a dimensionless correlation*. International journal of multiphase Flow 27, 2001. **27**(8): p. 1451-1461.

223. Oh, S.Y., J.A. Cornie, and K.C. Russell, *Wetting of ceramic particulates with liquid aluminum alloys: Part I. Experimental techniques* Metallurgical Transactions A, 1989. **20**(3): p. 527-532.
224. Mortensen, A. and I. Jin, *Solidification processing of metal matrix composites*. International Materials Reviews, 1992. **37**(1): p. 101-128.
225. Rajan, T., et al., *Solidification and casting/mould interfacial heat transfer characteristics of aluminum matrix composites*. Composites Science and Technology, 2007. **67**(1): p. 70-78.
226. Ouyang, et al., *Wettability at Al-Mg/Ceramic Interfaces*. Key Engineering Materials, 2006: p. 159-164.
227. Asavavisithchai, S. and A.R. Kennedy, *The effect of Mg addition on the stability of Al-Al₂O₃ foams made by a powder metallurgy route*. Scripta Materialia, 2006: p. 1331-1334.
228. Munitz, Metzger, and Mehrabian, *The interface phase in Al-Mg/Al₂O₃ composites*. American Society for Metals and Metallurgical Society of AIME, 1979: p. 1491-1497.
229. Fisher, J.C., *The fracture of liquids*. Journal of Applied Physics, 1948. **19**: p. 1062–1067.
230. Piwonka, T.S. and M.C. Fleming, *Pore formation in solidification*. Transactions of the Metallurgical Society of AIME, 1966. **236**: p. 1157-1165.

APPENDICES

APPENDIX A: RAW DATA FOR THE EXPERIMENTS

Table 10. Raw data for the first set of experiments to study the effect of processing parameters on the porosity content of MMC samples.

Sij	P(psi)	T(°C)	ρ (kg/m ³)	Relative Density	Average ρ (kg/m ³)	Average RD	Standard Deviation	Error Bar
S11	100	750	1.57	53.49	1.60	54.63	0.85	2.11
			1.63	55.54				
			1.61	54.9				
S12	100	800	2.15	73.25	2.20	74.84	1.40	3.48
			2.25	76.66				
			2.19	74.6				
S13	100	850	2.40	81.77	2.45	83.59	1.31	3.26
			2.47	84.16				
			2.49	84.8				
S14	100	900	2.54	86.54	2.59	88.25	1.27	3.16
			2.63	89.61				
			2.60	88.6				
S21	200	750	1.8	61.33	1.83	62.24	1.78	4.44
			1.78	60.65				
			1.9	64.7				
S22	200	800	2.25	76.66	2.32	78.93	2.12	5.27
			2.4	81.77				
			2.3	78.4				
S23	200	850	2.52	85.86	2.54	86.54	2.00	4.98
			2.62	89.27				
			2.48	84.5				
S24	200	900	2.65	90.29	2.69	91.65	1.11	2.76
			2.69	91.65				
			2.73	93				
S31	300	750	2.3	78.36	2.27	77.23	0.80	1.99
			2.25	76.66				
			2.25	76.66				
S32	300	800	2.45	83.48	2.51	85.63	1.58	3.92
			2.53	86.2				
			2.56	87.2				
S33	300	850	2.6	88.59	2.65	90.18	1.40	3.47
			2.7	91.99				
			2.64	89.9				
S34	300	900	2.72	92.67	2.73	93.13	1.69	4.22
			2.68	91.31				
			2.80	95.4				

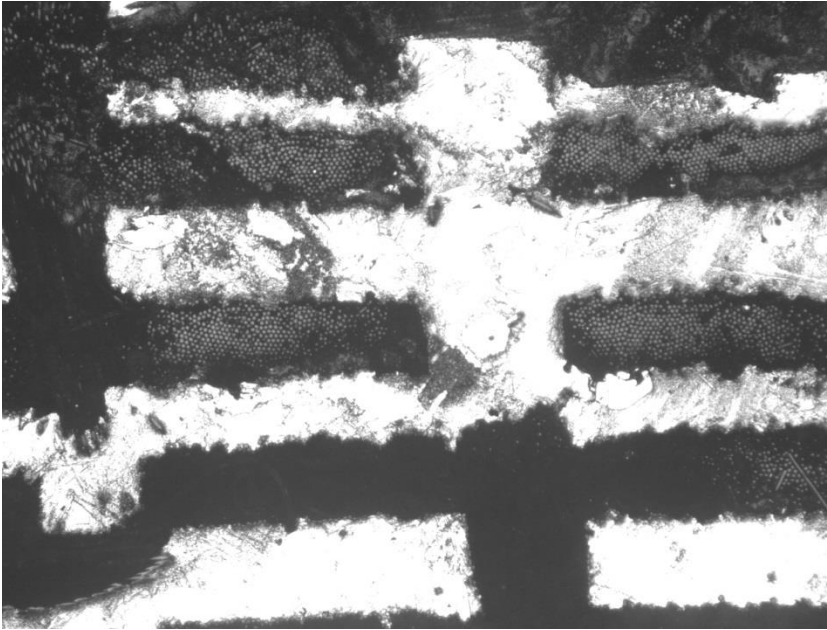


Figure 32. Micrograph of a S11 sample (Magnification 50X)

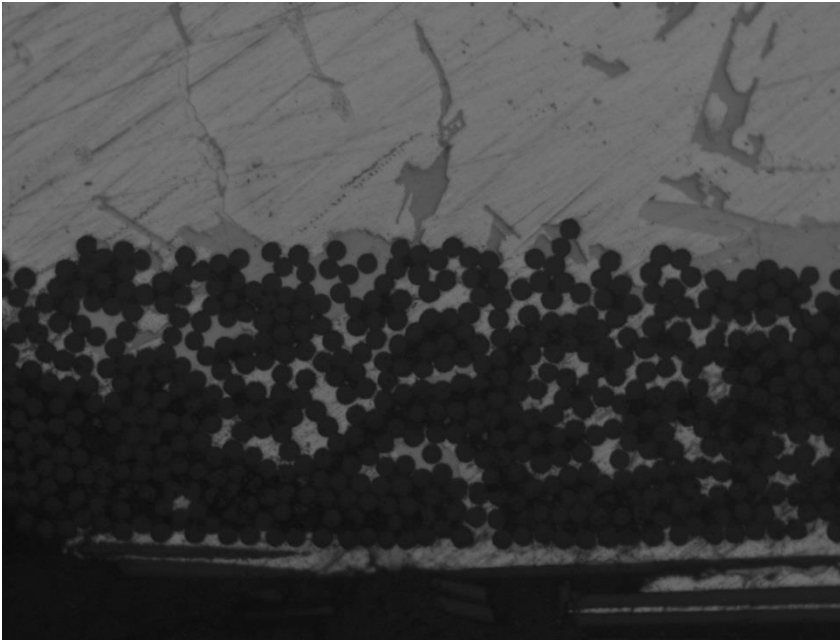


Figure 33. Micrograph of a fiber tow of a S23 sample (Magnification 200X)

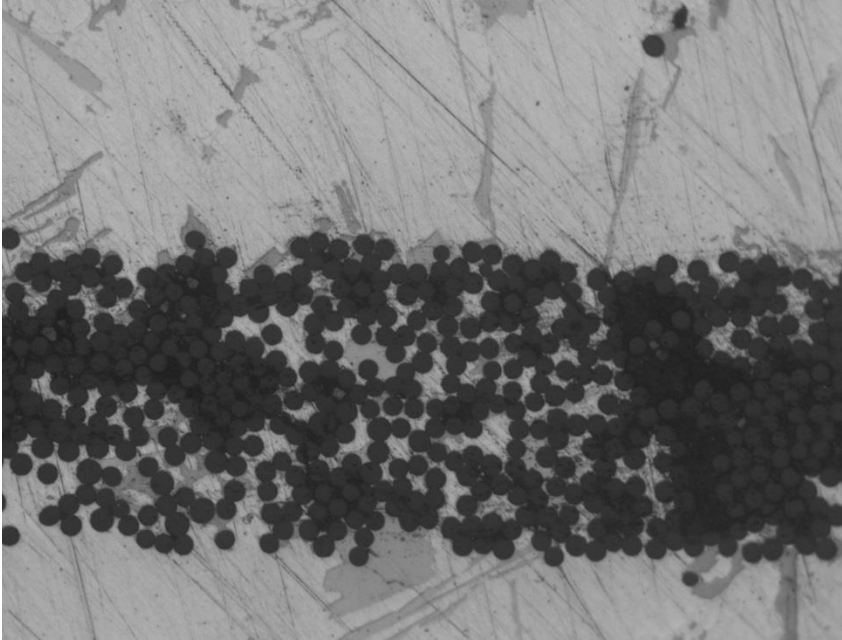


Figure 34. Micrograph of a S32 sample. (Magnification 200X)

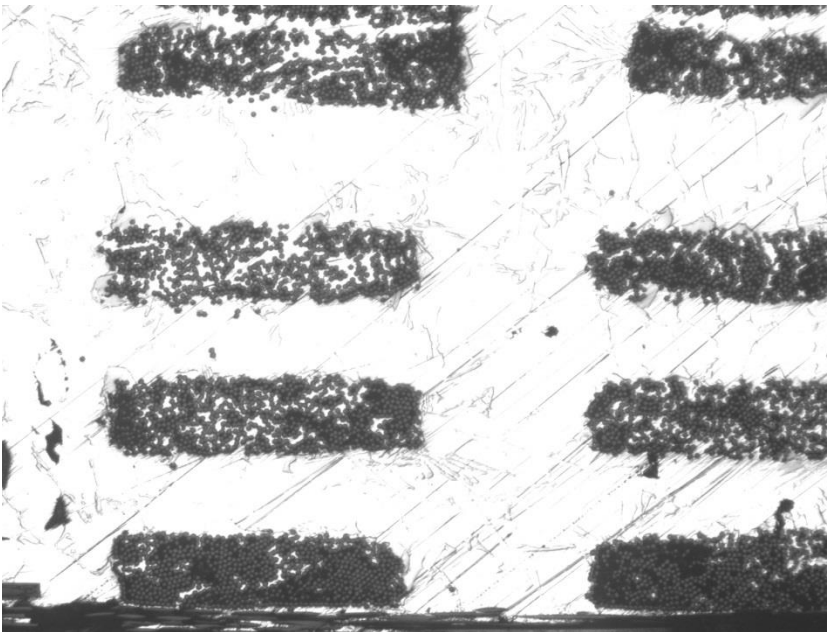


Figure 35. Micrograph of a S33 sample. (Magnification 50X)

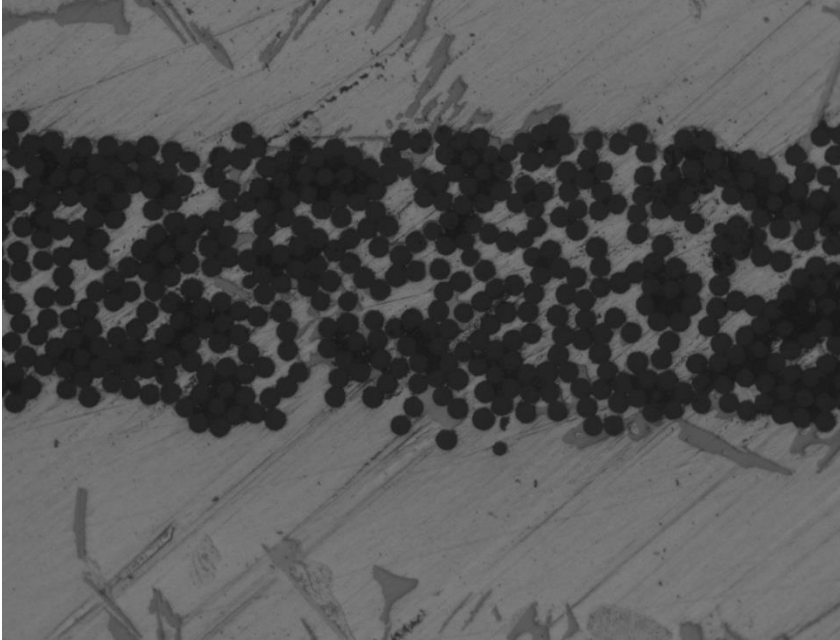


Figure 36. Micrograph of a fiber tow of S34 sample. (Magnification 200X)

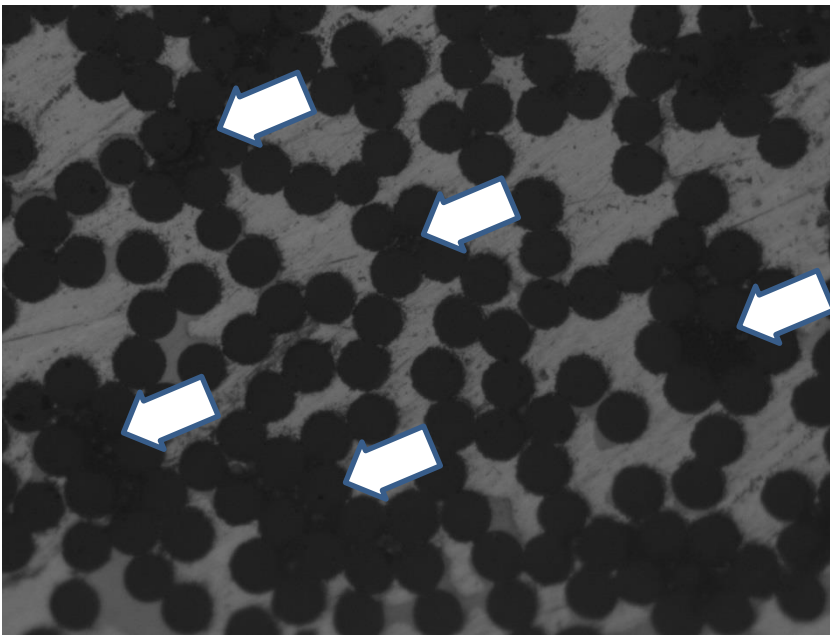


Figure 37. Micrograph of S34 sample with higher magnification. Porosity can be seen at the contact areas of the fibers. (Magnification 500X)

The composite theoretical density can be calculated using the rule of mixtures. From the rule-of-mixture formula, the theoretical value for the composite density can be calculated as

$$\rho_C = \rho_M V_M + \rho_f V_f \quad (9)$$

where ρ_M is the density of the matrix (A356 Al alloy) which is equal to 2.685 g/cm³; V_M is the volume fraction of the matrix, which is equal to 0.65; ρ_f is the density of the fiber with a value of 3.40 g/cm³; and V_f is the volume fraction of the fiber, which is equal to 0.35. Therefore, the composite theoretical value calculated from Eqn. (9) is

$\rho_C = 2.935$ g/cm³. The relative density (RD) as a percentage, is defined as $\frac{\rho}{\rho_C} \times 100$.

Table 11. Raw data for the second set of experiments to study the effect of matrix shrinkage on the porosity content of MMC samples. The applied infiltration pressure for all these experiments was 200 psi.

Matrix	T(°C)	ρ (kg/m ³)	Relative Density	Average ρ (kg/m ³)	Average RD (%)	Standard Deviation	Error Bar
A356	750	1.8	61.33	1.83	62.24	1.79	4.44
		1.78	60.65				
		1.9	64.74				
A356	800	2.25	76.66	2.32	78.93	2.12	5.28
		2.4	81.77				
		2.3	78.36				
A356	850	2.52	85.86	2.54	86.54	2.01	4.98
		2.62	89.27				
		2.48	84.5				
A356	900	2.65	90.29	2.69	91.65	1.11	2.76
		2.69	91.65				
		2.73	93.02				
Matrix	T(°C)	ρ (kg/m ³)	Relative Density	Average ρ (kg/m ³)	Average RD	Standard Deviation	Error Bar
Mercusil	750	2.2	76.39	2.22	76.97	2.17	5.38
		2.3	79.86				
		2.15	74.65				
Mercusil	800	2.5	86.81	2.54	88.08	2.57	6.39
		2.47	85.76				
		2.64	91.67				
Mercusil	850	2.72	94.44	2.67	92.82	1.15	2.85
		2.65	92.01				
		2.65	92.01				
Mercusil	900	2.72	94.44	2.75	95.60	1.18	2.93
		2.8	97.22				
		2.74	95.14				

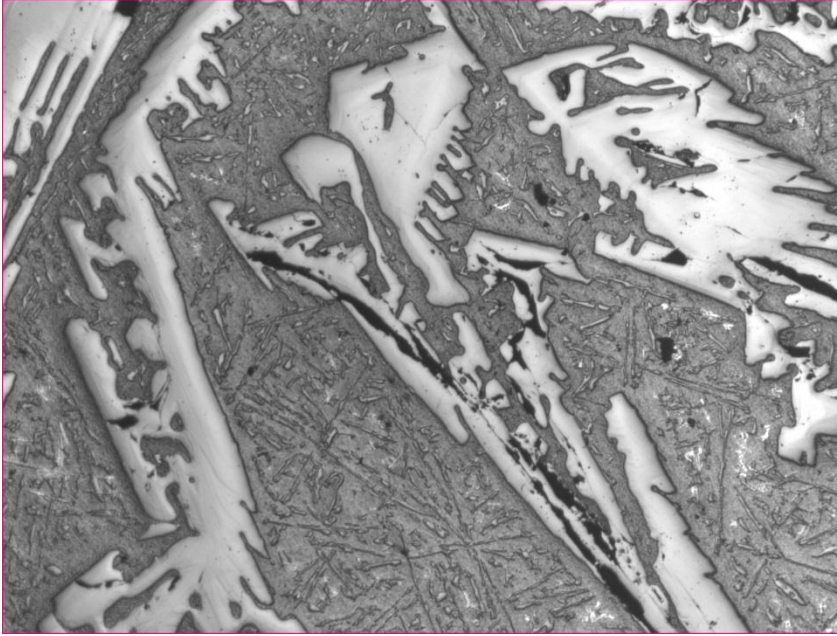


Figure 38. Micrograph of Mercusil Alloy (Magnification 50X)

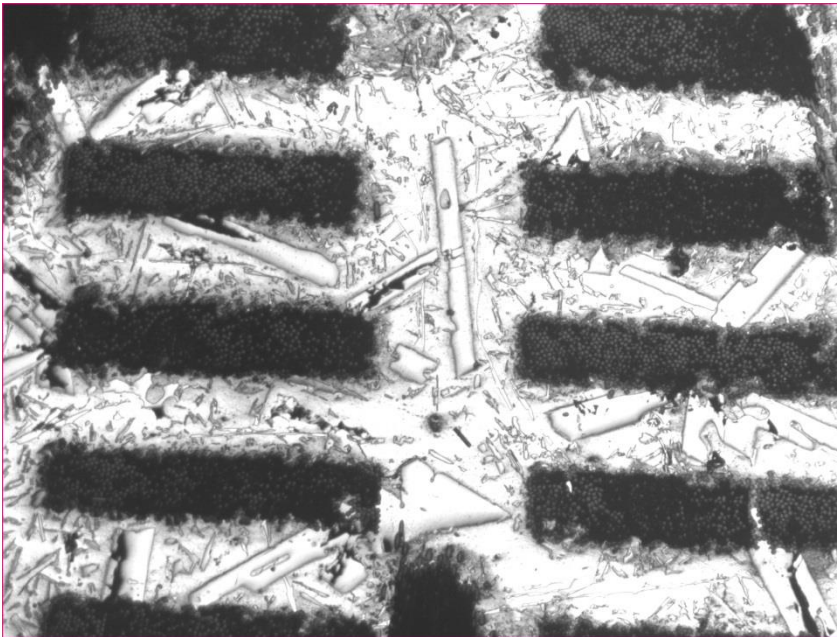


Figure 39. Micrograph of MMC with Mercusil Alloy as matrix made at 750C and 200 psi (Magnification 50X)



Figure 40. Micrograph of MMC with Mercusil Alloy as matrix made at 750C and 200 psi showing Z yarns (Magnification 50X)

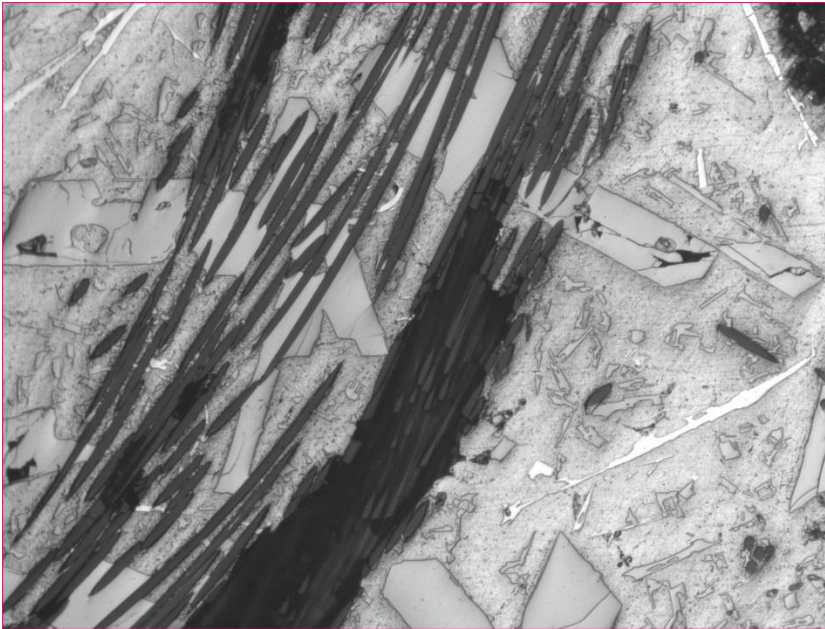


Figure 41. Micrograph of a partially infiltrated Z yarn (Magnification 100X)

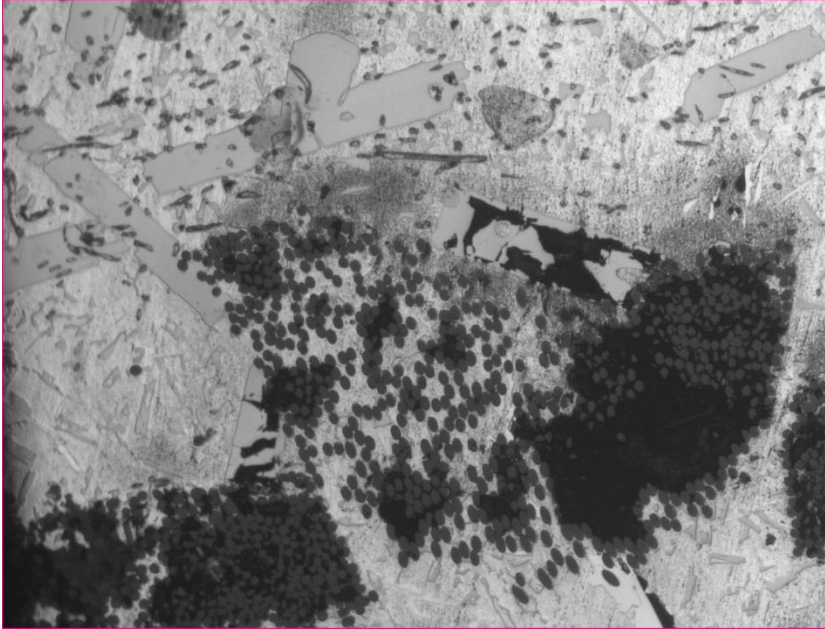


Figure 42. Micrograph of MMC sample made by Mercusil alloy as the matrix at 750 C and 200 psi (Magnification 100X)

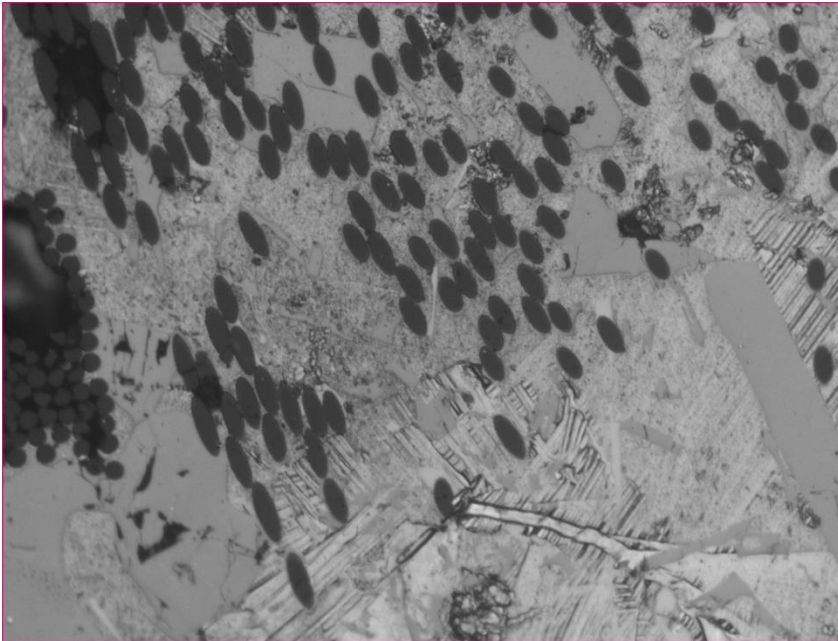


Figure 43. Micrograph of MMC sample made by Mercusil alloy as the matrix at 800 C and 200 psi (Magnification 200X)

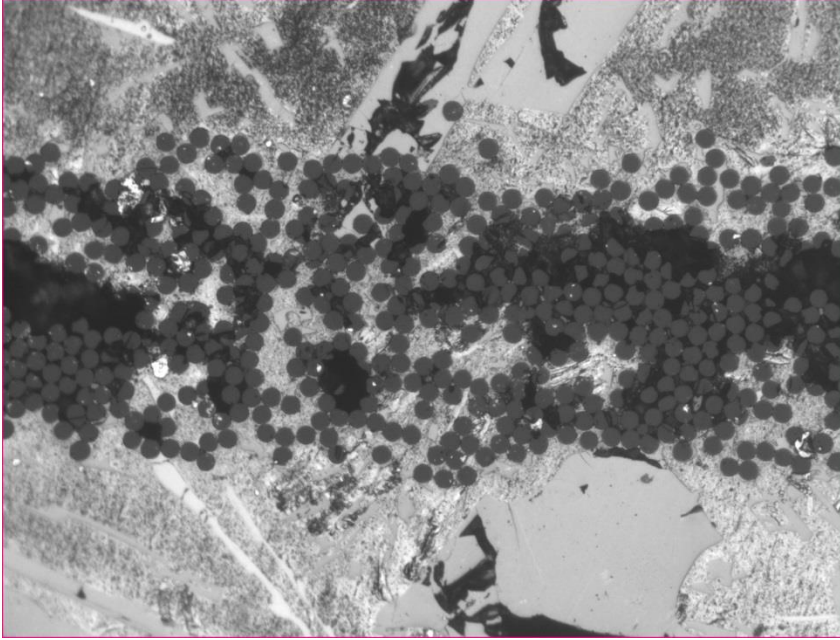


Figure 44. Micrograph of MMC sample made by Mercusil alloy as the matrix at 800 C and 200 psi showing the partial infiltration of a fiber tow (Magnification 200X)

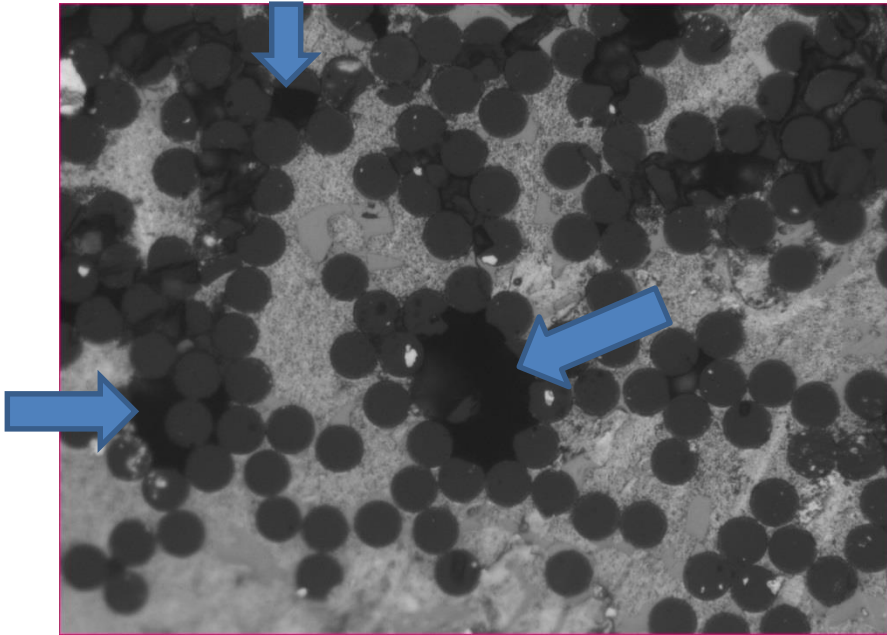


Figure 45. Micrograph of MMC sample made by Mercusil alloy as the matrix at 800 C and 200 psi showing the partial infiltration of a fiber tow and porosity (Magnification 500X)

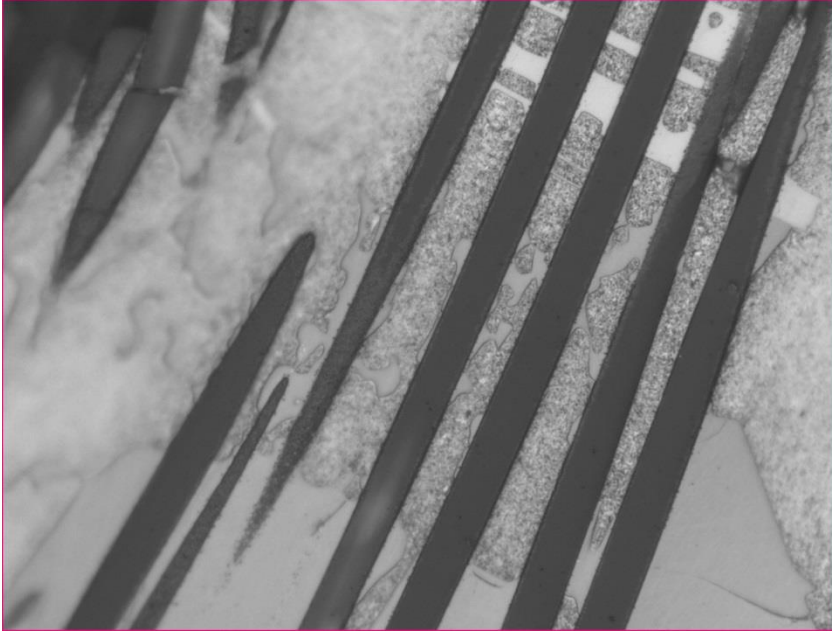


Figure 46. Z yarn fibers inside a tow infiltrated with mercusil alloy (Magnification 500X)

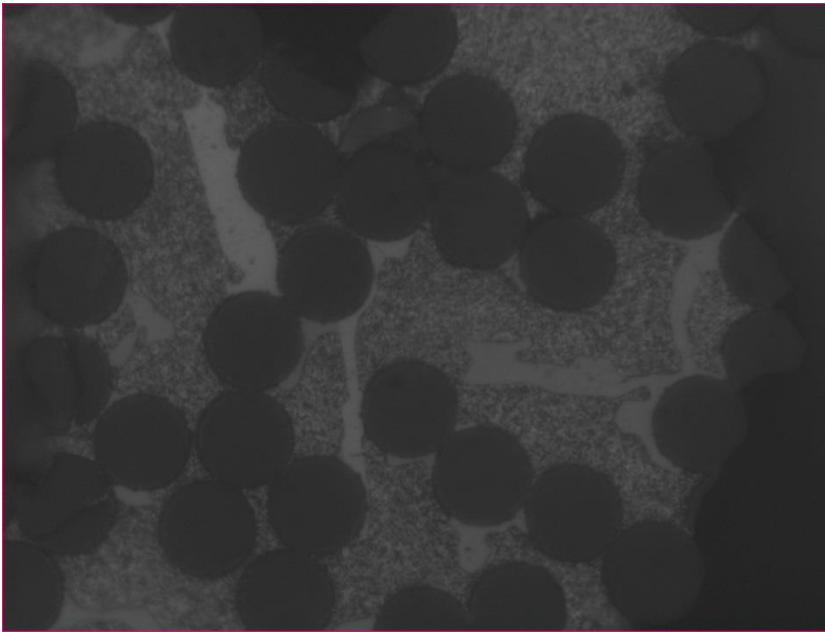


Figure 47. Micrograph of MMC sample made by Mercusil alloy as the matrix at 800 C and 200 psi (Magnification 1000X)

APPENDIX B: CALCULATING DARCY VELOCITY FOR MODIFIED CAPILLARY NUMBER

The superficial velocity used in Eqn. (7), which is the average velocity of metal inside the preform, can be estimated by assuming the infiltration process to be a line injection in a flat rectangular mold. This is a 1-D boundary value problem with time-dependent moving boundary. For simplicity, we assume there is full saturation behind the moving front and the preform is an isotropic medium. The governing differential equations for this problem are equations (1) and (2), which are Darcy's law and the continuity equation, respectively. For the 1-D case, these equations reduce to

$$q = -\frac{K}{\mu} \frac{dp}{dx} \quad (10)$$

$$\frac{dq}{dx} = 0 \quad (11)$$

Combining these equations, the governing equation for pressure distribution is given by

$$\frac{d^2 p}{dx^2} = 0 \quad (12)$$

The general solution to this equation is

$$p(x) = Ax + B \quad (13)$$

with A and B as arbitrary constants. The domain is from $x = 0$ at the entrance to $x = x_f(t)$ at the liquid-front in the mold with x_f being the x coordinate of the liquid front. We solve this problem for $0 \leq x \leq x_f(t)$ with the following pressure boundary conditions:

1. $p(x = 0) = p_{in} = const.$

2. $p(x = x_f) = 0$

Here p_{in} is the infiltration pressure applied to the incoming melt. Note that we ignore any suction pressure at the liquid front in this estimate. Applying these boundary conditions to

Eq. (12) results in: $B = p_{in}$ and $A = \frac{-P_{in}}{x_f(t)}$

On substituting A and B in Eqn.(12), we will have the equation for melt pressure distribution in the wetted preform as

$$p(x,t) = -\frac{P_{in}}{x_f(t)}x + p_{in} = p_{in}\left(1 - \frac{x}{x_f(t)}\right) \quad (14)$$

In calculating the modified capillary number for each experiment (Eqn. 7), the typical velocity was taken as the front velocity, which was estimated when the front has reached the middle section of the preform. From Eq. (13), the pressure distribution, when the front reaches the at mid-section, is

$$p(x) = p_{in}\left(1 - \frac{x}{T/2}\right) \quad (15)$$

where T is the flow-direction length of the preform. Hence the pressure gradient in the wetted portion of the PIP preform at the liquid front is given as

$$\left. \frac{dp}{dx} \right|_{x=T/2} = \frac{p_{in}}{T/2} \quad (16)$$

Now the front velocity, v_f , is obtained by dividing the Darcy velocity at the front with the void volume fraction, ε , as

$$v_f = \frac{dx_f}{dt} = \frac{q(x_f)}{\varepsilon} = \frac{K}{\varepsilon\mu} \frac{p_{in}}{T/2} \quad (17)$$

APPENDIX C: ESTIMATION OF PERMEABILITY FOR FIBER PREFORM

To estimate Ca^* (Eqn. 7) in the previous section, an estimate of the Darcy velocity at the mold center is needed, and for which, an estimation of the permeability, K , of the 3D weave Nextel fabric used in the present study is required. If we assume the preform to be single-scale porous medium, Kozeny-Carman equation can be used to calculate the preform permeability as

$$K = D_f^2 \phi(\varepsilon) \quad (18)$$

where D_f is the fiber diameter, ε is the void volume fraction of the preform, and ϕ is defined by the equation

$$\phi(\varepsilon) = \frac{1}{180} \cdot \frac{\varepsilon^3}{(1-\varepsilon)^2} \quad (19)$$

However, in determining the permeability of a dual-scale fabric, the size of pores between the tows, the diameter of the fibers inside the tows and the architecture of the preform, all play a role. Since the 3D Nextel fabric is of dual-scale type, the analytical correlation presented by Papathanasiou [222] for dual-scale porous media was applied to calculate the permeability of the preform. In this model, the boundary element method (BEM) was used to simulate Stokes flow across hexagonal arrays of unidirectional fiber tows in which the individual filaments are packed in hexagonal or square arrangements inside the tows. A semi-empirical correlation was developed for the dual-scale medium which allows prediction of the permeability of hexagonal arrays of fiber tows from a knowledge of their

inter- and intra-tow pore volume fractions, the type of intra-tow packing, and the diameter of intra-tow filaments. According to the Papathanasiou analytical solution, the overall permeability of such a dual-scale medium (K_p) is determined by liquid volumes passing through the inter- and intra-tow regions. The latter is related to the permeability of the tow itself (K_{tow}) while the former is related to the permeability of the system with the same inter-tow void volume fraction but made up of impermeable tows (K_s). K_{tow} and K_s are functions of the intra-void volume fraction (ϕ_t) and inter-tow void volume fraction (ϕ_i), respectively. The semi-analytical empirical correlation for K_p is of the form

$$K_p = K_s \left(1 + 2.67 \left(\frac{K_{tow}}{K_s} \right)^{0.89} \right) \quad (20)$$

where K_{tow} and K_s are calculated using Gebart's permeability model (1992) as

$$K = \frac{16}{9\pi\sqrt{2}} \left[\sqrt{\frac{1-\phi_{max}}{1-\phi}} - 1 \right]^{2.5} R^2 \quad (21)$$

Here K is the permeability, ϕ is the void volume fraction of the preform, and R is the fiber or tow radius. (Note that the tow-radius was half of the tow 'diameter', which was obtained as the average of the major and minor axes dimensions of the mostly elliptical tows.) ϕ_{max} , the porosity at maximum packing, is different for different types of packing (i.e., the hexagonal or square types) [222].

Empirical measurements on void volume as a fraction of the preform volume (i.e., average void volume fraction) furnish a value of about 0.65. Microscopic analysis of the

fabric filaments revealed the average fiber diameter to be 10-12 μm . The calculated permeabilities using the Papathanasiou model are presented in Table 6. It is noted from Table 6 that K_{tow} is very small in comparison to K_s and $K_p \cong K_s$. This suggests that very small amount of liquid will pass through the tows during transverse flows. On the other hand, a comparison between the permeability predicted by Kozeny-Carman equation, $K_{Kozeny-Carman}$, with the assumption of the preform being a single –scale porous medium, and K_p , derived from the equations for dual-scale preforms proposed by Papathanasiou, shows three order of magnitude difference between these two models (Table 12). This implies that the gaps between tows cause the permeability to shoot up and thus play an important role in facilitating melt flow in the dual-scale preforms.

Table 12. Some micro-geometrical properties of the preform and comparison of the dual-scale permeabilities obtained using the Papathanasiou model and the single-scale permeability obtained using the Kozeny-Carman model.

Shape of Tows	ellipse
Major Axis of Ellipse	844.64 μm
Minor Axis of Ellipse	185.65 μm
Fiber Diameter	11 μm
ϕ_t	0.24
ϕ_i	0.54
K_s	3.194 E-09 m^2
K_{tow}	2.471 E-15 m^2
K_p	3.194 E-09 m^2
$K_{Kozeny-Carman}$	1.506 E-12 m^2

APPENDIX D: WETTING PHENOMENA IN COMPOSITE SYNTHESIS

Many of the problems in the processing of metal matrix composites, such as poor wetting of the reinforcement by molten metal, are related to the interface between the metal and reinforcement [217]. Most metal matrix composites are non-equilibrium systems, a chemical potential gradient exists at the matrix-reinforcement interface, and this gradient is the driving force for diffusion or chemical reactions at high temperatures during processing[200]. Desirable interfacial features are sometimes contradictory. For example, high chemical affinity between the matrix and reinforcement is desired to ensure spontaneous combination of the two phases, yet low chemical affinity is desired to avoid unwanted chemical reactions at the interface during the processing. The interfacial zone that links the reinforcement phase with the metal can be in the form of a single surface of atomic bonds (simple interface) or one, or even several, new reaction phases and simple interfaces located between the reinforcement and matrix. In infiltration process, in which the reinforcement is combined with bulk metal, the free energy change is ΔG_i which is the change in free energy upon replacement of a square meter of reinforcement surface with surface energy of σ_{SV} , with a square meter of interfacial zone, of energy G_{SL}^s per square meter of interfacial zone:

$$\Delta G_i = G_{SL}^s - \sigma_{SV} \quad (22)$$

When there is no interfacial chemical reaction during processing, the interfacial zone is a simple interface and G_{SL}^s is the matrix/reinforcement surface energy, $\sigma_{SL} \cdot \Delta G_i$, is then the work of immersion W_i :

$$W_i = \sigma_{SL} - \sigma_{SV} \quad (23)$$

If $\sigma_{SV} > \sigma_{SL}$, the metal will wet the reinforcement, but in opposite case; work is required to make the solid/liquid interface. Thus in a non-wetting system of matrix/reinforcement, a minimum external pressure is required to start the infiltration. This threshold pressure P_0 (also called capillary pressure, P_c) can be defined in terms of the work of immersion as [223, 224]

$$P_0 = S_i W_i \quad (24)$$

where S_i is the reinforcement surface area per unit volume of metal matrix. The Young-Dupre equation can be used to relate the threshold pressure to the contact angle of liquid/solid interface [213, 225]

$$\sigma_{SV} - \sigma_{SL} = \sigma_{LV} \cos \theta = -W_i \quad (25)$$

or in other terms, the wetting contact angle which is an important parameter, is defined by Young's equation:

$$\cos \theta = \frac{\sigma_{SV} - \sigma_{SL}}{\sigma_{LV}} \quad (26)$$

Equation (23) can be written as:

$$P_0 = S_i \sigma_{LV} \cos \theta \quad (27)$$

The sessile-drop experiment and other capillary tests are used to estimate the contact angle in static conditions. By convention, if $\theta < 90^\circ$, the liquid is said to wet the substrate. Some

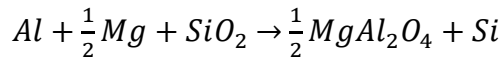
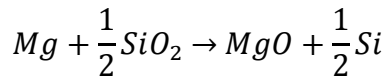
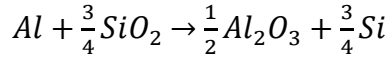
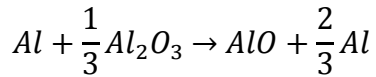
studies have been done so far to estimate contact angle at the metal-ceramic interfaces. The contact angle between molten metals or alloys and most inorganic fibers, such as Gr, SiC, Al₂O₃, etc., is found to be greater than 90°, and it may range to 150° or more. However, higher temperatures improve the wetting of metals and ceramics.

Due to the poor wettability of most ceramics with molten metals, melt intrusion of porous preforms requires overcoming a threshold pressure, which represents the capillary phenomenon described by the Young-Laplace equation:

$$P_c = \frac{2 \cdot \sigma_{LV} \cdot \cos \theta}{r_e} \quad (28)$$

where P_c is the capillary pressure to effect melt intrusion in a capillary of uniform radius r_e , and σ_{LV} is the surface tension of the liquid metal; θ is the contact angle [218].

For Al-based composites, the case is more serious because Al is usually covered with an oxide layer, which prevents wetting. One important limitation in liquid-state processing of MMCs is the compatibility between the ceramic reinforcement and the matrix. Wetting can be classified into two broad categories based on the nature of attractive forces at the interface: 1) Physical wetting and 2) Chemical wetting. Metals are known to wet ceramics essentially by chemical bond formation. When molten Al alloy is in contact with alumina and silica, the following interfacial reactions can occur forming oxides as reaction products [226]:

Table 13. Possible Interfacial Reactions in Nextel 720 reinforced A356.

It was found that wetting between alumina and aluminum is not significant up to temperatures higher than 1000C [227, 228] and even at higher temperatures, it is not still a strong wetting. The wetting behavior of liquid metal/ceramic system not only depends on thermodynamic characteristics as reactivity and solubility but also external factors such as atmosphere, surface condition of the substrate (roughness, crystallographic orientation, impurities and adsorption), and particularly the surface oxidation of the aluminum and the thickness of the oxide film. Addition of highly reactive elements as Mg to the melt is known to improve wettability. Wetting is affected by reaction between reactive elements and alumina at the metal-oxide interface through the formation of intermetallic compound, which is thought to modify and rupture the oxide film on the surface of the molten aluminum, exposing clean wettable surfaces. Temperature is another important factor increasing the wettability in metal-ceramic interfaces. Ouyang et al. [226] calculated the contact angle of $Al_2O_3/Al+xMg$ interface by a physicochemical mode. Their calculated results are shown in Figure 38. In many metal-ceramic systems, high temperatures cause the dissociation of a ubiquitous oxide film on the melt and the consequent establishment

of true contact between the metal and the reinforcement. This leads to a sudden drop in the value of the wetting angle.

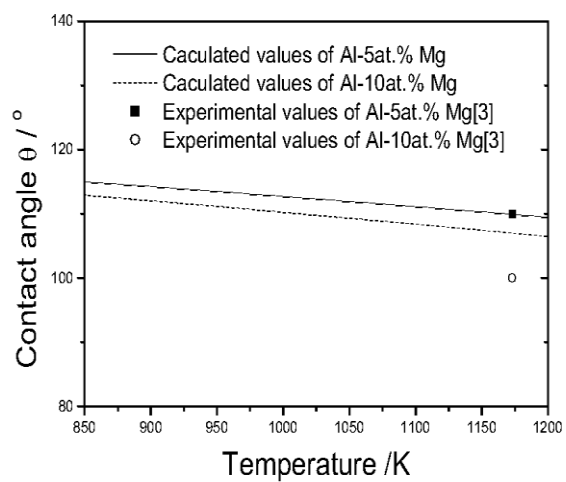


Figure 48. Variation of contact angle of Al-Mg with Al_2O_3 versus Temperature [226] .

APPENDIX E: THE PHYSICS OF SHRINKAGE POROSITY

The shrinkage that occurs on solidification is the primary source of porosity formation in solidifying castings. Solidification shrinkage is a contraction that occurs at liquid solid transition as a result of more open atomic arrangement in the liquid changing to the denser solid phase. In most cast alloys, the volume shrinkage is typically between 5-8% [41]. If a region of liquid in the casting becomes isolated from additional feed liquid, then after solidification and shrinkage, the pressure in the liquid drops, causing an increasing pressure difference between the inside and outside of the casting. In this case, there are two possibilities: (i) internal shrinkage porosity may form in the presence of favorable nuclei (ii) the solidified shell of the casting collapse plastically inwards forming external porosity or sink.

Ilegbusi and Yang [208] considered a planar matrix/reinforcement interface to study the fundamental mechanism of pore nucleation during PIP. The local pressure, P_l , in this system is the sum of three components

$$P_l = P_{shr} + P_{hyd} + P_{app} \quad (29)$$

Here P_{shr} is the pressure due to solidification shrinkage, P_{hyd} is the hydrostatic pressure, and P_{app} is the externally applied pressure. To avoid the formation of a stable void, this local pressure must be less than the fracture pressure. Fisher [229] and Campbell [221], calculated the fracture pressure for decohesion at the interface using the approach for heterogeneous void nucleation as

$$P_f = - \left[\frac{16\pi}{3kT} \frac{\sigma^3 \Phi}{\text{Ln}(6N^{2/3}kT/h)} \right]^{1/2} \quad (30)$$

where N , k and h are the Avogadro's, Boltzmann's and Planck's constants, respectively, and

$$\Phi = (2 + 3\cos\theta - \cos^3\theta)/4 \quad (31)$$

where θ is the contact angle.

Assuming unidirectional solidification and Darcy's law for the interdendritic flow in the solidifying MMC, Piwonkka et al. [230], obtained the equation for the shrinkage pressure as

$$P_{shr} = \frac{24\pi\mu\beta\tau^3\Delta T}{1-\beta} \frac{1}{d_1^2} \frac{V_s}{G} \ln \frac{f_l}{\alpha_l} \quad (32)$$

where τ is the tortuosity of the preform, and α_l is the liquid fraction at the end of mass feeding, which is assumed to be 0.32 [221], μ is viscosity, ΔT is the solidification range of the matrix alloy, f_l is the liquid fraction, V_s is the solidus velocity, G is the temperature gradient and d_1 is the dendrite arm spacing. The value of β , solidification shrinkage, is defined by the equation

$$\beta = \frac{\rho_s - \rho_l}{\rho_l} \quad (33)$$

where ρ_s and ρ_l are densities of the liquid and solid phase, respectively.